ORNL/TM-2012/337

Developing Fatigue Pre-crack Procedure to Evaluate Fracture Toughness of Pipeline Steels Using Spiral Notch Torsion Test

August 2012

Prepared by

Jy-An John Wang, Ting Tan, Hao Jiang, Wei Zhang, Zhili Feng

Materials Science and Technology Division
Oak Ridge National Laboratory

ORNL/TM-2012/337

Materials Science and Technology Division
Oak Ridge National Laboratory

Developing Fatigue Pre-crack Procedure to Evaluate Fracture Toughness of Pipeline Steels Using Spiral Notch Torsion Test

Jy-An John Wang, Ting Tan, Hao Jiang, Wei Zhang, Zhili Feng

Materials Science and Technology Division
Oak Ridge National Laboratory

Date Published: August 2012

Prepared by
OAK RIDGE NATIONAL LABORATORY
Oak Ridge, Tennessee 37831
Managed by
UT-BATTELLE, LLC

For the
U.S. DEPARTMENT OF ENERGY
under contract DE-AC05-00OR22725

ACKNOWLEDGEMENTS

This research was sponsored by the Department of Transportation Pipeline and Hazardous Materials Safety Administration **(**PHMSA) Program and was carried out at Oak Ridge National Laboratory under contract DE-AC05-00OR22725 with UT-Battelle, LLC.

The authors would like to thank DOT program manager, Mr. James Merritt, for supporting this project, and Dr. Hong Wang for reviewing this report.

Table of Contents

LIST OF FIGURES

LIST OF TABLES

EXECUTIVE SUMMARY

Fracture toughness and fatigue properties of pipeline steels play a critical role in developing advanced high-pressure hydrogen infrastructure for alternative fuel pipelines program. The reliability of structure components, particularly resistance to damage and failure in the intended service environment, is highly dependent on the selected materials. An effective surveillance program is also necessary to monitor the material degradation during the course of service. Steels have been proven to be desirable for hydrogen infrastructure. However, hydrogen embrittlement is an important factor that limits steel performance under high-pressure hydrogen conditions.

In order to reach the above goal, we have proposed an innovative technology, based on spiral notch torsion test (SNTT) methodology, to effectively investigate the material performance of X52 pipeline steel. The SNTT approach was successfully demonstrated and extended to X52 steels during the performance period. In addition to single notch front geometry, the crack growth behavior of the SNTT process has been effectively established using an integrated experimental, numerical and analytical approach. The results indicate that the proposed protocol not only provides significant advance in understanding the compliance evolution of the SNTT specimen, but also can be readily utilized to assist future development of hydrogen infrastructures.

In FY2011, an extensive study was performed to characterize the fracture toughness degradation of AISI 4340 high-strength steel exposed to high-pressure hydrogen using in situ spiral notch torsion tests. This effort included equipment setup and calibration, sample design and fabrication, finite element simulation of the specimen fracture, and fractographic characterization using advanced microscopic techniques. The detailed description of the results is summarized in by Wang [Wang 2011]. The SNTT samples tested in the current study were either X52 steel (base line material) or welded materials. A 45° pitch angle for the spiral was machined for all SNTT samples in this study. Mode I failure served as the starting point in the cycle fatigue process. Under fatigue loading conditions, the crack evolved progressively to the center of the cylinder and finally formed Mode III failure at the end of cycle in the back of the samples due to shear tearing.

Based on the successful experience of applying SNTT to 4340 steel materials in FY2011, a significant amount of effort on this initiative was focused on the design and fabrication of X52 test samples and fixtures suitable for SNTT cycle-fatigue testing. Various designs and trials were carried out in a joint collaboration between different groups at the Oak Ridge National Laboratory. Bulk plates from current pipe lines were manufactured, and SNTT samples were subsequently machined from these plates. For each sample, an entire spiral loop was machined for the SNTT cylinder with a notch–to-diameter ratio of 0.1. A new set of fixtures was

fabricated to accommodate the X52 SNTT samples. Threads were introduced into both ends of the SNTT samples to help improve sample stability during the cycle-fatigue process.

The finite element method (FEM) was used to characterize the crack growth in the SNTT process. FEM models were established to capture the stress concentrations around the non-coplanar three-dimensional spiral crack front. Different meshes were assigned to different areas to achieve this goal. A series of FEM models was created to cover the crack depth range from 0.1 to 0.45 in the crack depth-to-diameter ratio. For each crack depth, either angle or torque was applied to perform the numerical analysis. The output from these models included the reaction torque, the end rotational angle, and the energy release rate. Beside the tested SNTT cylinder samples, which measured 0.375 inch in diameter, numerical cases were also extended to SNTT samples with a 1-inch diameter. Corresponding indices, including the torque, angle and energy release rates, were also obtained for these models. Evaluation was also performed on aluminum SNTT samples with the above two dimensions, and the results were included for analysis.

By summarizing these numerical results, the evolution of the SNTT compliance and the energy release rates were studied carefully with respect to different crack lengths. Two non-dimensional indices, the characteristic compliance and the characteristic energy release rates of SNTT, were proposed to quantify the crack growth process of SNTT. Collapse trends were observed between SNTT samples with different dimensions, as well as between samples made from both steel and aluminum. Analytical models in both broken and unbroken ligament forms were proposed to quantify the crack penetration depth based on these non-dimensional indices. The sensitivity in the broken ligament form facilitates the experiment measurements, which could be easily adapted by industrial communities.

Experiment measurements were performed at different crack lengths during the cycle fatigue process. Specimens were cut in cross sections, and crack penetration depths were compared with predictions from the compliance function. For the base material X52, a generally good agreement was observed between predictions and the experimental measurement. For the welded X52 materials, good agreements were observed for some specimens. For other samples, crack deviation was observed during the cycle fatigue process. The reason for this deviation is probably related to the heterogeneous properties of the welded material, on which further study is needed. In order to validate the analytical models, further analysis was carried out on the RVDT measurement and finite element model predictions. The net section of the SNTT specimen was modeled with the measured crack depth. By using the torque data from the RVDT measurement, good agreement was observed between the predictions and the measurement.

In this study, one interesting phenomenon observed is the deviation of crack penetration in the welded samples. Further effort is needed to characterize the cycle fatigue behavior of in homogeneous material. Other areas of interest include the fracture toughness of X52 or X80 in

high-pressure hydrogen environments for both base and welded materials. The dependence of crack penetration pattern on the spiral turns is also of great interest for future study. A good design of the SNTT sample can effectively reduce the end effect of the samples and facilitate uniform crack penetration in the cycle-fatigue process.

1. INTRODUCTION AND BACKGROUND

Hydrogen is a plentiful energy source with the potential for a major impact on energy security and climate change [Baldwin 2009]. One of the primary challenges of moving toward a hydrogen economy is reducing the cost of hydrogen storage and transport at the commercial level. The DOE Hydrogen Program performed assessments of compressed hydrogen storage during 2006-2009 [Hua 2010]. The principal conclusion of the assessment was that the 350-bar (~5000 psi) compressed storage system has the potential to meet the projected 2015 system capacity. The material performance of steel under such high pressure is an important factor for evaluation [Nancy, 2007, Somerday 2005, Somerday 2010].

The safe, reliable operation of structural components is critically dependent on the selection of materials that are resistant to damage and failure in the expected service environment. An effective surveillance program is also necessary to monitor the degradation of the materials in the course of service. Steels are preferred options for hydrogen storage tanks because of their combination of strength and stiffness. However, the degradation of fracture toughness in steel induced by hydrogen embrittlement has not been thoroughly investigated, especially for ductile steels such as X52 or X80. To meet this need, we propose to develop new approaches based on the spiral notch torsion test (SNTT), an ORNL-patented, R&D 100 Award-winning technology

1.1 Hydrogen Infrastructure Materials

It is important to understand the hydrogen embrittlement mechanism before mechanical characterization is performed. In steels, hydrogen can facilitate transforming austenite to martensite, the latter of which is highly affected by hydrogen embrittlement [Bromley 2008]. There are three primary embrittlement mechanisms proposed: hydrogen-enhanced decohesion (HEDE) [Losch 1979, Shivanyuk 2003, Han 1998], hydrogen-enhanced localized plasticity (HELP) [Losch 1979, Gavriljuk 2003, Liang 2008] and hydride-induced embrittlement (HIE) [Abraham 1995, Shivanyuk 2001, Varias 2002].

Hydrogen infrastructures, including hydrogen storage tanks, are subjected to complex, multiaxial stress states due to high hydrogen concentration and pressure fluctuation. The formation of blisters and cracks can be indications of hydrogen embrittlement [Bromley 2008]. To ensure the reliability and safety of hydrogen systems, it is necessary to identify the mechanisms that might lead to failure in pipe or tank materials and to fully characterize material behavior under extreme conditions. This is of particular interest to the high-pressure hydrogen segment in the automotive industry

Fracture is one of the most dramatic failure modes of any engineering structure. A material's intrinsic capacity to resist fracture is known as fracture toughness. The fracture toughness of

steel degrades significantly in high-pressure hydrogen situations. Thus, to obtain a complete knowledge of the fracture behavior of steel in the hydrogen environment, it is important to understand the specific behavior of steel under different loading conditions.

There are three independent fracture modes: Mode I (opening mode), Mode II (in-plane shear), and Mode III (tearing or out-of-plane shear) [Sanford 2003]. Since hydrogen infrastructures are subject to mixed mode loading in their service environments, it is highly desirable to study the mixed-mode loading effect on the integrity and durability of the hydrogen infrastructure.

A variety of testing methods [ASTM 2010, Carlisle 1959, Gaydos 2007] have been proposed for mechanical testing for steels affected by hydrogen embrittlement , including tensile test [Caskey 1983], notched tensile test [Walter 1969, ASTM 2010], notched tensile test in self-loading fixture [ASTM 2010], self-loading bend test [ASTM 2010], notched square bend test [ASTM 2010], disk rupture test [Fidelle 1974], constant displacement stress bar test [ASTM 2010], and torque bolt test [Carlisle 1959]. However, there has been little effort devoted to developing a test to characterize the fracture behavior of steel under mixed loading modes, particularly mode I and mode III, which is essential for design and development of these materials for hydrogen infrastructures.

1.2 Spiral notch torsion test (SNTT)

In this project, a novel testing method based on the spiral notch torsion test (SNTT) [Wang 2000,Wang 2002a, Wang 2011] has been further refined to quantify the crack growth behavior of isotropic materials under combined Mode I and Mode III loading.

The original SNTT test method uses a round-rod specimen having a V-grooved spiral line at a 45° pitch (Figure 1), subjected to pure torsion. In the absence of the V-groove, the stress state of a generic element in a round bar under pure torsion can be depicted as tension (normal to the 45° pitch) and compression (tangential to 45° pitch) of equal magnitude.

When a notch is introduced (Figure 1), a tri-axial tensile stress field will evolve in the neighborhood of the notch root area. This observation has been experimentally and analytically validated [Wang 2000, 2002b]. When the grooved specimen is sectioned into segments perpendicular to the groove line, each of the segments can be viewed as a compact tension (CT) specimen with a notch. Since all the imaginary CT specimens are bonded side-by-side seamlessly, the compatibility condition is automatically satisfied, and remains in place before and after application of torsion loading.

Therefore, when a V-grooved spiral line with a 45° pitch is machined on the surface of the specimen, the grooved line effectively becomes a Mode I crack mouth opening. When the pitch

angle is other than 45°, the mode III condition is introduced at the notch root, which enables the investigation of fracture behavior under I/III mixed mode loading.

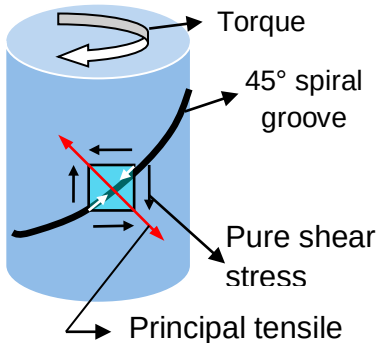

Figure 1. The configuration of SNTT specimen.

Due to the 3-D non-coplanar crack front of the SNTT configuration and the lack of closed form solutions, K_{IC} of the SNTT method was evaluated using 3-D finite element analysis and derived from minimum strain energy density criterion [Sih 1974] or J-Integral based on the domain integral method [Wang 2000, 2002b].
The current SNTT method works well for brittle materials, which have been proved in references [Wang 2000, Wang 2002a]. As for ductile materials, some parts need to be improved. First, it has not been able to capture the crack growth behavior in the SNTT cycle fatigue process. Then, the compliance function or the energy release rates with respect to different crack lengths have not been disclosed.

2. Scope of current research

The objective of this research project is to use the spiral notch torsion test (SNTT) to study the crack growth behavior during the cycle fatigue process, which is an essential element in evaluating the reliability of hydrogen infrastructures. The project was divided into two stages:

1) SNTT compliance and energy release rate function development, and
2) SNTT crack growth experimental validation.

In the first stage, finite element models were established to calculate the compliance and energy release rate with respect to different crack lengths. Functions of compliance and energy release rates were established using non-dimensional indices of characteristic compliance and energy release rates. Then, SNTT samples were designed and fabricated from X52 base material – a steel commonly used in hydrogen infrastructures. Spiral notches with uniform notch depth and pitch angle were machined on the steel samples. Using the SNTT technique, the cycle fatigue behavior was investigated. Fractographic examination was performed to study the fracture

mechanisms, while the compliance function was used to estimate fracture toughness. The accomplishment in the previous stage demonstrated the applicability of the SNTT technique to 4340 materials and provided important guidance for the current study.

Based on earlier work on 4340 steel, a significant effort was dedicated to SNTT sample design and fabrication in the second stage of this project. Several different designs of SNTT steel samples were compared. SNTT experiments were performed on steel samples fabricated from both base and welded materials. Incorporating acoustic technique, preliminary data on the fracture toughness of X80 samples was collected.

3. SNTT compliance studies

X52 steel has been widely used in the oil industry to transport gas and oil in large volumes. The detailed information on equipment setup and calibration, sample design and fabrication, SNTT testing, and post mortem fractographic examination is included in Wang, 2011.

3.1 Materials and samples

The chemical composition of the X52 steel used in this study is listed in Table 1.

Table 1. Chemical composition of the X52 steel used in the study.

C	Si	Mn	P	S	Cu	Ni	Cr	Mo	V	Ti	Nb
0.06	0.12	0.87	0.011	0.006	0.03	0.02	0.03	0	0.002	0	0.03

SNTT samples were machined according to the geometry shown in Figure 2. The samples were 0.375" (9.53 mm) in diameter with a gauge length of 0.942" (23.92 mm). A V-shaped spiral groove was machined on the sample surface with a pitch angle θ. When $\theta = 45^o$ the notch root is subject to an effective Mode I loading; and when $\theta \neq 45^o$, the notch root is then subject to a mixed loading of Mode I and Mode III. Examples of machined epoxy samples are shown in Figure 2b.

Figure 2. The geometry of the machined X52 SNTT samples

3.2 SNTT experiments

In this project, a servo-hydraulic axial/torsional testing machine (Model 809, MTS Systems Corp. Eden Prairie, MN, USA) was used to perform SNTT testing. Notched samples with fatigue precrack were used for some samples.

For cyclic fatigue testing, the tests were performed either through a function generator or a control program. Using the function generator, angle control was applied to the crack growth process during the SNTT test. For the control program, torque control was used with controlled torque of 380 lbf-in at maximum to initiate cracking; the minimum torque was 10 lbf-in. The cycle frequency was 5HZ. The fracture surfaces were examined by optical microscopy (SZH10, Olympus, Japan) and scanning electron microscopy (S3400, Hitachi, Japan). The following section discusses the process in detail.

3.3 Finite element analysis

Finite element analysis (FEA) was used to analyze the Spiral Notch Torsion Test (SNTT) results from the cycle fatigue process. The particular focus of the analysis was to evaluate the compliance and the energy release rates evolution during the cycle fatigue process. Therefore, semi-analytical models were proposed to quantitatively estimate the crack penetration depth or the fracture toughness. A series of SNTT models with different crack lengths were created to simulate the SNTT crack penetration process. Numerical cases were performed on SNTT specimens with different dimensions and materials.

3.3.1 Geometries

In this finite element model, the height of the cylinder, h, was selected to be one-eighth of the pitch length, i.e., $0.125p$. Therefore, the spiral rotational angle between the top and bottom of the cylinder, θ_h, was given by:

$$\theta_h = 2\pi\frac{h}{p} = (2\pi)\frac{1}{8} = \frac{\pi}{4} \tag{1}$$

A three dimensional finite element model was established in commercial software Abaqus™ 10.0 (Dassault Systèmes, Providence, RI). The model geometry is shown in Figure 3.

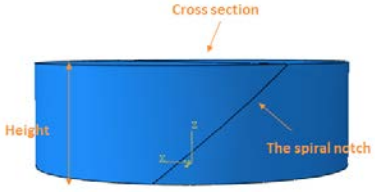

Figure 3. The geometry of the epoxy SNTT model.

3.3.2 Meshing

In the finite element model of the epoxy SNTT sample, the spiral notch served as the initiation or starter of a three dimensional (3-D) non co-planar crack front. The associated meshing strategy must capture the stress concentrations along this spiral crack front, and the energy release rates are extracted from these stress contours (Figure 4).

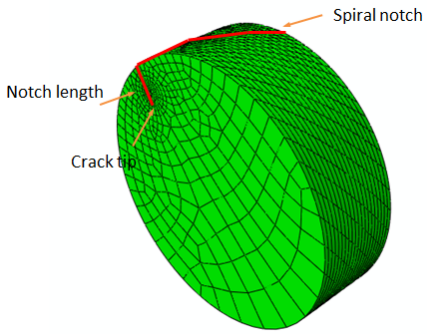

Figure 4. The finite element mesh of the epoxy SNTT sample

Different element types in the associated regions were assigned to area A1, A2 and A3 (Figure 5 and Figure 6). In Figure 5, the element C3D20R in Abaqus was assigned to area A1, which is outside the red circle. In Figure 6, the crack tip area, the area inside the red circle, is illustrated with higher resolution. The element C3D20R was also assigned to area A2; while the singular element C3D15 was assigned to area A3. In areas A2 and A3, the web mesh is able to capture the stress concentrations along the spiral notch crack front.

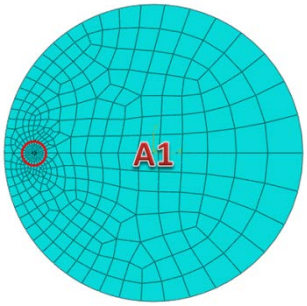

Figure 5. The finite element model mesh in area A1

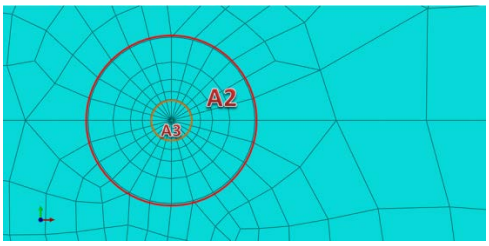

Figure 6. The finite element model mesh in areas A2 and A3

3.3.3 Mechanical properties

The steel materials used for SNTT samples are from actual welded pipes, either the pipe section or the welded area. All the steel materials used in this study were assumed as linear elastic

materials. The primary mechanical properties used in the finite element models are summarized in Table 2.

Table 2. Mechanical properties of epoxies used in the FEM study

Material	X52
Young's moduli, E (GPa)	2.9E7 [a]
Poisson's ratio, ν	0.3 [a]
Density (Kg/m^3)	7.85E3 [a]
Tensile strength (MPa)	420~550

[a] Data sheet of X52 from Wei Zhang.

3.3.4 Loading and boundary conditions

The loading and boundary conditions are displayed in Figure 7. A concentrated torque was applied at the center of the cross section on one end of the cylinder model. On the other end, the in-plane translations were fixed.

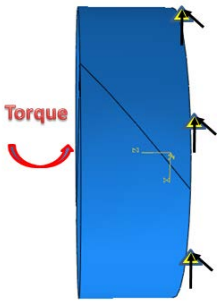

Figure 7. Loading and boundary conditions of the SNTT model

3.3.5 Finite element results

3.3.5.1 Displacement distributions of the steel SNTT sample

In order to illustrate the displacement contour of the steel SNTT samples, a cylindrical coordinate system was defined (Figure 8). The tangential and the radial orientations were along with the cross-section circle, while the axial orientation was aligned with the cylindrical axis of the SNTT samples.

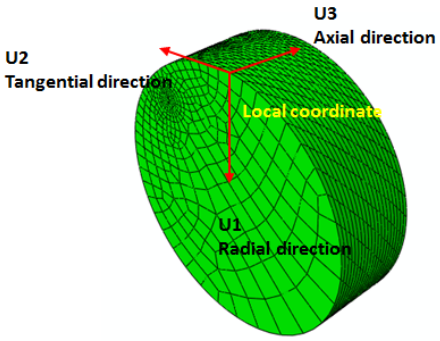

Figure 8. A cylindrical coordinate systme of the SNTT sample

The displacement contours of the deformed steel SNTT sample are shown in Figure 9 to Figure 11. Similar contours were observed for other crack depths.

The numerical results for the X52 steel SNTT sample with the a/D ratio of 0.1 were selected as a representative example for the single SNTT samples in Figure 9 to 10. Figure 9 indicates that the maximum radial displacements (red areas) appear to be on the middle section away from the ends of the spiral notch; which is consistent with displacement of a rotating cylinder. Furthermore, due to pure shear stress loading, the maximum stress contour is located on the perimeter or the outer surface of the SNTT samples.

Tangential displacement is plotted in Figure 10. The red contours are areas with zero tangential displacements, corresponding to the fixed surface. The blue contours are the maximum tangential displacement areas, corresponding to the torque-applied surface. The gradient located between the red and the blue contours reflects the tangential displacement variation along the spiral notch. Tangential displacements were around zero in the center area of the torque applied surface tangential displacements are maximum on the perimeter of the cross-section due to torsion loading.

The axial displacement distributions of the deformed X52 steel sample were shown in Figure 11. It showed that the contours of the split halves are symmetrically distributed around the spiral notch crack front. This is due to symmetrical reaction forces of the torsional loading applied to the two halves.

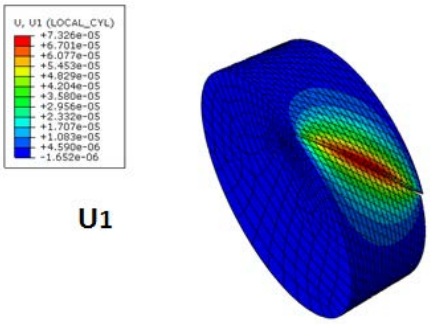

Figure 9. Radial displacement contours of the deformed X52 steel SNTT sample

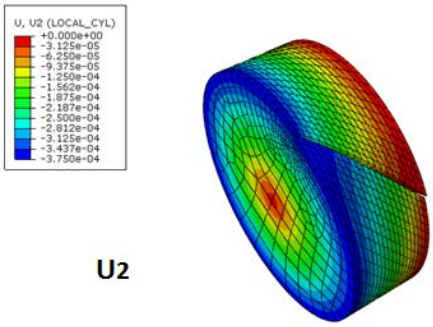

Figure 10. Tangential displacement contours of the deformed X52 steel SNTT sample

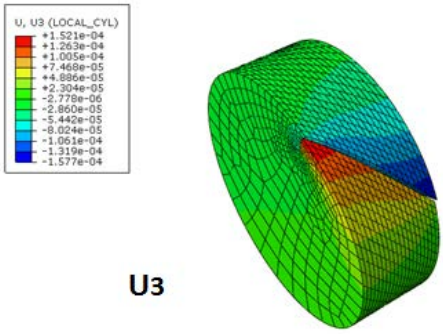

Figure 11. Axial displacement contours of the deformed X52 steel SNTT sample

3.3.5.2 von Mises stress distributions in single-depth steel SNTT sample

The von Mises stress distributions of the deformed steel sample are illustrated in Figure 12. The stress concentrations phenomenon was observed near the vicinity of the spiral notch. In Figure 13, the von Mises stress distributions around the crack tip are displayed in cross-section view. Deformed notch root blunting was clearly presented, and the butterfly plastic process zone was also captured by the wedge element mesh.

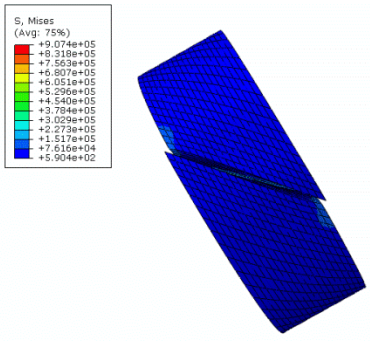

Figure 12. von Mises stress contours of the deformed steel SNTT sample

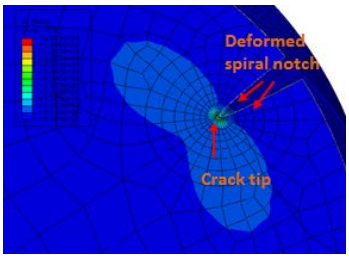

Figure 13. von Mises stress contours near the crack tip of the steel SNTT sample

3.3.5.3 Numerical models with different crack lengths

One interesting area for analysis is crack growth during the SNTT cycle fatigue process. It is important to quantify the evolution of crack depth in a SNTT specimen with measurable experimental indices, such as compliance and energy release rates. Therefore, a series of SNTT models were established to simulate the crack penetration process. Two different types of SNTT specimens, either 0.375 or 1.0 inch in diameter, were selected to model the crack penetration process. The ratio of notch to diameter ranges from 0.10 to 0.45. Either torque or theta control was applied to perform the numerical analysis. The crack series for X52 steel SNTT samples in Figure 14 to Figure 21 illustrate the crack growth process.

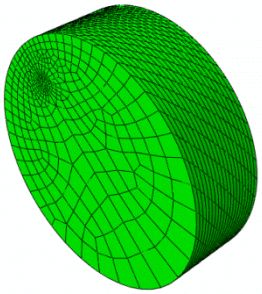

Figure 14. Finite element mesh of X52 steel SNTT sample with notch-to-diameter ratio of 0.10.

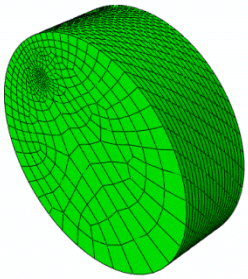

Figure 15. Finite element mesh of X52 steel SNTT sample with notch-to-diameter ratio of 0.15.

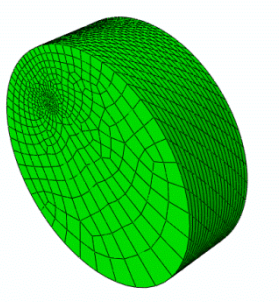

Figure 16. Finite element mesh of X52 steel SNTT sample with notch-to-diameter ratio of 0.20.

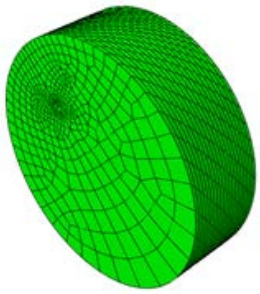

Figure 17. Finite element mesh of X52 steel SNTT sample with notch-to-diameter ratio of 0.25.

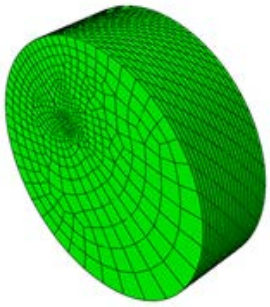

Figure 18. Finite element mesh of X52 steel SNTT sample with notch-to-diameter ratio of 0.30.

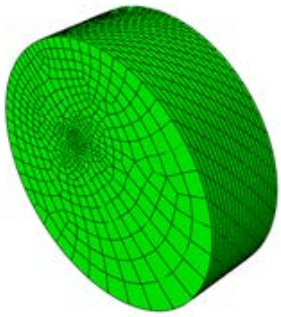

Figure 19. Finite element mesh of X52 steel SNTT sample with notch-to-diameter ratio of 0.35.

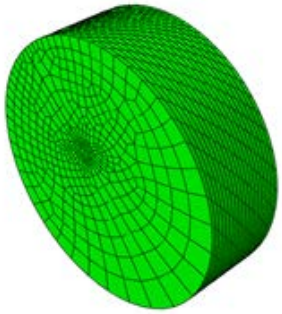

Figure 20. Finite element mesh of X52 steel SNTT sample with notch-to-diameter ratio of 0.40.

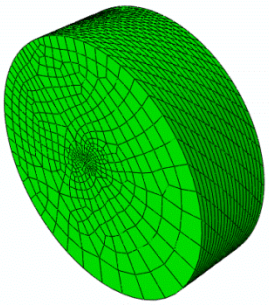

Figure 21. Finite element mesh of X52 steel SNTT sample with notch-to-diameter ratio of 0.45.

3.3.5.4 Von Mises stress evolution during the crack growth process

At each crack depth, the same meshing rules were applied to the model as shown in section 3.3.2. Wedge elements were assigned around the crack tip area to capture the stress singularity. With the growing crack penetration depth, the von Mises stress distributions around the crack tip area also change accordingly. The variance of von Mises stress in the crack tip area is displayed in Figure 21 to Figure 28 below. Table 3 to Table 10 provide detailed numerical results of finite element analysis for different cases.

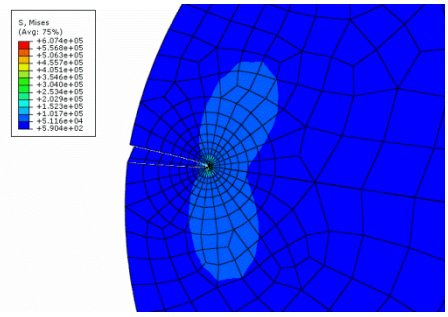

Figure 22. Mises stress around the crack tip of X52 steel SNTT sample with notch-to-diameter ratio of 0.10.

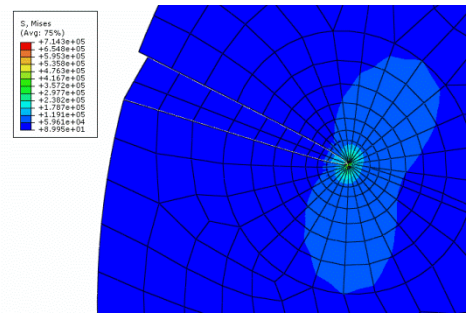

Figure 23. Mises stress around the crack tip of X52 steel SNTT sample with notch-to-diameter ratio of 0.15.

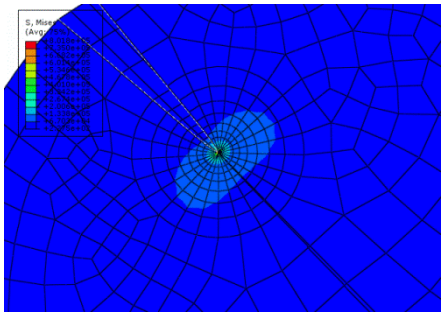

Figure 24. Mises stress around the crack tip of X52 steel SNTT sample with notch-to-diameter ratio of 0.20.

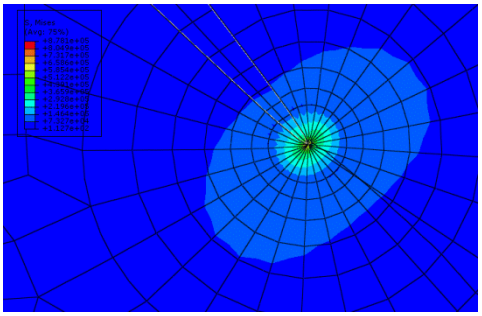

Figure 25. Mises stress around the crack tip of X52 steel SNTT sample with notch-to-diameter ratio of 0.25.

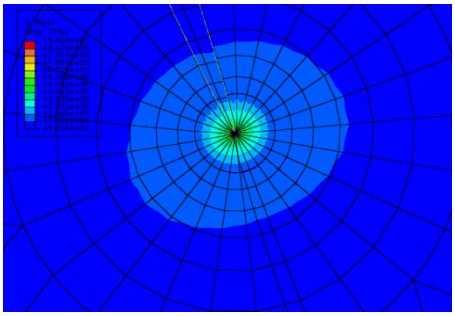

Figure 26. Mises stress around the crack tip of X52 steel SNTT sample with notch-to-diameter ratio of 0.30.

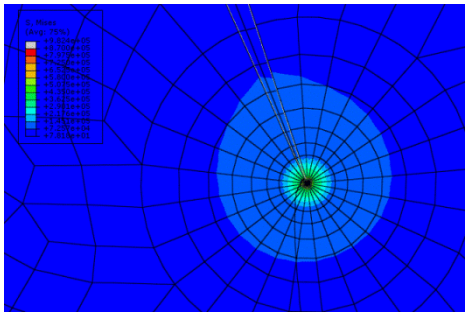

Figure 27. Mises stress around the crack tip of X52 steel SNTT sample with notch-to-diameter ratio of 0.35.

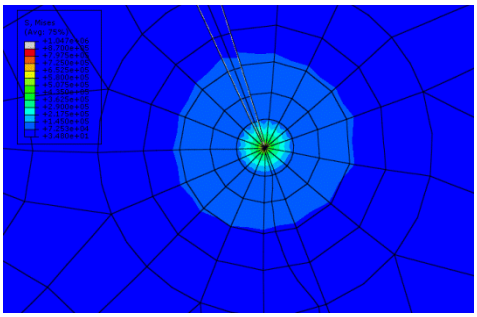

Figure 28. Mises stress around the crack tip of X52 steel SNTT sample with notch-to-diameter ratio of 0.40.

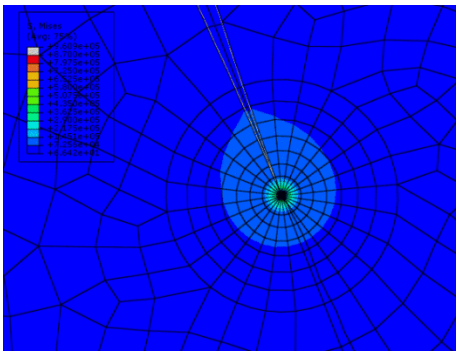

Figure 29. Mises stress around the crack tip of X52 steel SNTT sample with notch-to-diameter ratio of 0.45.

Table 3. Results of 1.0 inch diameter steel SNTT sample with applied angle 0.0015 rad.

a/D	Theta (rad)	Torque (lbf-in)	G (lbf/in)	K_1 (psi√in)	K_2 (psi√in)	K_3 (psi√in)
0.10	0.0015	5146.59	9.132	17259	-0.7358	2240
0.15	0.0015	4902.25	12.02	18888	-0.9838	5891
0.20	0.0015	4621.96	13.6	18421	-0.732	9377
0.25	0.0015	4322.82	14.45	16641	-0.9354	12452
0.30	0.0015	4016.23	14.77	13951	-0.687	14905

0.35	0.0015	3712.19	14.58	10598	-0.7397	16572
0.40	0.0015	3419.65	13.89	6837	-0.5092	17353
0.45	0.0015	3145.92	12.81	3231	-10.03	17363

Table 4. Results of 1.0 inch diameter steel SNTT sample with applied torque 5000 lbf-in.

a/D	Torque (lbf-in)	Theta (rad)	G (lbf/in)	K_1 (psi√in)	K_2 (psi√in)	K_3 (psi√in)
0.10	5000	0.00146	8.62	16767	-0.7148	2177
0.15	5000	0.00153	12.5	19264	-1.003	6008
0.20	5000	0.00162	15.91	19928	-0.7918	10144
0.25	5000	0.00173	19.33	19248	-1.082	14403
0.30	5000	0.00187	22.89	17369	-0.8552	18556
0.35	5000	0.00202	26.45	14274	-0.9966	22322
0.40	5000	0.00219	29.7	9996	-0.7446	25373
0.45	5000	0.00238	32.38	5135	-15.95	27596

Table 5. Results of 1.0 inch diameter aluminum SNTT sample with applied angle 0.002 rad.

a/D	Theta (rad)	Torque (lbf-in)	G (lbf/in)	K_1 (psi√in)	K_2 (psi√in)	K_3 (psi√in)
0.10	0.002	2289.08	5.345	7837	-0.0074	993
0.15	0.002	2181.42	7.158	8660	-0.225	2610
0.20	0.002	2056.81	8.149	8493	-0.1556	4157
0.25	0.002	1923.32	8.67	7706	-0.307	5523
0.30	0.002	1786.33	8.856	6494	-0.2575	6614
0.35	0.002	1650.49	8.719	4972	-0.3195	7357
0.40	0.002	1519.94	8.282	3256	-0.2377	7705
0.45	0.002	1398.05	7.604	1606	-4.983	7712

Table 6. Results of 1.0 inch diameter aluminum SNTT sample with applied torque 2500 lbf-in.

a/D	Torque (lbf-in)	Theta (rad)	G (lbf/in)	K_1 (psi√in)	K_2 (psi√in)	K_3 (psi√in)
0.10	2500	0.00218	6.376	8559	-0.0081	1084
0.15	2500	0.00229	9.401	9925	-0.2579	2991
0.20	2500	0.00243	12.04	10323	-0.1891	5052
0.25	2500	0.0026	14.65	10016	-0.399	7179
0.30	2500	0.0028	17.35	9089	-0.3602	9256
0.35	2500	0.00303	20.01	7532	-0.4839	11143
0.40	2500	0.00329	22.41	5356	-0.391	12673
0.45	2500	0.00358	24.32	2871	-8.91	13791

Table 7. Results of 0.375 inch diameter steel SNTT sample with applied angle 0.002 rad.

a/D	Theta (rad)	Torque (lbf-in)	G (lbf/in)	K_1 (psi√in)	K_2 (psi√in)	K_3 (psi√in)

0.10	0.002	353.351	5.948	13849	-1.388	1903
0.15	0.002	336.579	7.828	15185	-1.647	4853
0.20	0.002	317.337	8.857	14835	-1.712	7655
0.25	0.002	296.797	9.41	13431	-1.481	10113
0.30	0.002	275.749	9.619	11299	-1.293	12062
0.35	0.002	254.922	9.494	8982	-0.2912	13643
0.40	0.002	234.784	9.044	5642	-0.6431	13962
0.45	0.002	215.993	8.341	2639	-0.3112	13853

Table 8. Results of 0.375 inch diameter steel SNTT sample with applied torque 5000 lbf-in.

a/D	Torque (lbf-in)	Theta (rad)	G (lbf/in)	K_1 (psi√in)	K_2 (psi√in)	K_3 (psi√in)
0.10	300	0.0017	4.288	11758	-1.178	1615
0.15	300	0.00178	6.219	13534	-1.468	4325
0.20	300	0.00189	7.915	14024	-1.619	7237
0.25	300	0.00202	9.614	13576	-1.497	10222
0.30	300	0.00218	11.39	12292	-1.407	13122
0.35	300	0.00235	13.15	10570	-0.3423	16056
0.40	300	0.00256	14.77	7210	-0.8217	17840
0.45	300	0.00278	16.09	3665	-0.4324	19241

Table 9. Results of 0.375 inch diameter aluminum SNTT sample with applied angle 0.002 rad.

a/D	Theta (rad)	Torque (lbf-in)	G (lbf/in)	K_1 (psi√in)	K_2 (psi√in)	K_3 (psi√in)
0.10	0.0025	150.90	3.13	6036.00	-0.01	809.20
0.15	0.0025	143.80	4.20	6683.00	-0.27	2065.00
0.20	0.0025	135.59	4.78	6566.00	-0.40	3259.00
0.25	0.0025	126.79	5.08	5971.00	-0.41	4308.00
0.30	0.0025	117.76	5.19	5050.00	-0.43	5140.00
0.35	0.0025	108.82	5.11	4048.00	0.00	5818.00
0.40	0.0025	100.20	4.85	2580.00	-0.28	5953.00
0.45	0.0025	92.16	4.46	1258.00	-0.13	5908.00

Table 10. Results of 0.375 inch diameter steel SNTT sample with applied torque 5000 lbf-in.

a/D	Torque (lbf-in)	Theta (rad)	G (lbf/in)	K_1 (psi√in)	K_2 (psi√in)	K_3 (psi√in)
0.10	150	0.00249	3.10	6000.00	-0.01	804.40
0.15	150	0.00261	4.57	6971.00	0.28	2154.00
0.20	150	0.00277	5.85	7264.00	-0.44	3605.00
0.25	150	0.00296	7.12	7065.00	-0.48	5097.00
0.30	150	0.00318	8.42	6432.00	-0.54	6548.00
0.35	150	0.00345	9.71	5579.00	0.00	8020.00
0.40	150	0.00374	10.88	3862.00	-0.42	8913.00

0.45	150	0.00407	11.81	2047.00	-0.21	9616.00

3.3.6 Analytical models

3.3.6.1 The evolution of compliance and fracture resistance in SNTT process

Systematic studies reveal that an SNTT-type specimen (a rod-type specimen having a helical groove with a 45-degree pitch) can effectively simulate the behavior of a thick compact-tension specimen equal to the total length of the groove line. Careful studies show that the evolutions of compliance and fracture resistance of the SNTT sample during the crack growth process can be unified together irrespective of specimen sizes and material types. In addition to the special features of small volume specimen and ease of testing with the SNTT method, the independence of size effect is in rigorous analytical results for this testing method. The evolution of compliance and fracture resistance in the SNTT process has also been presented with simple governing equations using the ratios of crack lengths over the cylindrical diameter. Based on the measured torques and rotation angles, the penetrated crack depth can be obtained through compliance governing equations. Once crack depths are known, the energy release rates, i.e., the crack driving force, can be obtained from the fracture resistance equation for the SNTT experiments. Therefore, it is possible to control the crack penetration depth in SNTT experiments via monitoring the applied torques and angles, a technique easily adapted by industry. The governing equations will be published following final validations.

Figure 30a and Figure 30b chart the previous circular segmental section method in calculating compliance of the SNTT crack growth process. Figure 31a and Figure 31b display the one keyway shaft method in calculating compliance of the SNTT crack growth process. Figure 32 shows the evolution of crack growth in an SNTT sample with a cylinder diameter of 1 inch. where a is the crack length and D is the diameter. The ratio of crack length over diameter increases from 0.10 to 0.45. The length of each model is the same during the crack growth process. Figure 32a shows the compliance evolution of the SNTT sample with respect to different ratios of crack length over diameter. To obtain a more sensitive response of the compliance evolution, a factor was applied to account for the effect of unbroken ligament of the SNTT samples, which is graphed in Figure 32b. It shows that the compliance evolution curves are the same for specimens with different materials or sizes. γ is the unit end rotation angle; T is the applied torque; μ is the shear modulus; and R is the cylinder radius. Figure 33a shows the fracture resistance evolution of the SNTT sample with respect to crack length over diameter ratios. In order to obtain a more sensitive response of the compliance evolution, a factor also was applied to account for the effect of unbroken ligament of the SNTT samples, which is shown in Figure 33b. It was noted that fracture resistance curves are the same for specimens with different materials or sizes. G is the energy release rate; T is the applied torque; θ is the associated rotation angle; A is the cross section area of the cylinder.

(a)

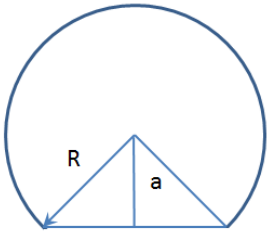

(b)

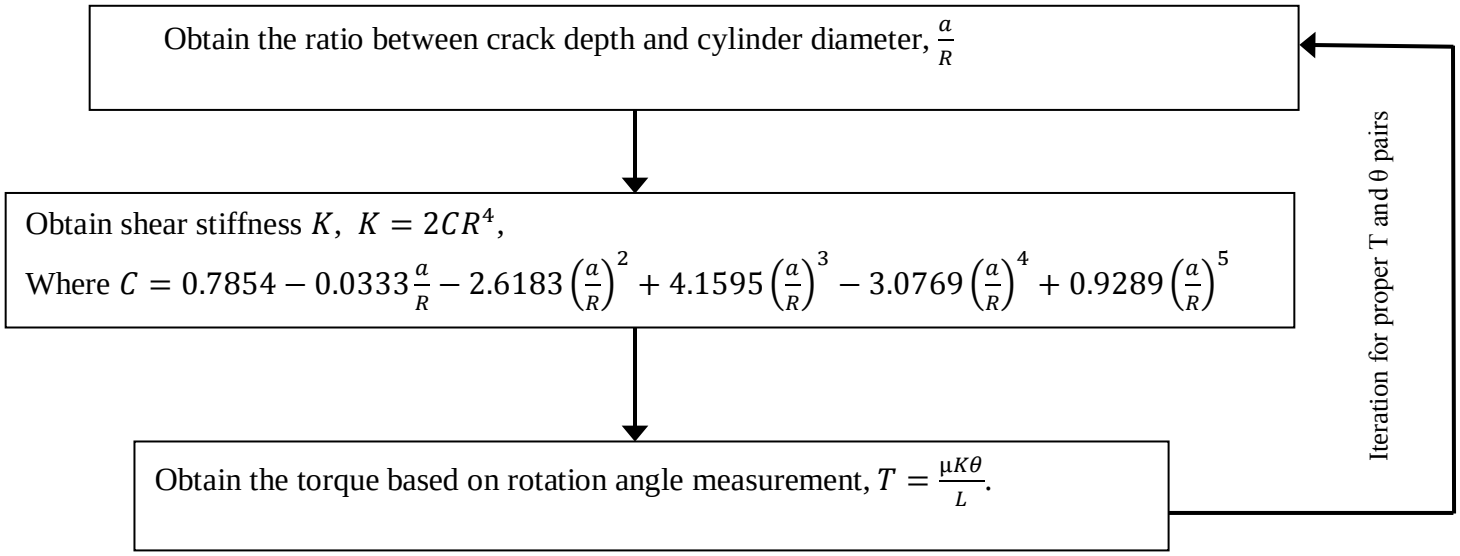

Figure 30. Circular segmental section calculations of crack growth in SNTT process.

(a)

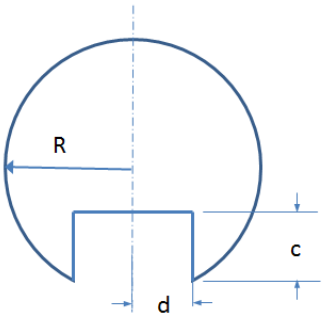

(b)

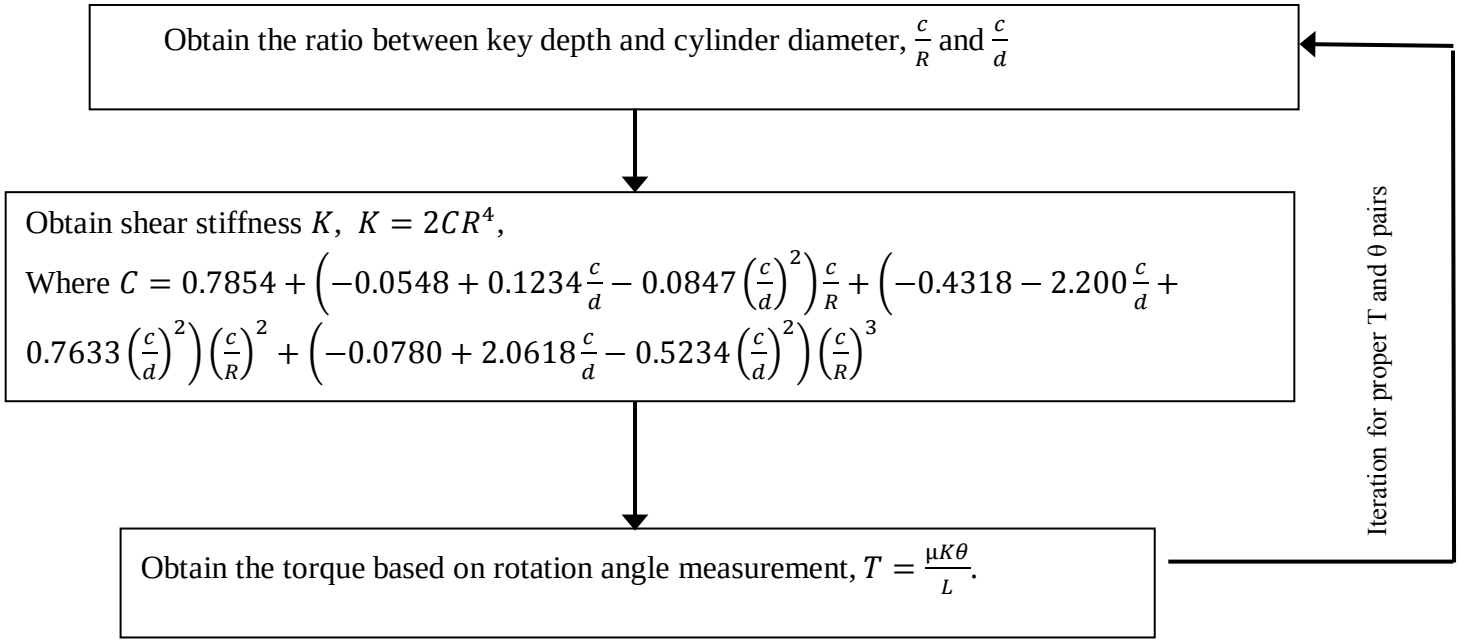

Figure 31. Shaft with one keyway calculations of crack growth in SNTT process.

(a)

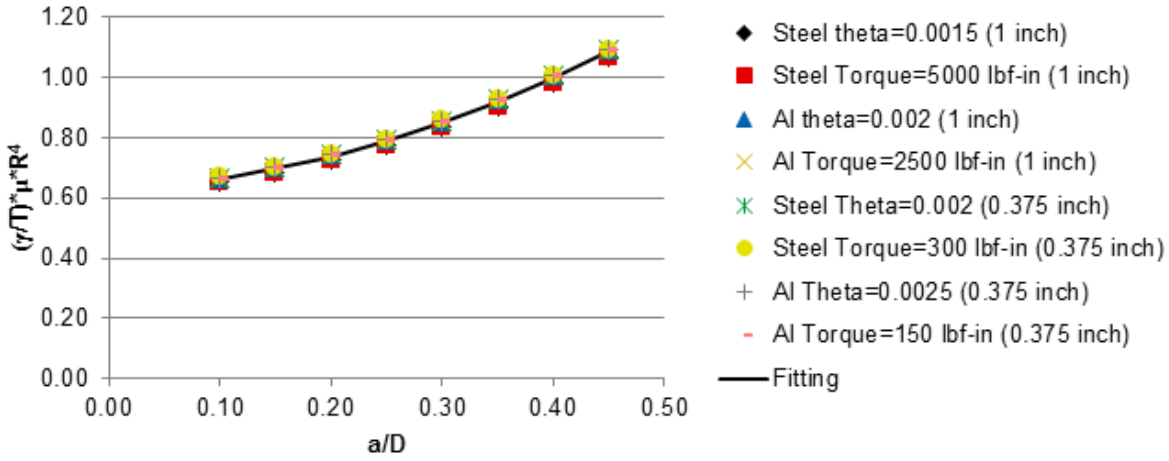

(b)

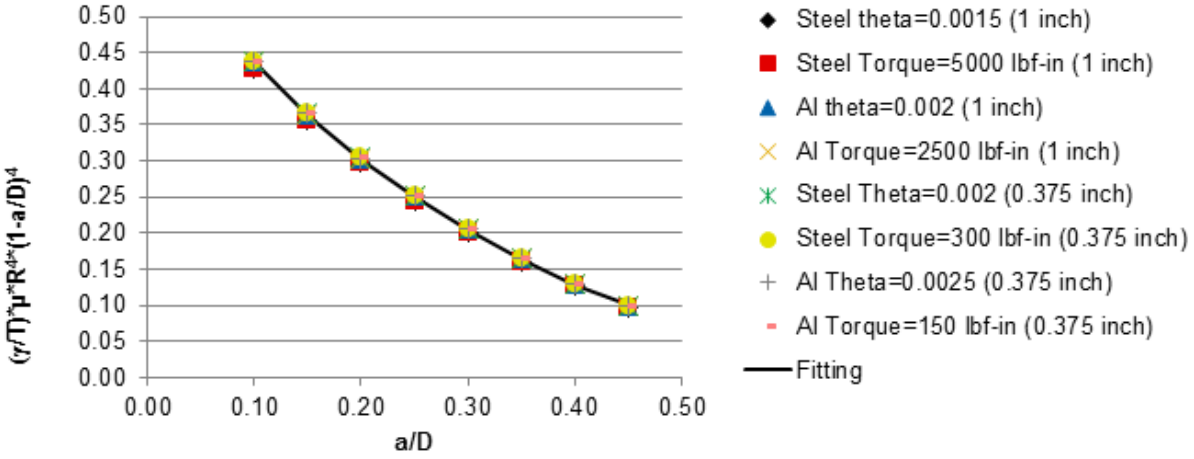

Figure 32. (a) The unscaled compliance evolution with the crack growth; (b) The scaled compliance evolution along the crack growth with unbroken ligament factor.

(a)

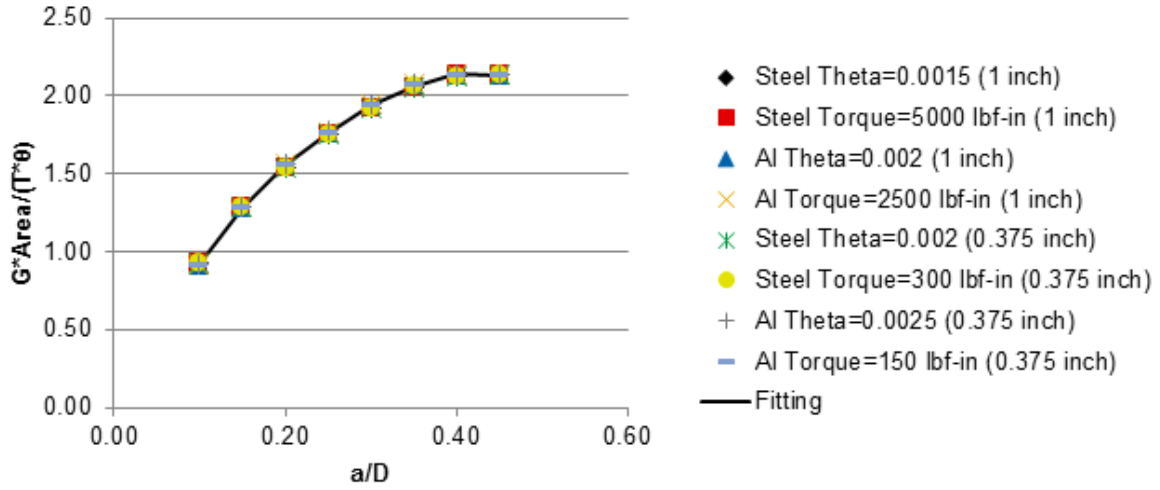

(b)

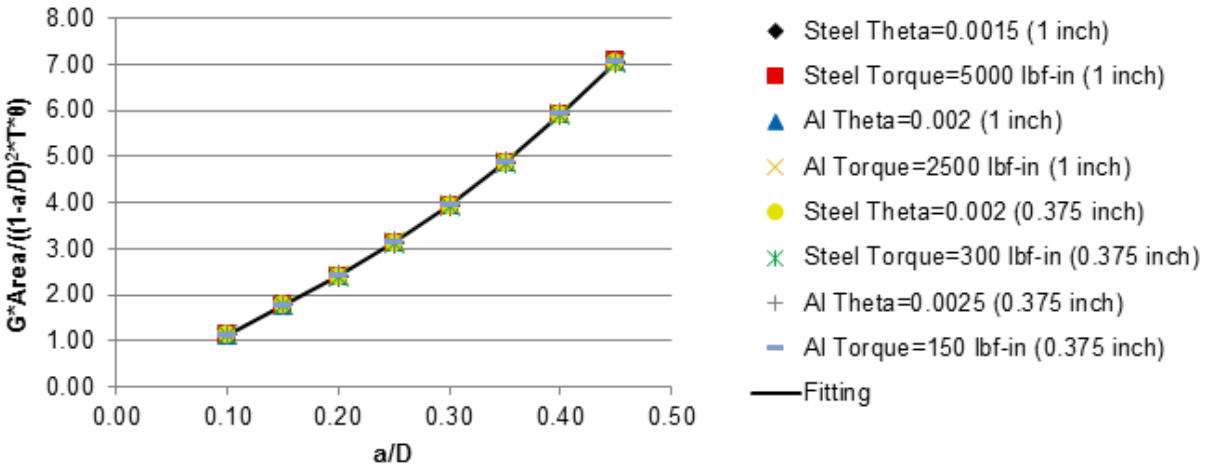

Figure 33. (a) The unscaled energy release rate evolution with the crack growth; (b) The scaled energy release rate evolution along the crack growth with unbroken ligament factor.

4. In Air Spiral Notch Torsion Test of X52 steel

4.1 Sample design and fabrication

The SNTT technique has been successfully applied to various types of materials, including metals, ceramics, polymers and composites [Wang 2000, Wang 2002, Wang 2011]. During the first quarter of FY2011, an extensive study was performed to test 4340 steel [Wang 2011]. Further effort built on previous work to develop new specimen and fixture design. This work was performed primarily by research staff in the Materials Science and Technology Division, Oak Ridge National Laboratory. The design details for specimens and fixtures are discussed in the following sections.

4.1.1 X52 sample design

In this approach, X52 SNTT samples were fabricated from a segment of friction stir welded X52 steel pipe. Since the thickness of the pipe is 0.5 inch, the diameter of the SNTT cylinder was designed to be 0.375 inch (Figure 34) The SNTT specimen axis was parallel to the pipe cylinder axis (Figure 35). Only one entire loop was machined in the X52 SNTT sample. Threads were introduced onto both ends of the X52 SNTT samples.

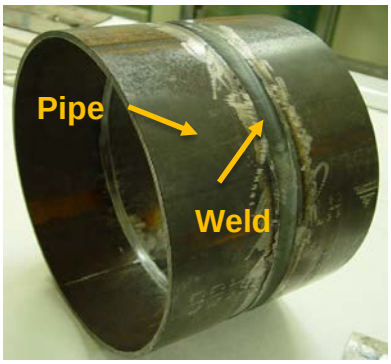

Figure 34. Actual dimension of Friction Stir Welded X52 steel pipe.

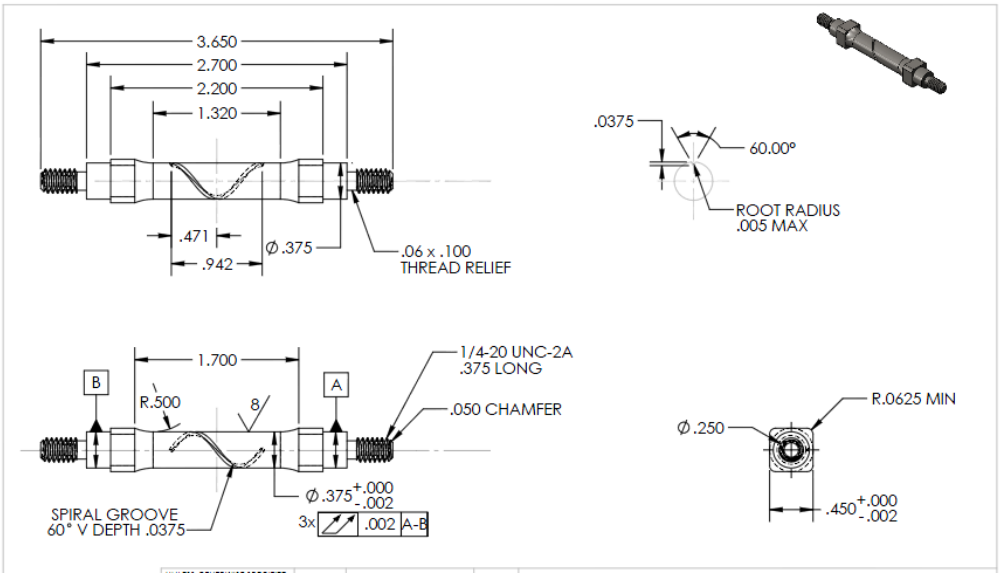

Figure 35. Geometry details of the X52 steel SNTT specimen.

4.1.2 X52 SNTT sample fixture design

Two major concerns were addressed in the fixture and base design of X52 SNTT samples. Because a high number of cycles were involved in the pre-fatigue crack process, threads could be coupled with bolts to stabilize the specimens. Therefore, small fixtures were designed separated to accommodate the X52 SNTT samples (Figure 36). In the meantime, In addition, a base was designed to connect the X52 specimen fixture to the MTS machine (Figure 37). In both the fixture and base, rotated bolt arrays were applied to secure the fastening between different components.

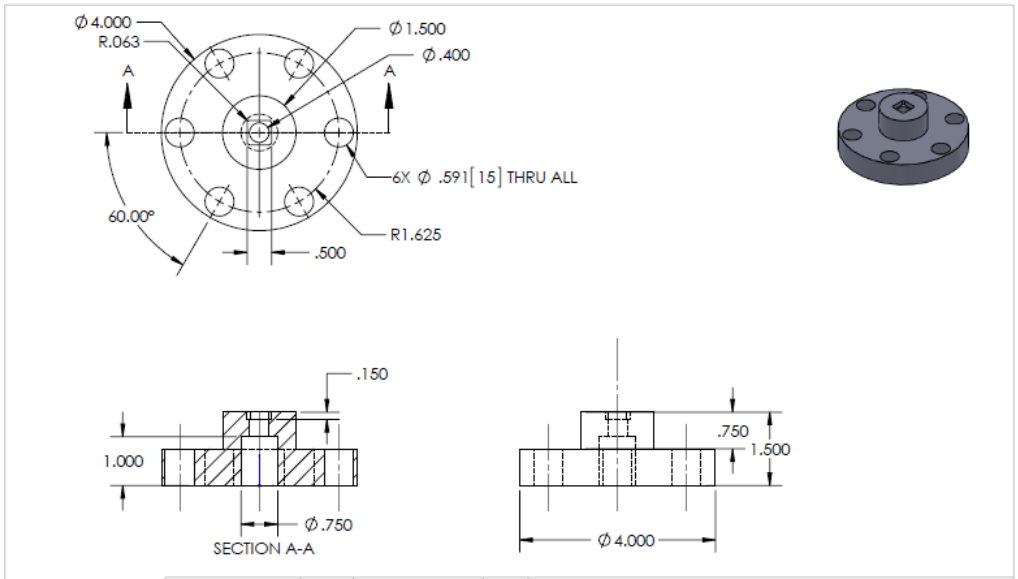

Figure 36. Schematic for fixture to adapt the X52 SNTT specimen.

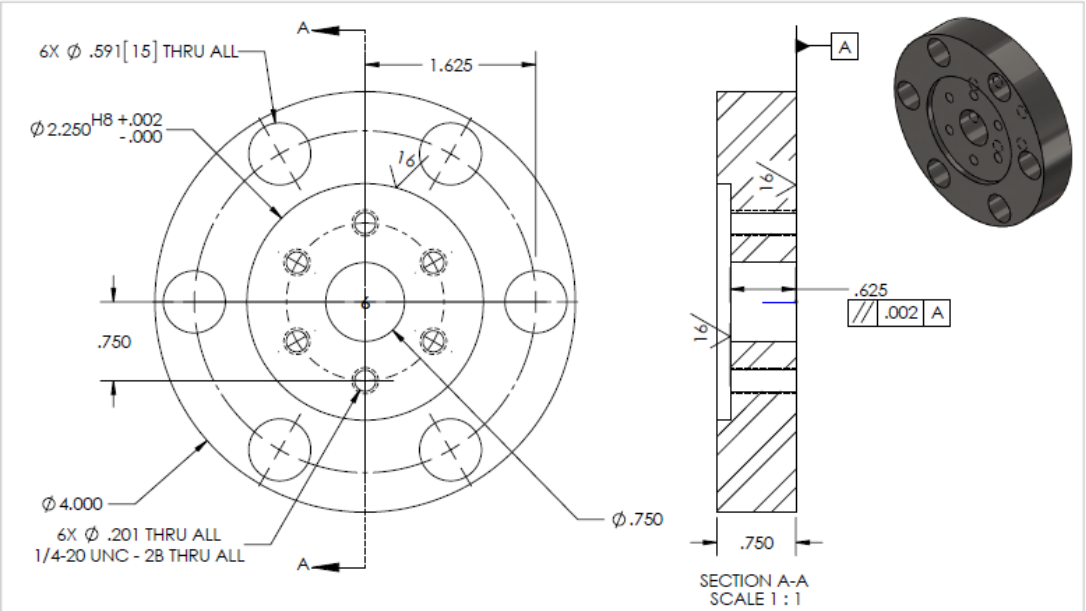

Figure 37. Schematic for base to adapt the X52 SNTT fixture.

4.2 SNTT equipment setup

To date, the SNTT testing of X52 steel has been focused on samples machined from the bulk material of friction stir welded pipe (see Section 4.1.1). Preliminary calculations estimate that the threshold of crack initiation in these samples is around 380 lbf-in. The maximum capacity of the load/torque cell on the MTS 809 machine is 10,000 lbf-in. The cyclic fatigue frequency also covers from 0.1 HZ to 10 HZ. These specifications ensure that cycle fatigue testing of SNTT X52 steel specimens can be conducted.

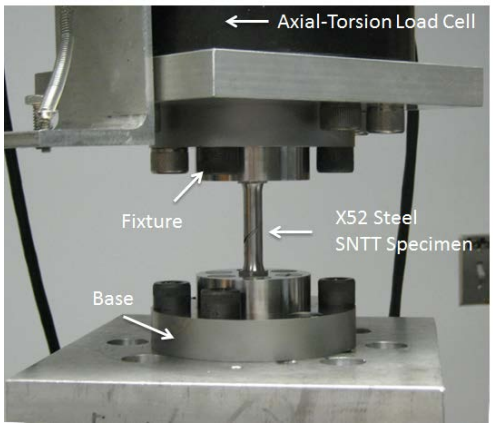

Figure 38. SNTT testing setup of X52 steel specimen.

4.3 In air SNTT testing of X52 steel base materials

4.3.1 X52 base material sample B1

4.3.1.1 Cycle fatigue process

The cycle fatigue process sample B1 was performed through the angle control mode by a function generator built in the MTS system. In order to find the fatigue threshold of the X52 SNTT samples, the initial maximum torque was adjusted to approximately 220 lbf-in with 5 HZ cyclic fatigue process. This cyclic load was increased to 300 lbf-in after 350,000 cycles to facilitate the crack growth. This torque was increase to 340 lbf-in after ~ 440,000 cycles. After this increment, the dynamic torque decreased quickly to 128 lbf-in within a few hours, indicating that an accelerated crack penetration. B1 sample fractured into two halves during the cycle fatigue process.

Table 11. The monitoring process of B1 sample through a function generator

Date	Time (EST)	Mean (degree)	Amplitude (degree)	Freq	Torque (lbf-in)		Theta (degree)		Count	Note
					Peak	Valley	Peak	Valley		
03/24/12	16:00	16.50	1.00	5	210.40	40.79	17.00	16.00		
03/24/12	20:30	16.50	1.00	5	218.00	16.00	17.00	16.00		
03/25/12	10:30	16.50	1.00	5	222.00	39.00	17.00	16.00	350,695	
03/25/12	10:40	17.00	1.50	5	297.00	25.00	17.75	16.25		
03/25/12	13:42	17.00	1.50	5	287.00	14.50	17.75	16.25	404,316	
03/25/12	16:36	17.00	1.50	5	285.00	13.60	17.75	16.25	438,280	
03/25/12	16:38	17.50	1.50	5	332.00	56.00	18.25	16.75		
03/25/12	16:40	17.50	1.75	5	341.00	24.00	18.37	16.62		
03/25/12	17:30	17.50	1.75	5	332.00	20.00	18.37	16.62		Restart MTS
03/25/12	20:50	17.50	1.75	5	128.00	-12.00	18.37	16.62		

4.3.1.2 Failed sample characterization

The failed B1 samples were characterized using an optical camera (Canon EOS rebel T2i, Lake Success, NY), which captured optical images of the specimen (Figure 39a) and the fractured surfaces (Figure 39b). From Figure 39a, it can be seen that the B1 sample split into two halves during the cycle fatigue process. The failed surfaces were smooth and rotated along spiral grooves. During examination of the failed surface, it was noticed there were some defects located within the X52 base material (Figure 39b). This will have to be taken into account in future X52 material development.

Figure 39. Failed B1 specimen in X52 base steel series.

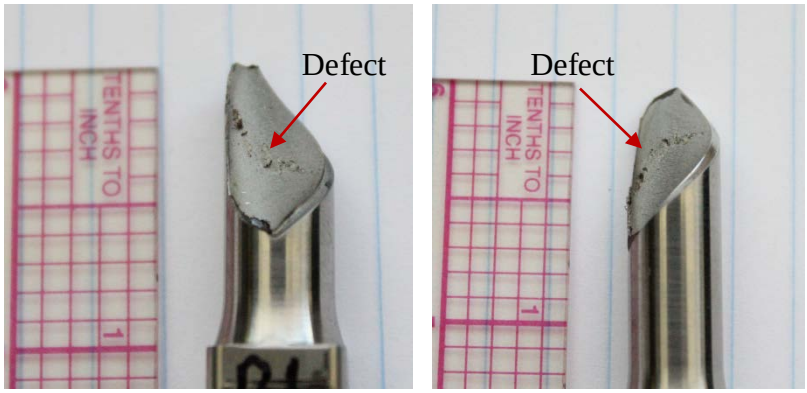

(a) (b)

Figure 39. Higher resolution image of failed B1 specimen of X52 base steel sample series.

4.3.2 X52 base material sample B2

4.3.2.1 Cycle fatigue process

The cycle fatigue process (Table 12) of sample B2 was also conducted through the angle control mode by the same function generator built in the MTS system. In order to find the fatigue threshold of the X52 SNTT samples, the initial maximum torque was adjusted to around 250 lbf-in 5 HZ cyclic fatigue process. This cyclic load was increased to 250 lbf-in after 460,000 cycles to facilitate crack growth, then to 290 lbf-in after ~910,000 cycles, and finally to 330 lbf-in after 1 million cycles. After the final adjustment to 320 lbf-in at 1.2 million cycles, the dynamic torque decreased quickly to 135 lbf-in with a fast crack penetration.

Table 12. The monitoring process of B2 sample through a function generator

Date	Time (EST)	Mean (degree)	Amplitude (degree)	Freq	Torque (lbf-in)		Theta (degree)		Count
					Peak	Valley	Peak	Valley	
03/26/12	10:43	2.75	1.00	5	217.71	24.32	3.25	2.25	
03/26/12	14:48	2.75	1.00	5	216.50	24.32	3.25	2.25	
03/26/12	17:34	2.75	1.00	5	217.00	24.31	3.25	2.25	140,900
03/27/12	9:14	2.75	1.00	5	220.00	27.37	3.25	2.25	
03/27/12	9:47	2.90	1.15	5	256.00	33.16	3.47	2.32	
03/27/12	11:42	2.90	1.15	5	254.00	31.33	3.47	2.32	466,000
03/27/12	15:45	2.90	1.15	5	253.00	29.89	3.47	2.32	539,000
03/27/12	17:54	2.90	1.15	5	250.30	27.97	3.47	2.32	576,800
03/28/12	9:08	2.90	1.15	5	247.90	24.90	3.47	2.32	851,400
03/28/12	9:41	3.10	1.25	5	285.40	40.80	3.72	2.48	859,500
03/28/12	10:54	3.10	1.25	5	281.50	36.00	3.72	2.48	881.400
03/28/12	12:27	3.10	1.25	5	281.50	36.40	3.72	2.48	909,100
03/28/12	12:31	3.15	1.30	5	294.00	39.60	3.80	2.50	
03/28/12	13:28	3.15	1.30	5	291.00	36.50	3.80	2.50	926,700
03/28/12	14:31	3.15	1.30	5	290.00	36.00	3.80	2.50	945,300
03/28/12	15:40	3.15	1.30	5	289.90	36.00	3.80	2.50	966,300
03/28/12	15:47	3.30	1.35	5	314.70	49.60	3.97	2.62	
03/28/12	17:05	3.30	1.35	5	310.00	44.10	3.97	2.63	989,800
03/28/12	18:12	3.30	1.35	5	309.00	45.00	3.97	2.62	1,010,600
03/28/12	18:37	3.45	1.40	5	334.80	58.40	4.15	2.75	1,017,000
03/29/12	9:21	3.45	1.40	5	299.80	42.92	4.15	2.75	1.283,000
03/29/12	9:27	3.60	1.45	5	324.00	57.50	4.32	2.87	
03/29/12	10:45	3.60	1.45	5	236.00	22.18	4.32	2.87	1,306,000
03/29/12	10:51	3.60	1.45	5	221.00	16.38	4.32	2.87	
03/29/12	11:06	3.60	1.45	5	188.00	3.27	4.32	2.87	1,312,500
03/29/12	11:08	3.60	1.45	5	135.00	-10.17	4.32	2.87	1,317,100

4.3.2.2 Monotonic loading test

B2 sample was then loaded monotonically in the MTS machine with a loading rate of 20 lbf-in/second. The load was increased to ~ 300 lbf-in during testing (Figure 1a). When the load reached ~100 lbf-in, the sample yielded (Figure 40b).

4.3.2.3 Failed sample characterization

Images of failed B2 samples are shown in Figure 41. In Figure 41a, it can been seen that the B2 sample did not split into two halves during the monotonic loading tests. In Figure 41b, smooth fatigue areas can be detected in the opened specimen. Also, a tensile stress area occurred around the fatigue crack front, which was due to the monotonic loading tensile test. The B1 sample of X52 material is tough enough to resist quick failure even after the fatigue process.

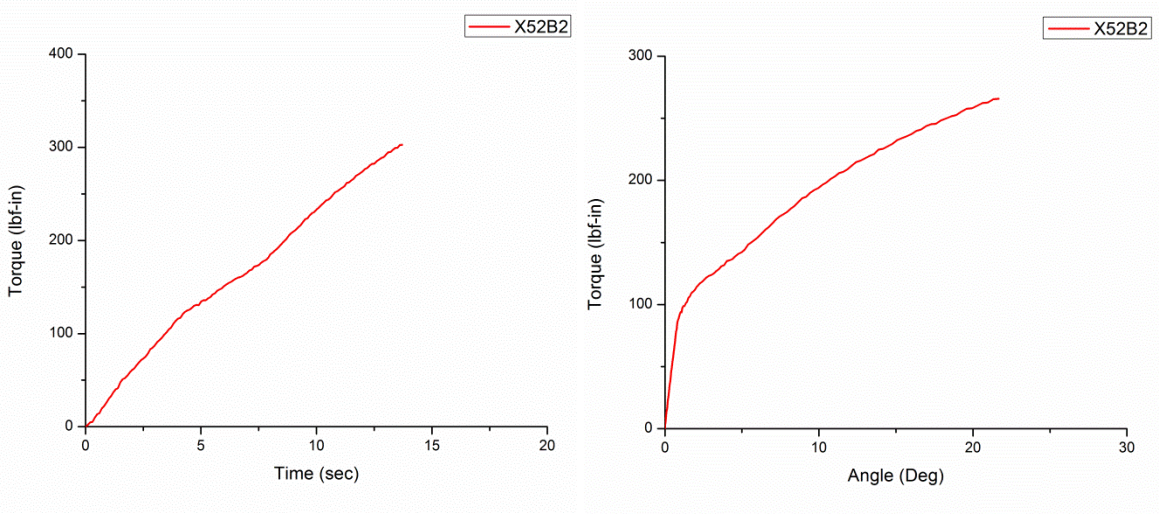

(a) (b)

Figure 40. Loading curves for the B2 sample during the monotonic loading test: (a) load versus time; (b) load versus angle.

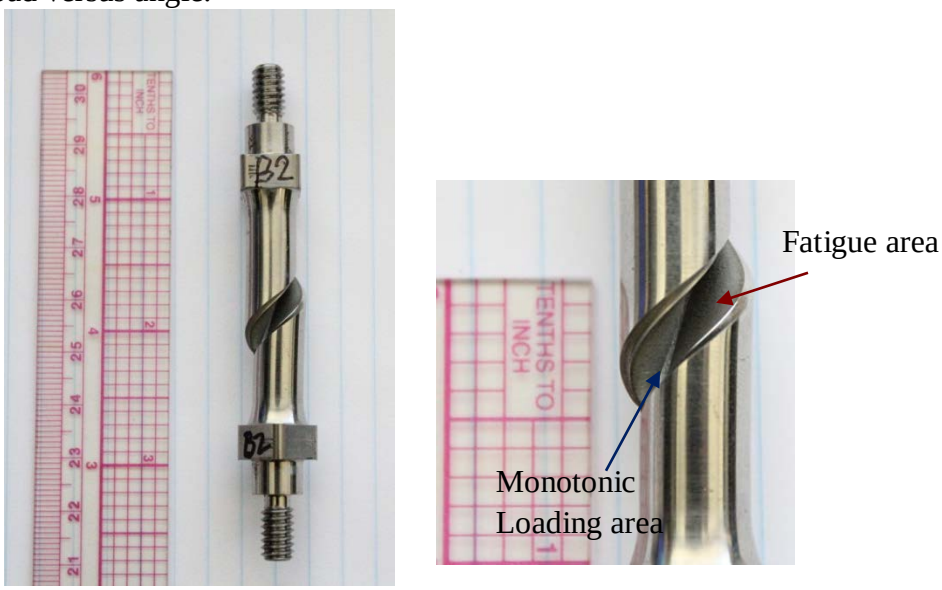

(a) (b)

Figure 41. The failed B2 specimen of X52 base sample series. (a) entire view; (b) local area in the middle section of the SNTT cylinder.

4.3.3 X52 base material sample B3

4.3.3.1 Cycle fatigue process

The cycle fatigue process (Table 13) of sample B3 was also performed through the angle control mode by the built-in MTS function generator. Initial maximum torque was adjusted to around 300 lbf-in 5 HZ cyclic fatigue process. This cyclic load was increased to 320 lbf-in after 50,000 cycles to facilitate crack growth. The cyclic fatigue loading process ended when the dynamic torque decreased to ~50 lbf-in.

Table 13. The monitoring process of B3 sample through a function generator

Date	Time (EST)	Mean (degree)	Amplitude (degree)	Freq	Torque (lbf-in)		Theta (degree)		Count	Notice
					Peak	Valley	Peak	Valley		
03/29/12	16:33	9.70	1.15	5	297.33	66.7	10.20	9.10		
03/29/12	18:00	9.70	1.15	5	296.40	64.50	10.25	9.10	24,500	
03/29/12	18:05	9.75	1.15	5	306.10	74.00	10.32	9.17		
03/29/12	18:28	9.75	1.15	5	304.60	72.20	10.32	9.17	32,300	
03/30/12	9:07	9.75	1.15	5	263.80	56.60	10.32	9.17		
03/30/12	9:20	11.05	1.25	5	313.80	93.60	11.67	10.42	500	Restart MTS
03/30/12	11:16	11.05	1.25	5	127.00	0.00	11.67	10.42	31,100	
03/30/12	11:31	11.05	1.25	5	66.40	-10.76	11.67	10.42	35.600	
03/30/12	11:39	11.05	1.25	5	54.20	-10.76	11.67	10.42	37,900	
03/30/12	11:45	11.05	1.25	5	51.16	-10.76	11.67	10.42		

4.3.3.2 Monotonic loading test

A B3 sample was then loaded monotonically in the MTS machine with a loading rate of 20 lbf-in/second. The load was increased to ~ 200 lbf-in during test (Figure 42a). Figure 42b shows that the linear range of the X52 material is below 50 lbf-in. At higher loads a very nonlinear load-displacement curve is observed for the X52 base material B3 sample.

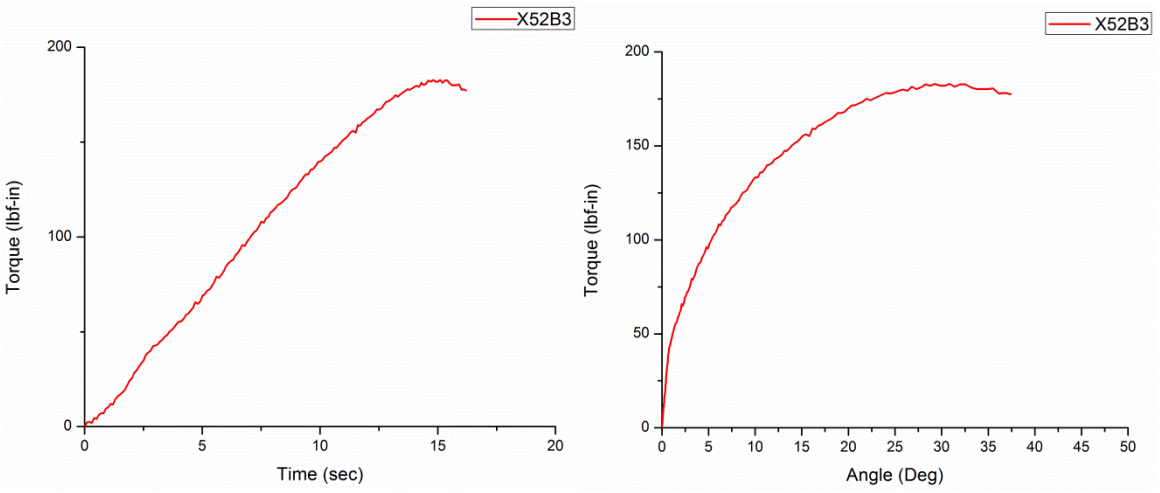

(a) (b)

Figure 42. The loading curves for B3 sample during the monotonic loading test: (a) load versus time; (b) load versus angle.

4.3.3.3 Failed B3 sample characterization

The images of the failed B3 samples are shown for a specimen that sample split into two halves after the monotonic loading tests (Figure 43). In Figure 44a and Figure 44b, defect areas can be observed among the smooth fatigue areas for the base material sample, and a monotonic loading area can be clearly detected beyond the fatigue crack front. The half in Figure 44b was observed using an optical microscope (SZH10, Olympus, Japan). The defect area and surrounding fatigue area in the failed B3 sample can be clearly detected in Figure 45. Three locations in this sample were selected for further scanning microscopy analysis (discussed in a later section).

Figure 43. The failed B3 specimen in X52 base steel series.

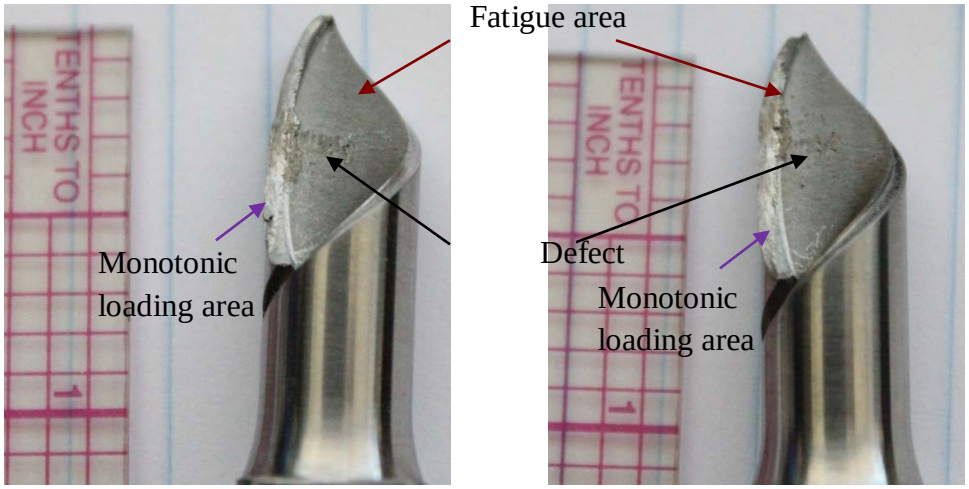

(a) (b)

Figure 44. The failed B3 specimen with higher resolution (a) one half of failed B3; (b) the other half of the failed B3.

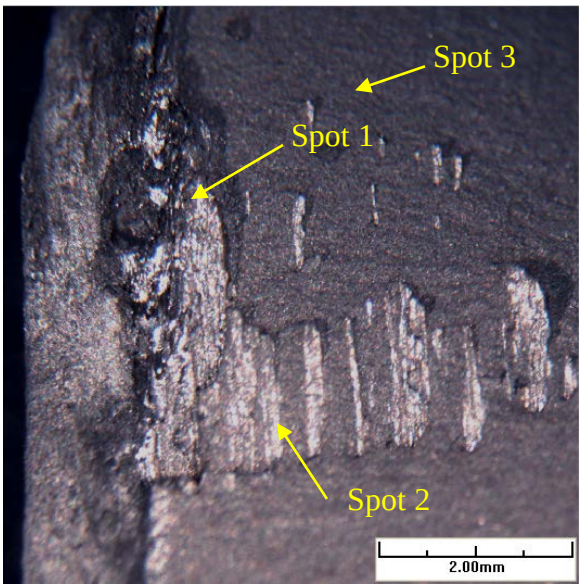

Figure 45. Fracture surface characterization by optical image of the defect area shown in Figure 44b.

Scanning electron microscopy (S3400, Hitachi, Japan) was used to characterize the fracture surfaces in Figure 45. In spots 1 and 2, striations can be detected in the defect areas (Figure 46). However, characterization of spot 3 (Figure 47) showed no clear striation for the B3 smooth fatigue area, which covered most of the two halves.

The transition area between the fatigue crack front and the monotonic loading area was also characterized in SEM images (Figure 48 and Figure 49). The difference between these two areas can also be noticed by these preliminary SEM analyses. The fatigue area is smoother than the monotonic loading areas. When the monotonic load was applied, the crack started penetrating into the unbroken ligament of the SNTT sample from the fatigue crack front. The yielding of the material also blunted the crack front. When the sample finally failed, evidence of monotonic failure can be observed from the fracture surface (Figure 50).

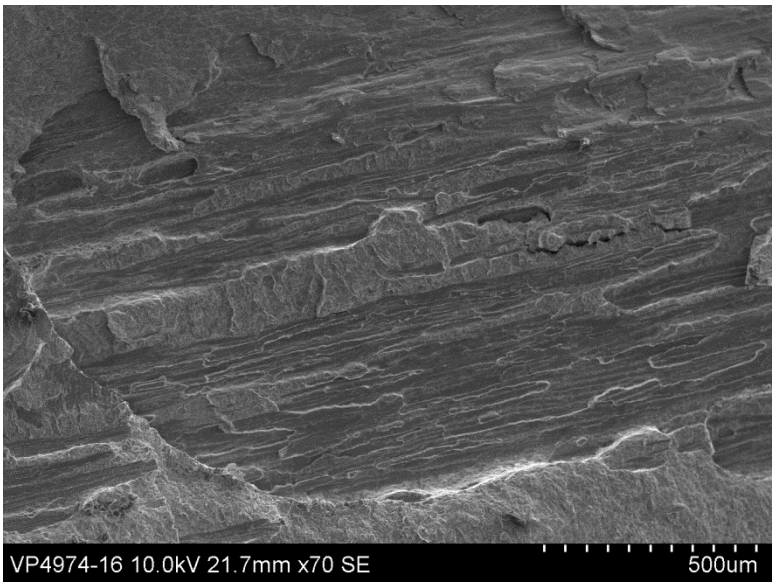

(a)

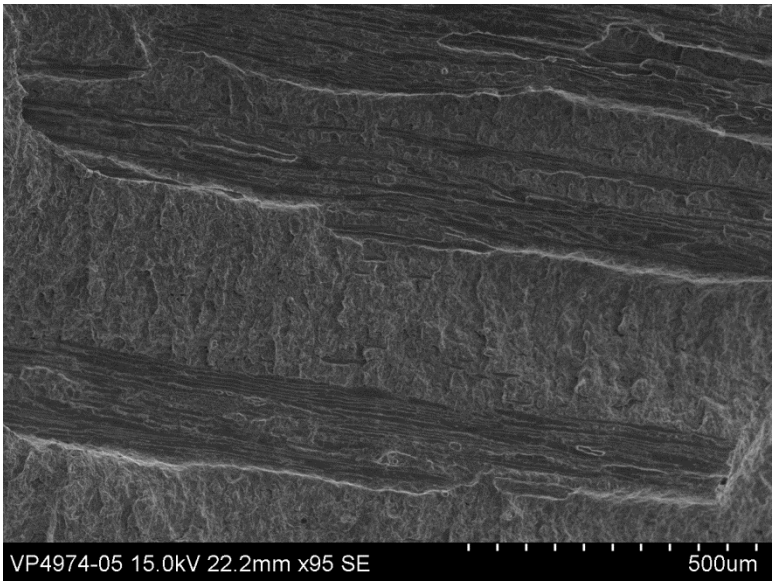

(b)

Figure 46. SEM images of the defect area in Figure 45. (a) spot 1; (b) spot 2.

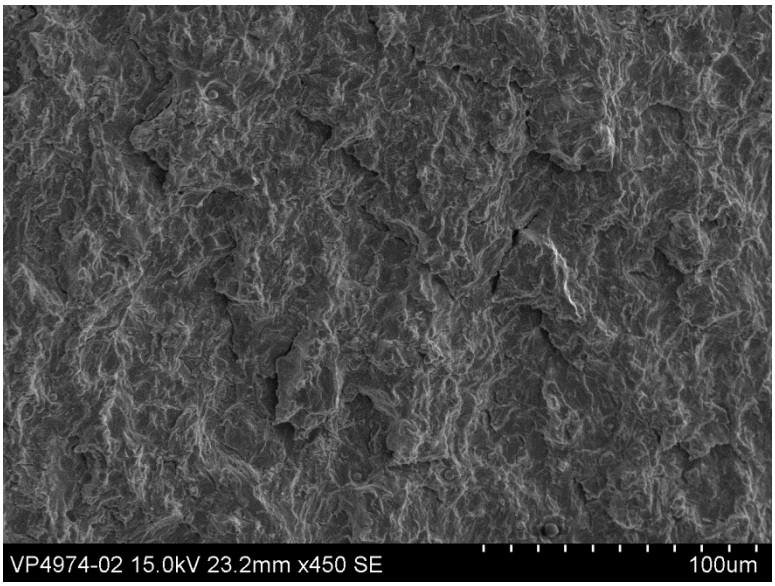

Figure 47. SEM image of the fatigue area around spot 3 in sample B3.

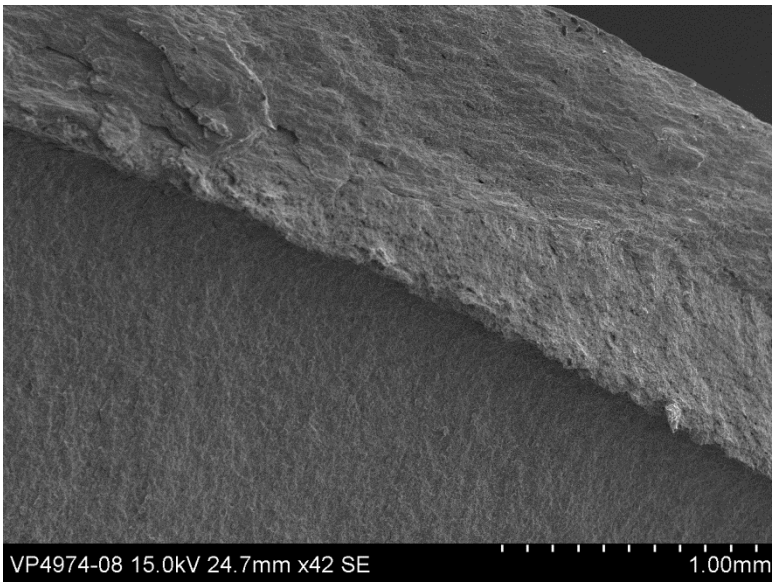

Figure 48. SEM image of the transitional area between the fatigue crack front and the monotonic loading area.

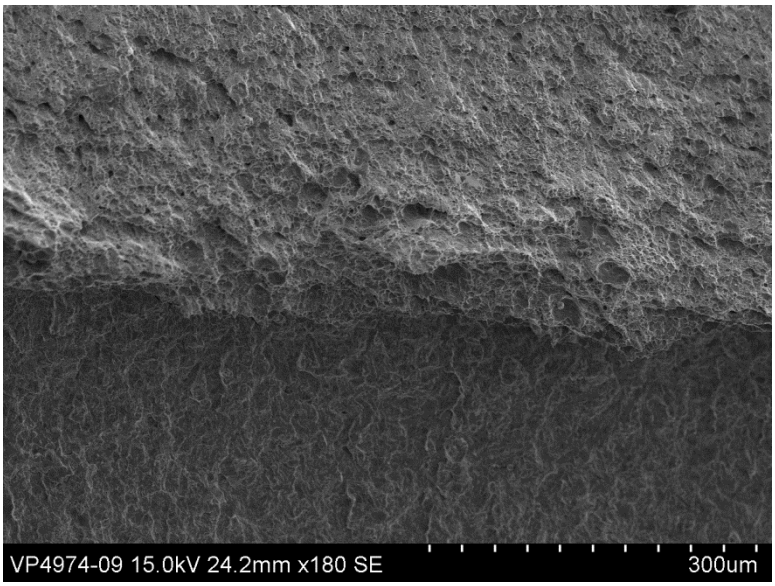

Figure 49. Higher resolution SEM image of sample B3 transitional area between fatigue crack front and monotonic loading area.

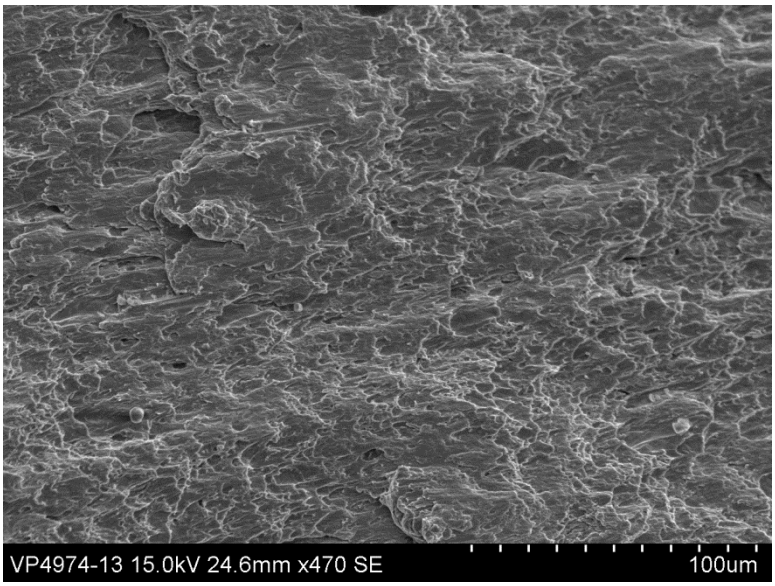

Figure 50. SEM image of the monotonic loading area in failed sample B3.

4.3.4 X52 base material sample B4

4.3.4.1 Cycle fatigue process

(Table 14) presents cycle fatigue process data for sample B4. The initial maximum torque was adjusted to around 300 lbf-in 5 HZ and then was increased to 360 lbf-in after 367,000 cycles to facilitate the crack growth, ending at 320 lbf-in after ~420,000 cycles. The cyclic fatigue loading process stopped when the sample failed through the entire fatigue process.

Table 14. The monitoring process of B4 sample through a function generator

Date	Time (EST)	Mean (degree)	Amplitude (degree)	Freq	Torque (lbf-in)		Theta (degree)		Count
					Peak	Valley	Peak	Valley	
03/30/12	12:45	9.30	1.35	5	302.21	35.00	9.97	8.62	500
03/30/12	13:39	9.30	1.35	5	302.80	31.00	9.97	8.62	
03/30/12	14:05	9.40	1.40	5	324.70	42.90	10.09	8.69	
03/30/12	14:46	9.40	1.40	5	322.30	40.80	10.09	8.69	
03/30/12	16:25	9.40	1.40	5	321.40	40.10	10.09	8.69	
03/30/12	16.46	9.45	1.40	5	330.80	49.00	10.15	8.75	66,000
03/30/12	17:10	9.45	1.40	5	329.80	47.50	10.15	8.75	78,000
03/30/12	17:40	9.45	1.40	5	329.60	47.10	10.15	8.75	
03/31/12	9:01	9.45	1.40	5	325.00	44.70	10.15	8.75	363,700
03/31/12	9:17	9.60	1.50	5	357.00	56.90	10.35	8.85	367,000
03/31/12	9:36	9.60	1.50	5	352.00	53.00	10.30	8.80	373,000
03/31/12	10:16	9.60	1.50	5	349.80	51.16	10.34	8.84	385,090
03/31/12	11:00	9.60	1.50	5	344.00	49.30	10.34	8.84	398,000
03/31/12	12:13	9.60	1.50	5	319.00	40.80	10.34	8.84	420,000
03/31/12	12:47	9.60	1.50	5	289.00	29.10	10.34	8.84	430,000
03/31/12	13:22	9.60	1.50	5	217.00	6.32	10.34	8.84	441,000
03/31/12	13:37	9.80	1.50	5	226.00	18.20	10.35	9.05	442,000
03/31/12	13:45	9.80	1.20	5	191.00	31.33	10.40	9.20	
03/31/12	13:58	9.80	1.20	5	152.70	18.20	10.40	9.20	449,000
03/31/12	14:06	9.80	0.70	5	123.10	44.45	10.15	9.45	
03/31/12	14:16	9.80	1.10	5	142.90	22.79	10.35	9.25	450,100
03/31/12	14:32	9.80	1.10	5	116.70	13.30	10.35	9.25	454,000
03/31/12	14:44	9.80	1.10	5	95.40	6.30	10.35	9.25	458,000
03/31/12	15:01	9.80	1.10	5	73.70	0	10.35	9.25	464,000
03/31/12	15:28	9.80	1.10	5	57.20	-2.52	10.35	9.25	471,700
03/31/12	15:58	9.80	1.10	5	50.20	-4.65	10.35	9.25	480,700
03/31/12	16:33	9.80	1.10	5	44.70	-5.57	10.35	9.25	491,000
03/31/12	17:15	9.80	1.10	5	40.70	-5.57	10.35	9.25	504,000
03/31/12	17:26	9.85	1.20	5	42.00	-5.57	10.45	9.25	
03/31/12	17:36	9.90	1.25	5	42.62	-4.35	10.52	9.27	507,200
03/31/12	18:10	9.90	1.25	5	36.80	-5.27	10.52	9.27	517,400
03/31/12	18:37	9.95	1.35	5	38.00	-3.74	10.62	9.27	524,000
03/31/12	19:02	10.00	1.40	5	35.30	-0.99	10.70	9.30	531,200
03/31/12	19:09	10.00	1.45	5	35.30	-1.60	10.70	9.30	532,700
03/31/12	19:20	10.00	1.45	5	13.00	0.52	10.72	9.27	538,300

4.3.4.2 Failed sample characterization

The images of the failed B4 sample appear in Figure 51, again splitting into two halves during the fatigue process. In Figure 52a, the fatigue crack front extends to the edge of the SNTT cylinder. There were no similar defect areas compared to those observed in sample B1 and B3. An addition cut was performed to one of the split halves to examine the crack penetration status on the edge of the spiral notch. No clear crack penetration was observed in the cross-section.

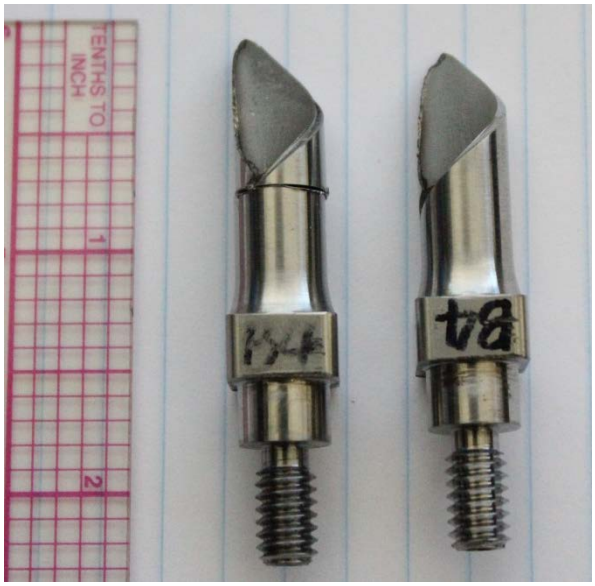

Figure 51. The failed B4 specimen in X52 base steel series.

(a) (b)

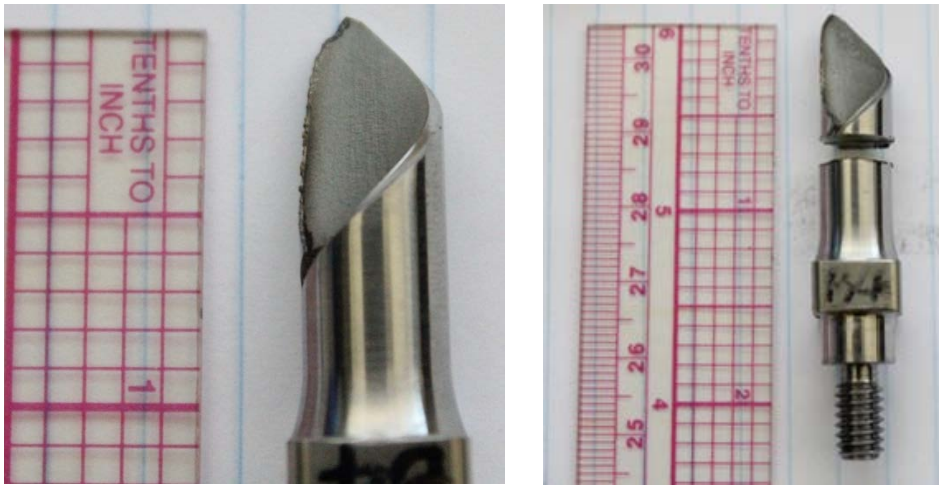

Figure 52. The failed B4 specimen with higher resolution (a) one half of failed B3; (b) the other half of the failed B4 with the cut.

4.3.5 X52 base material sample B5

4.3.5.1 Cycle fatigue process

The cycle fatigue process (Table 15) of sample B5 was also performed through the angle control mode by the same function generator built in the MTS system. The initial maximum torque was adjusted to around 300 lbf-in 5 HZ cyclic fatigue process. The cyclic fatigue loading process ended at ~ 2 million cycles before the sample was put into liquid nitrogen.

Table 15. The monitoring process of B5 sample through a function generator

Date	Time (EST)	Mean (degree)	Amplitude (degree)	Freq	Torque (lbf-in)		Theta (degree)		Count
					Peak	Valley	Peak	Valley	
04/04/12	08:45	0.20	1.45	5	295.20	7.06	0.92	-0.52	
04/04/12	10:21	0.20	1.45	5	289.40	-0.83	0.92	-0.52	
04/04/12	15:29	0.20	1.45	5	288.30	-1.60	0.92	-0.52	332,603
04/04/12	17:05	0.20	1.45	5	288.50	-1.62	0.92	-0.52	362,000
04/04/12	18:38	0.27	1.45	5	301.50	11.50	0.99	-0.45	389,000
04/06/12	10:40	0.27	1.45	5	296.00	6.20	0.99	-0.45	676,610
04/06/12	12:41	0.27	1.45	5	295.00	4.60	0.99	-0.45	709,970
04/07/12	15:23	0.27	1.45	5	281.50	-8.40	0.99	-0.45	
04/07/12	16:11	0.35	1.45	5	297.60	7.03	1.07	-0.37	1,198,700
04/08/12	14:57	0.35	1.45	5	289.00	0	1.07	-0.37	
04/09/12		0.35	1.45	5	286.00	-3.90	1.07	-0.37	1,980,000

4.3.5.2 Failed sample characterization

The images of the failed B5 sample are shown in Figure 53. After the initial cyclic loading process, the B5 sample was submerged into liquid nitrogen for 5 minutes. In order to cause B5 failure, significant torque was applied with a torque wrench, assuming that the sample would fail like a brittle material. The B5 sample did not fail even though the sample was subjected to strong twisting, as can be observed from the dented area and the stretched spiral groove. An addition cut was performed in the middle section of the twisted B5 sample. No clear crack penetration was observed.

Figure 53. The failed B5 specimen in X52 base steel series.

4.3.6 X52 base material sample B6

4.3.6.1 Cycle fatigue process

For the cycle fatigue process (Table 16) of sample B6, the initial maximum torque was adjusted to around 300 lbf-in 5 HZ until ~343,000 cycles. Then the load was increased to 320 lbf-in. The cyclic fatigue loading process ended before the loading-unloading test was performed.

Table 16. The monitoring process of B6 sample through a function generator

Date	Time (EST)	Mean (degree)	Amplitude (degree)	Freq	Torque (lbf-in)		Theta (degree)		Count
					Peak	Valley	Peak	Valley	
04/09/12		2.75	1.50	5	298.00	2.30	3.50	2.00	300
04/10/12	10:29	2.75	1.50	5	288.60	-8.20	3.50	2.00	260,280
04/10/12	11:04	2.75	1.50	5	288.90	-8.60	3.50	2.00	
04/10/12	15:40	2.75	1.50	5	288.00	-9.00	3.50	2.00	342,645
04/10/12	15:58	2.90	1.55	5	317.00	7.16	3.67	2.12	343,500
04/10/12	17:05	2.90	1.55	5	315.00	5.20	3.67	2.12	364,180
04/10/12	17:47	2.90	1.55	5	314.00	4.80	3.67	2.12	376,700
04/10/12	18:12	2.90	1.55	5	314.00	4.20	3.67	2.12	384,800
04/11/12	10:14	2.90	1.55	5	308.00	-0.89	3.67	2.12	672,830
04/11/12	12:06	2.90	1.55	5	307.10	-1.74	3.67	2.12	702,200
04/11/12	15:48	2.90	1.55	5	306.20	-0.86	3.67	2.12	768,500
04/11/12	18:54	2.90	1.55	5	299.10	-3.74	3.67	2.12	824,800
04/11/12	19:08	2.90	1.55	5	298.80	-3.15	3.67	2.12	825,200

4.3.6.2 Failed sample characterization

The images of the failed B6 sample were shown in Figure 54. After the initial cyclic loading process, dye penetrant (Magnaflux, Glenview, IL) was sprayed into the cracked B6 sample (Figure 55). The fatigue precrack test stopped when the dynamic torque was around lbf-in. Then the loading–unloading test was performed to characterize the mechanical behavior of the B6 sample, as described below.

Figure 54. The failed B6 specimen in X52 base steel series

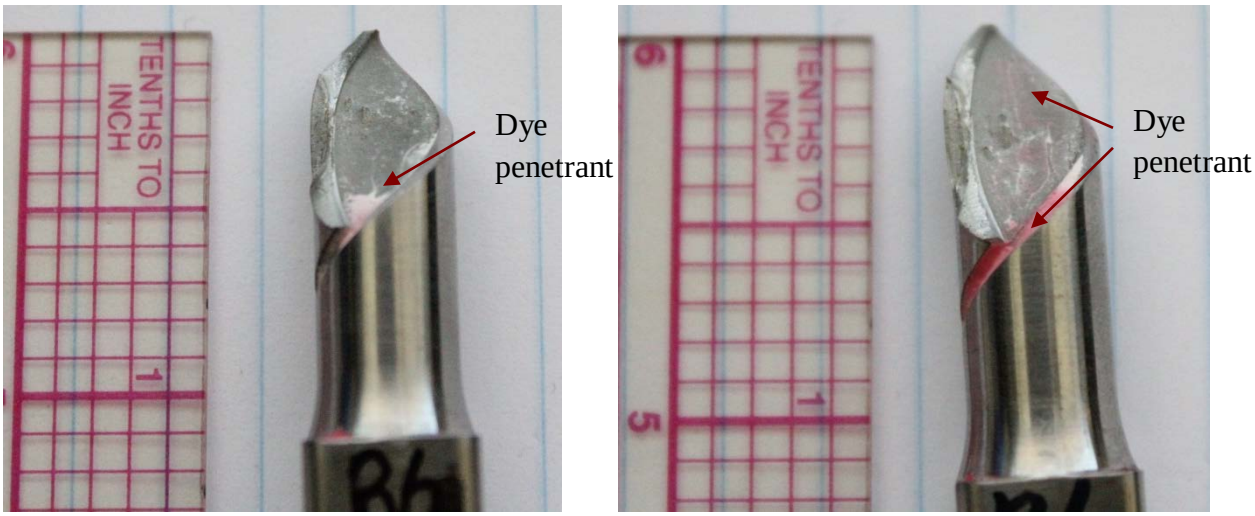

Figure 55. Tailed B6 specimen at higher resolution (a) one half of failed B6; (b) the other half of the failed B6.

4.3.6.3 Loading-unloading test

After the fatigue pre-crack process, manual controlled loading-unloading test was performed. The results are charted in Figure 56. The linear range of the loading curve was below 100 lbf-in during the first loading segment. The yielding of material occurred after that critical point. At the same time, the loading and unloading curves separated from each other. Sample B6 failed when the load reached 220 lbf-in.

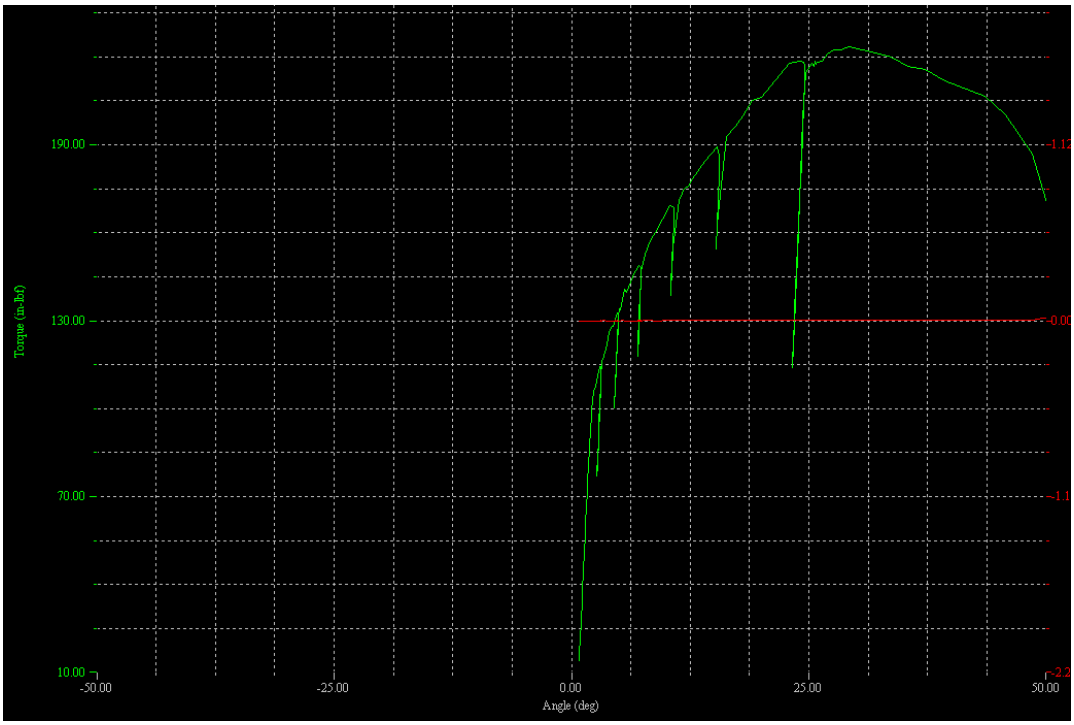

Figure 56. Loading-unloading curve of B6 sample after fatigue precrack process.

4.3.7 X52 base material sample B7

4.3.7.1 Cycle fatigue process

The initial maximum torque on sample B7 was adjusted to around 260 lbf-in 5 HZ for the cyclic fatigue process until ~260,000 cycles. Then the load increased to 320 lbf-in until ~824,000 cycles. At approximately 1.5 million cycles, the load increased to 340 lbf-in. With the degradation of the dynamic torque, the load increased to ~ 380 lbf-in. At that point, the cyclic fatigue loading process ended when the fracture torque decreased to 250 lbf-in at ~ 2.2 million cycles.

Table 17.The monitoring process of B7 sample through a function generator

Date	Time (EST)	Mean (degree)	Amplitude (degree)	Freq	Torque (lbf-in)		Theta (degree)		Count
					Peak	Valley	Peak	Valley	
04/13/12		3.90	1.20	5	252.99	18.20	4.50	3.30	260,157
04/13/12	11:50	4.25	1.60	5	320.30	8.40	5.05	3.45	262,100
04/13/12	12:40	4.25	1.60	5	315.20	3.49	5.04	3.44	276,080
04/13/12		4.25	1.60	5	314.90	2.98	5.04	3.44	276,500
04/13/12		4.25	1.60	5	315.90	3.56	5.04	3.44	304,480
04/13/12		4.25	1.60	5	312.10	1.57	5.04	3.44	304,600
04/13/12	16:02	4.25	1.60	5	315.40	3.40	5.04	3.44	330,300
04/13/12	16:56	4.25	1.60	5	314.20	4.00	5.04	3.44	343,700
04/13/12	17:53	4.10	1.10	5	237.10	21.70	4.65	3.55	357,700
04/14/12	14:25	4.40	1.30	5	312.00	56.00	5.05	3.75	742,792
04/14/12	19:26	4.10	1.20	5	236.00	7.90	4.67	3.49	824,230
04/15/12	15:06	4.40	1.50	5	332.00	38.00	5.15	3.65	1,181,471
04/15/12	19:00	4.20	1.30	5	271.00	16.80	4.84	3.55	1,256,334
04/15/12	19:22	4.30	1.40	5	302.00	28.00	5.00	3.60	
04/16/12	9:10	4.30	1.40	5	304.00	28.00	4.99	3.59	1,508,537
04/16/12	9:22	4.40	1.50	5	334.00	40.00	5.15	3.65	1,509,357
04/16/12	9:48	4.40	1.50	5	334.00	40.59	5.15	3.65	1,514,584
04/16/12	10:51	4.40	1.50	5	334.00	40.00	5.15	3.65	1,533,390
04/16/12	11:01	4.40	1.50	5	334.00	40.00	5.15	3.65	1,533,600
04/16/12	12:34	4.40	1.50	5	328.00	34.00	5.15	3.65	1,561,110
04/16/12	14:14	4.40	1.50	5	334.00	40.00	5.15	3.65	1,589,400
04/16/12	14:39	4.32	1.70	5	338.00	8.00	5.17	3.47	1,592,490
04/16/12	16:28	4.32	1.70	5	339.00	7.50	5.17	3.47	1,624,689
04/17/12		4.30	1.70	5	316.60	23.60	5.05	3.55	1,969,000
04/17/12	12:07	4.45	1.75	5	365.80	24.10	5.32	3.57	1,972,000
04/17/12	13:30	4.45	1.75	5	360.10	20.73	5.32	3.57	1,996,300
04/17/12	14:56	4.45	1.75	5	359.40	19.80	5.32	3.57	
04/17/12		4.45	1.75	5	359.00	19.00	5.32	3.57	2,032,400
04/17/12		4.45	1.75	5	380.50	29.00	5.32	3.57	2,039,410
04/17/12		4.55	1.80	5	374.50	26.20	5.45	3.65	2,052,300
04/17/12		4.40	1.40	5	301.00	32.00	5.09	3.69	2,073,400
04/17/12		4.30	1.30	2	270.00	21.00	4.95	3.65	2,075,988
04/18/12	14:20	4.30	1.30	2	252.00	17.60	4.95	3.65	2,218,680
04/18/12	15:30	4.30	1.30	2	250.00	19.60	4.95	3.65	2,226,570

4.3.7.2 Failed sample characterization

The images of the failed B7 sample, which split into two halves during the fatigue process, are shown in Figure 57. In Figure 58a, the fatigue crack front extends to the edge of the SNTT

cylinder. There are similar defect areas in this failed sample compared to those observed in samples B1 and B3. An additional cut was made in one of the split halves to examine the crack penetration status on the edge of the spiral notch. No clear crack penetration was observed in the cross-section.

Figure 57. The failed B7 specimen in X52 base steel series

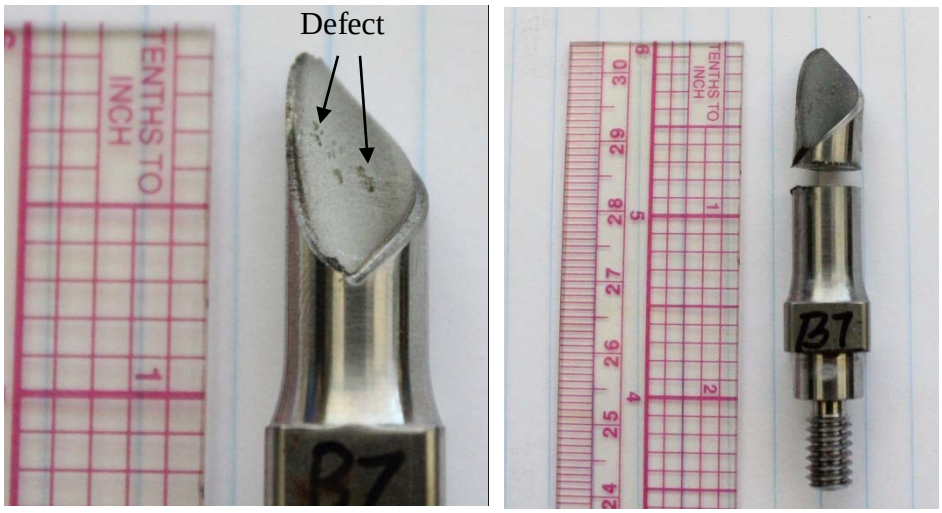

(a) (b)

Figure 58. The failed B7 specimen with higher resolution (a) one half of failed sample; (b) the other half of the failed sample.

4.3.8 X52 base material sample B8

4.3.8.1 Cycle fatigue process

The cycle fatigue process (Table 18) of sample B8 was also performed through the angle control mode by the same function generator built in the MTS system. The initial maximum torque was adjusted to around 280 lbf-in 5 HZ cyclic fatigue process until ~32,000 cycles. Then the load increased to 320 lbf-in for the same angle control until ~309,000 cycles. Around 377,000 cycles, the load increased to 380 lbf-in for the same angle control to facilitate the crack growth. Then, the cyclic fatigue loading process ended when the fracture torque decreased to 18.9 lbf-in around 539,000 cycles before the loading-unloading test was performed to the B8 sample.

Table 18. The monitoring process of B8 sample through a function generator

Date	Time (EST)	Mean (degree)	Amplitude (degree)	Freq	Torque (lbf-in)		Theta (degree)		Count
					Peak	Valley	Peak	Valley	
04/19/12	15:29	4.63	1.40	5	271.00	5.78	5.31	3.93	800
04/19/12	16:00	4.63	1.40	5	271.00	5.20	5.31	3.93	9,670
04/19/12	17:03	4.63	1.40	5	269.00	3.60	5.31	3.93	29,180
04/19/12	17:33	4.88	1.66	5	318.00	1.90	5.69	4.07	32,300
04/19/12	19:08	4.88	1.66	5	246.00	-2.10	5.71	4.05	55,073
04/19/12	19:32	4.88	1.66	5	245.00	-1.90	5.71	4.05	62,450
04/19/12	19:50	4.88	1.66	5	244.00	-1.53	5.71	4.05	64,650
04/20/12	9:13	4.88	1.66	5	227.00	-1.30	5.71	4.05	304,200
04/20/12		5.50	1.66	5	340.00	13.00	6.33	4.67	309,400
04/20/12		5.50	1.66	5	330.00	6.80	6.33	4.67	328,357
04/20/12		5.50	1.66	5	328.00	5.10	6.33	4.67	354,890
04/20/12		5.50	1.66	5	327.00	6.50	6.32	4.66	370,567
04/20/12		5.50	1.66	5	342.00	14.00	6.32	4.66	370,652
04/20/12		5.50	1.66	5	339.00	14.00	6.32	4.66	372,377
04/20/12		5.60	1.66	5	353.00	28.00	6.42	4.76	377,309
04/20/12		5.60	1.66	5	349.00	23.00	6.43	4.77	389,183
04/20/12	16:20	5.60	1.66	5	346.00	23.00	6.43	4.77	
04/20/12		5.60	1.68	5	348.00	20.00	6.44	4.76	
04/21/12		5.60	1.68	2	18.90	-3.96	6.44	4.76	539,546

4.3.8.2 Failed sample characterization

Figure 59 contains the images of the failed B8 sample. The fatigue pre-crack process stopped when the dynamic torque was around lbf-in. Then the loading–unloading test was performed to characterize the mechanical behavior of the B6 sample. In Figure 60, there were no defect areas similar to those observed for sample B1 and B3. Due to an accidental switch between force mode to displacement mode of the MTS system, one thread on the SNTT sample was torn apart in the end section area. The thread diameter was increased to 5/16 inch in the updated design to strengthen the sample in the new batch.

Figure 59. The failed B8 specimen in X52 base steel series.

Figure 60. The failed B8 specimen with higher resolution (a) one half of failed sample; (b) the other half of the failed sample.

4.3.8.3 Loading-unloading test

After the fatigue precrack process, manual controlled loading-unloading test was performed. The results were shown in Figure 61. The linear range of the loading curve was below 25 lbf-in during the first loading segment. The yielding of material occurred after that critical point. In the meantime, the loading and unloading curves separated from each other. The loading-unloading test ended when the load reached approximately 120 lbf-in.

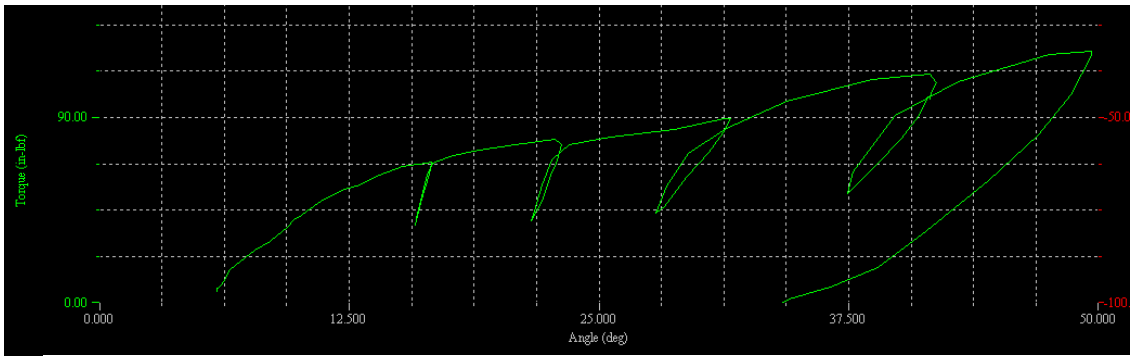

Figure 61. The loading-unloading curve of B8 sample after fatigue precrack process.

4.3.9 X52 base material sample B9

4.3.9.1 Cycle fatigue process

From sample B9, a program was established using the Teststar software in MTS system to control the crack growth of SNTT samples in the cycle fatigue process. Load control was used to drive the cracks; while critical angle was set up to trigger the termination of the program. The primary monitoring parameters were listed in Table 19.

Table 19. The monitoring process of B9 sample through a controlled program

Date	Sample	Run	Frequency	Torque (lbf-in)		Cycle Interval
				Peak	Valley	
04/21/12	B9	01	2	380	10	5000

In order to capture the crack growth process in SNTT sample, a proper parameter needs to be selected to reflect compliance evolution. In Figure 62, the net section of SNTT sample is the part where torque loading was applied during the cyclic fatigue process.

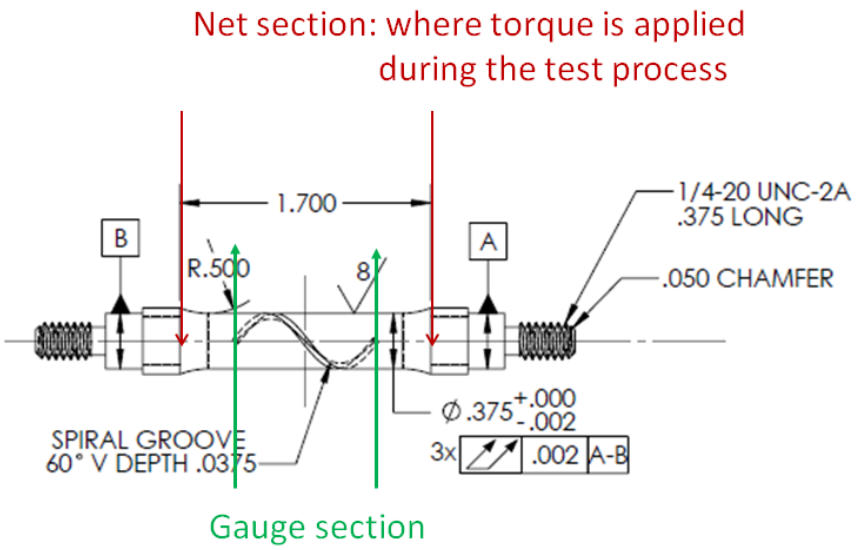

Figure 62. The net section of SNTT specimen during the loading process.

Based on the RVDT recording system, the corresponding load and end rotation angles will be recorded as time series for the net section. By subtracting the rotation angles on both ends, the end rotation angles of the gauge section can be obtained. A slope index is defined as

$$Slope_{gauge} = \frac{Torque}{Angle_{gauge}} \qquad \text{Equation 1}$$

The gauge slope was calculated for each compliance measurement until the program ended. In

b

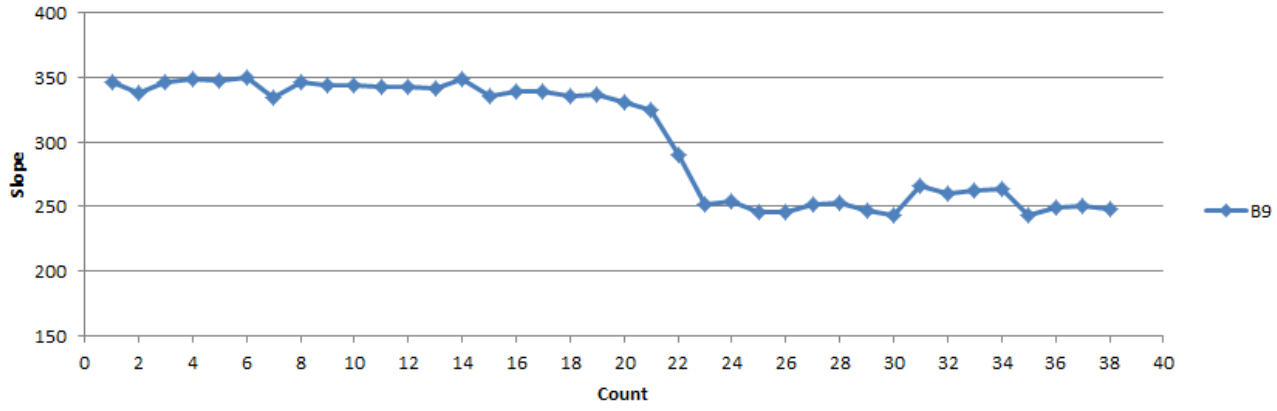

Figure 63. The monitoring curve of crack growth process in SNTT sample B9.
In Figure 63, it shows that the slope decrease gradually before the count 20. Then the crack penetrated quickly between count 20 and 22. The program ended soon after this jump since the end rotation angle reached the critical angle limit. After count 24, the slope measurement stayed in the same level. Based on the data in Figure 32, the penetration of final crack penetrating ratio in sample B9 is ~0.45.

4.3.9.2 Failed sample characterization

When the program ended, the sample was cut into parts using a diamond saw Labcut 1010 (Extec, Enfield, CT) to check the actual crack depth. Various locations along the specimen axis were selected for cross sections check. When the cross section is in the middle section of the SNTT specimen, cracks could be observed clearly. However, no clear cracks could be observed to when the cross sections located close to the square ends of the SNTT sample. The assembled length of B9 parts is shorted than the original sample since one segment is with Ohio State University for characterization.

Figure 64. The failed B9 specimen in X52 base steel series.

In the middle of the B9 sample, the crack profiles in the cross section were characterized in Figure 65a and Figure 65b using the optical microscope (SZH10, Olympus, Japan). By measuring the crack penetration depth on both sides of the cut specimen, the ration of crack depth to diameter are 0.41 and 0.40 on each side, respectively.

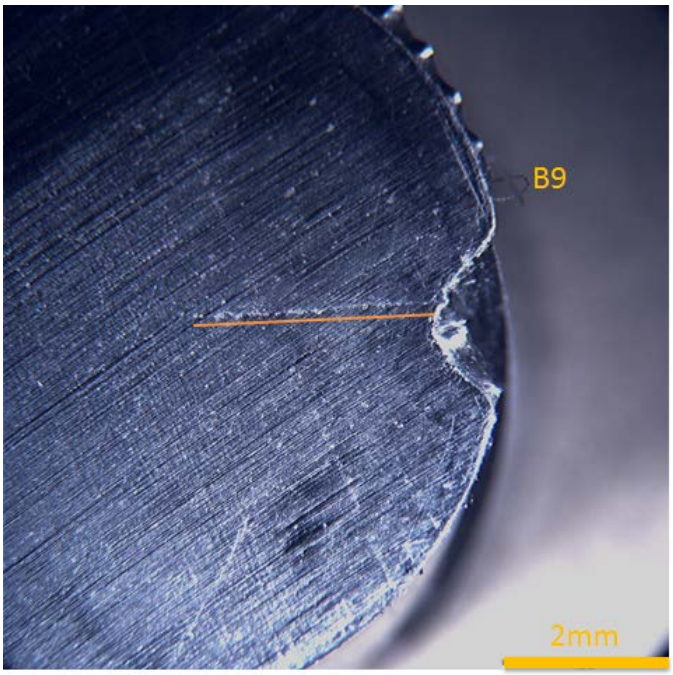

(a)

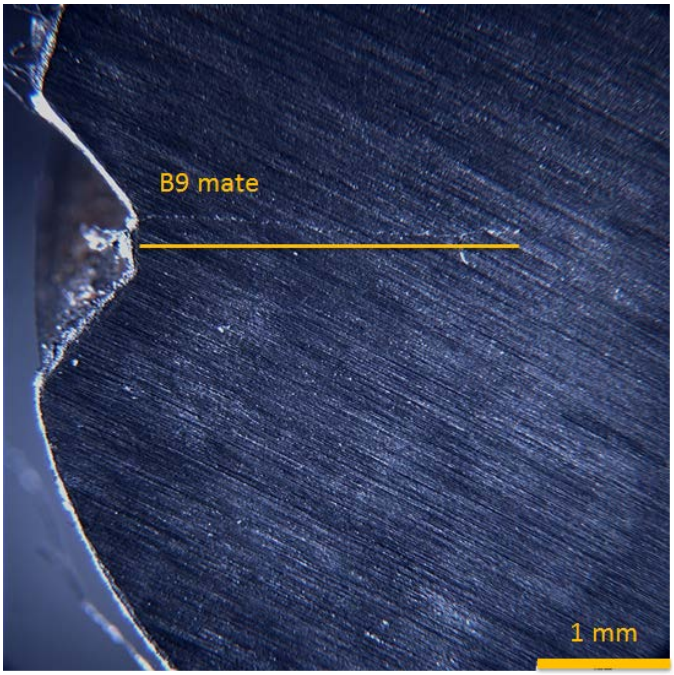

(b)

Figure 65. The crack depth in the middle section of sample B9 after fatigue precrack process: (a) cut; (b) cut mate.

4.3.10 X52 base material sample B10

4.3.10.1 Cycle fatigue process

In sample B10, the same program was applied in MTS system to drive the crack into SNTT samples with load control mode. The primary monitoring parameters were listed in Table 20.

Table 20.The monitoring process of B10 sample through a controlled program

Date	Sample	Run	Frequency	Torque (lbf-in)		Cycle Interval
				Peak	Valley	
04/25/12	B10	01	2	380	10	5000

The gauge slope evolution process in sample B10 was shown in Figure 66. It shows that the slope stayed almost in the same level before the count 11. Then the crack penetrated quickly between count 11 and 18. The program ended soon after this jump since the end rotation angle reached the critical angle limit. After count18, the slope measurement stayed in the same level. Based on the data in Figure 32, the penetration of final crack penetrating ratio in sample B10 is ~0.35.

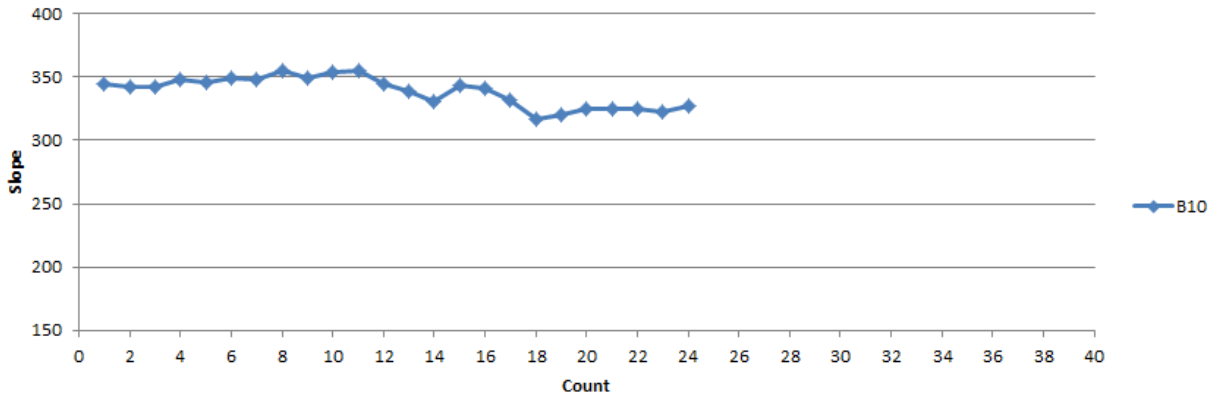

Figure 66. The monitoring curve of crack growth process in SNTT sample B10.

4.3.10.2 Failed sample characterization

When the program ended, the sample was cut into parts using a diamond saw Labcut 1010 (Extec, Enfield, CT) to check the actual crack depth. The middle section was cut perpendicular to the cylindrical axis; while another skew cut was performed above the middle section cut (Figure 67). In the middle-section cut (Figure 68), the measured ratios of crack depth to diameter were 0.28 and 0.30 on both sides. In the skew-cut section (Figure 69), the measured ratios of crack depth to diameter were 0.18 and 0.16 on both sides. Due to an accidental switch between force mode to displacement mode of the MTS system, one thread on the SNTT sample was torn apart in the end section area.

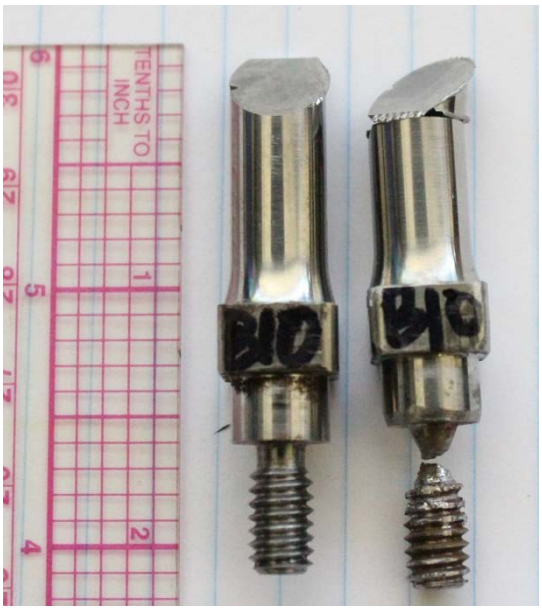

Figure 67. The failed B10 specimen in X52 base steel series.

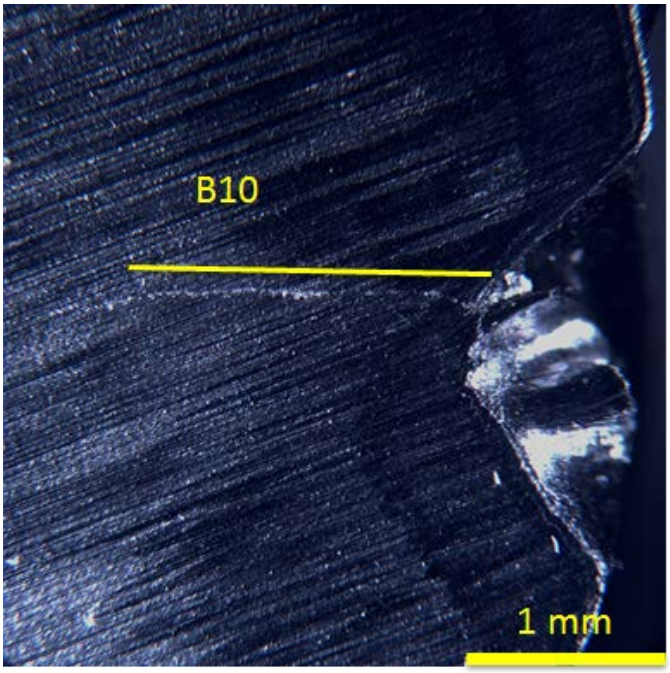

(a)

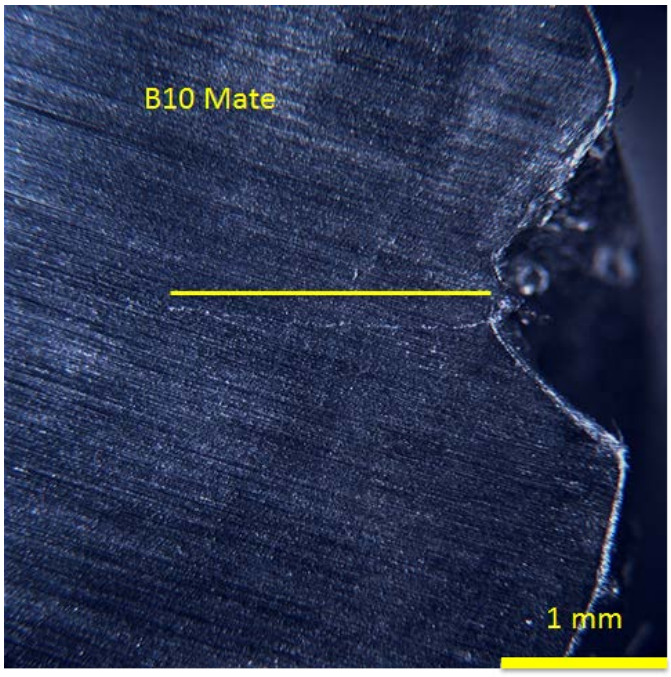

(b)

Figure 68. The crack depth in the middle section of sample B10 after fatigue precrack process: (a) cut; (b) cut mate.

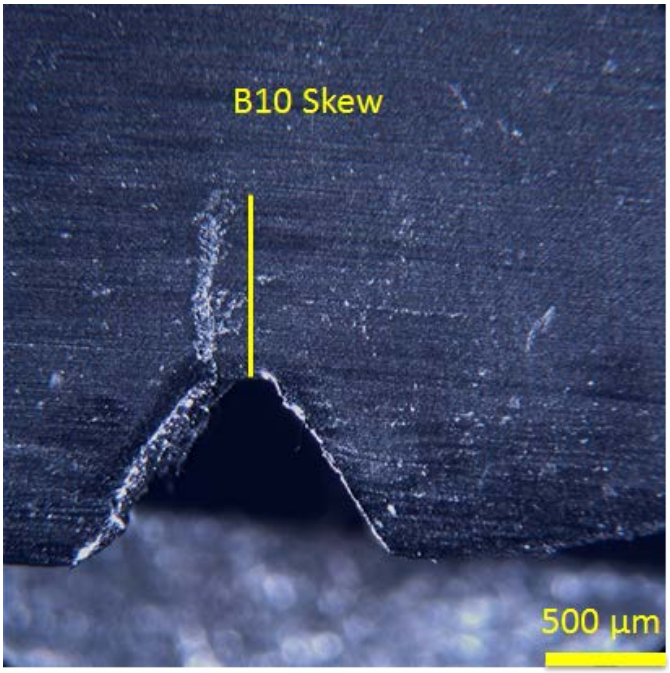

(a)

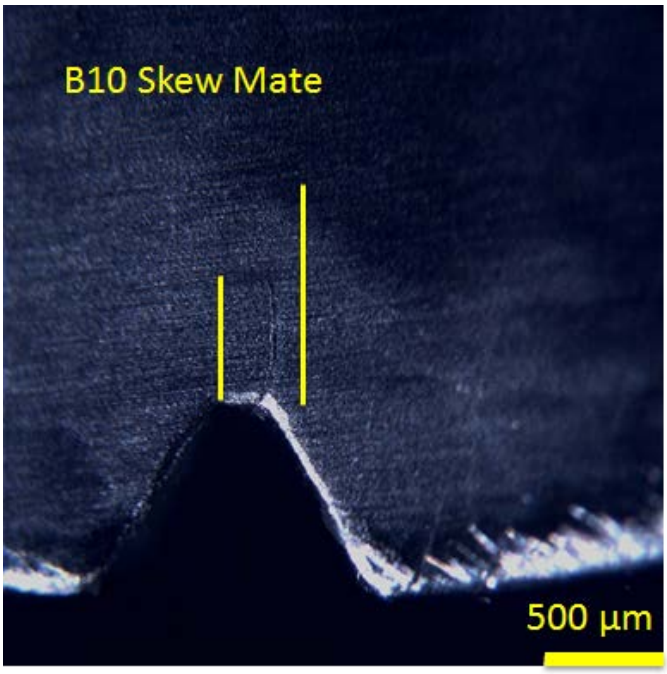

(b)

Figure 69. The crack depth in the skew-cut section of sample B10 after fatigue precrack process: (a) skew cut; (b) skew cut mate.

4.3.11 X52 base material sample B11

4.3.11.1 Cycle fatigue process

In sample B11, the same program was applied to drive the crack into SNTT samples with load control mode. The primary monitoring parameters were listed in Table 21.

Table 21. The monitoring process of B11 sample through a controlled program

Date	Sample	Run	Frequency	Torque (lbf-in)		Cycle Interval
				Peak	Valley	
04/27/12	B11	01	5	380	10	5000
04/28/12	B11	02	5	380	10	5000

The gauge slope evolution process in sample B11 was shown in Figure 70. It shows that the slope stayed almost in the same level before the count 13. Then the crack penetrated quickly between count 13 and 20. The program ended soon after this jump since the end rotation angle reached the critical angle limit. After count 20, the slope measurement stayed in the same level. Based on the data in Figure 32, the penetration of final crack penetrating ratio in sample B11 is ~0.29.

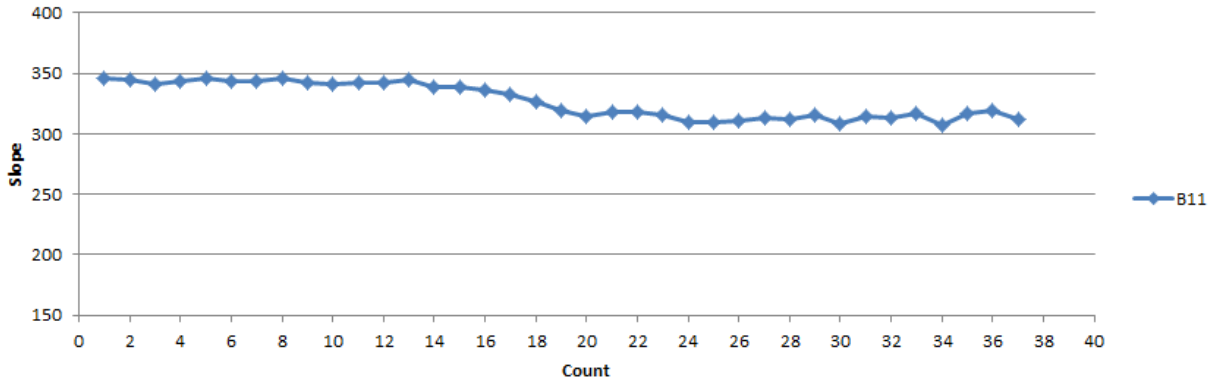

Figure 70. The monitoring curve of crack growth process in SNTT sample B11.

4.3.11.2 Failed sample characterization

When the program ended, the sample was cut into parts using a diamond saw Labcut 1010 (Extec, Enfield, CT) to check the actual crack depth. The middle section was cut in an angle of 45 degree with respect the cylindrical axis; while another cut was performed perpendicular to the cylinder axis above the previous cut (Figure 71). In the middle-section skew cut (Figure 72), the measured ratios of crack depth to diameter were 0.31 and 0.30 on both sides. In the cut perpendicular to the cylindrical axis, no clear cracks were observed in the cross section.

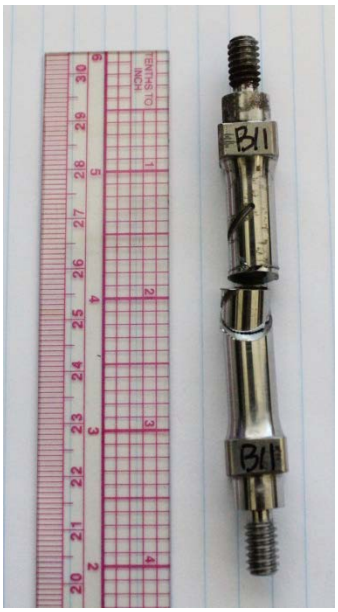

Figure 71.The failed B11 specimen in X52 base steel series.

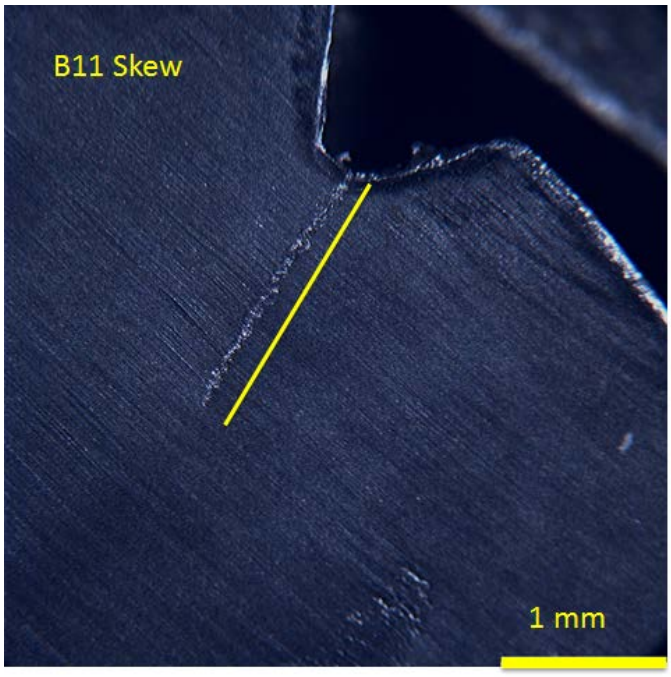

(a)

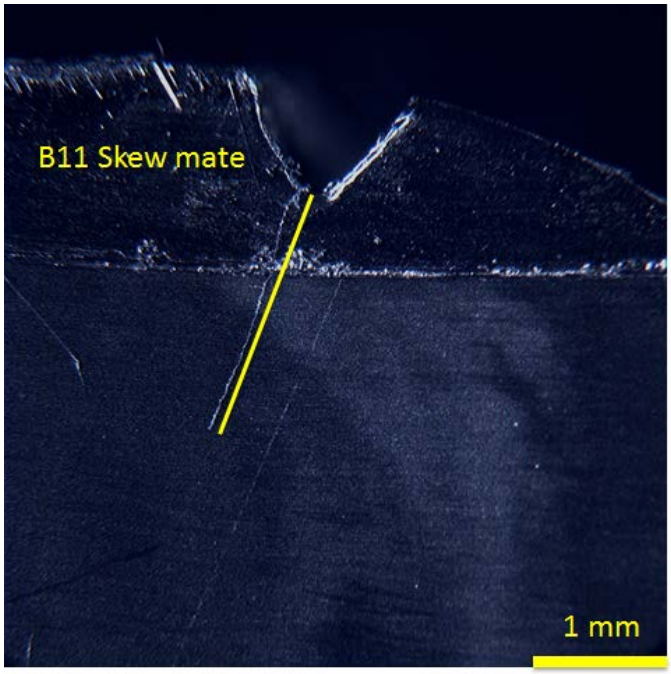

(b)

Figure 72. The crack depth in the middle section with a skew-cut of sample B11 after fatigue precrack process: (a) skew cut; (b) skew cut mate.

4.3.12 X52 base material sample B12

4.3.12.1 Cycle fatigue process

In the sample B12, the same program was applied to drive the crack into SNTT samples with load control mode. The primary monitoring parameters were listed in Table 22.

Table 22. The monitoring process of B12 sample through a controlled program

Date	Sample	Run	Frequency	Torque (lbf-in)		Cycle Interval
				Peak	Valley	
04/29/12	B12	01	5	380	10	5000

The gauge slope evolution process in sample B12 was shown in Figure 73. It shows that the slope stayed almost in the same level before the count 10. Then the crack penetrated quickly between count 10 and 15. The program ended soon after this jump since the end rotation angle reached the critical angle limit. After count 15, the slope measurement stayed in the same level. Based on the data in Figure 32, the penetration of final crack penetrating ratio in sample B12 is ~0.29.

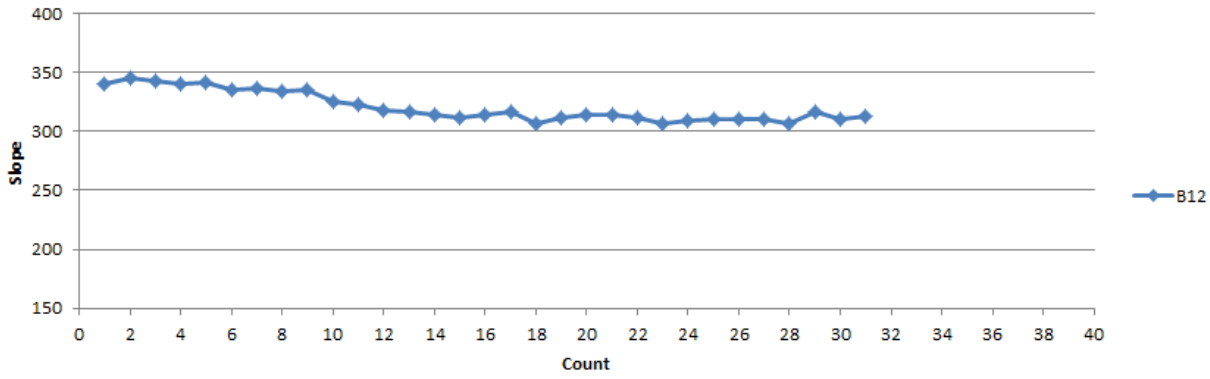

Figure 73. The monitoring curve of crack growth process in SNTT sample B12.

4.3.12.2 Failed sample characterization

When the program ended, the sample was cut into parts using a diamond saw Labcut 1010 (Extec, Enfield, CT) to check the actual crack depth. A cut was performed perpendicular to the cylindrical axis in middle section; while another cut was performed at angle of 45 degree to the cylinder axis above the previous cut (Figure 74). In the middle-section cut (Figure 75), the measured ratios of crack depth to diameter were 0.14 and 0.14 on both sides. In the skew-cut (Figure 76), the measured ratios of crack depth to diameter were 0.13 and 0.13 on both sides.

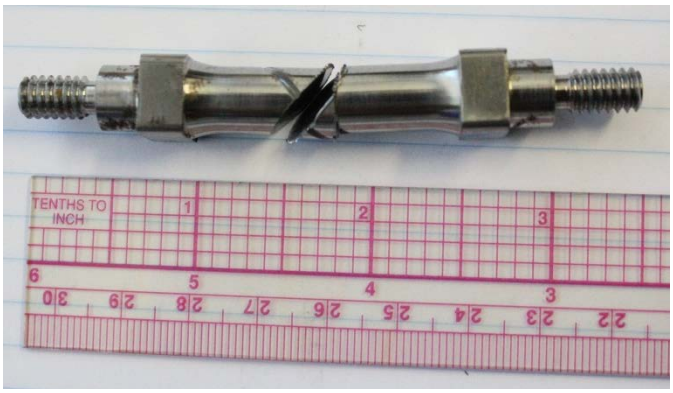

Figure 74. The failed B12 specimen in X52 base steel series.

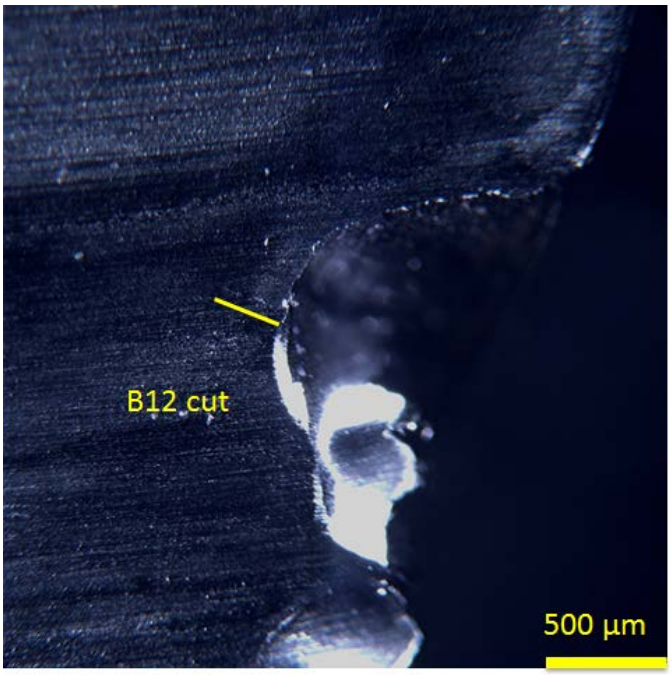

(a)

(b)

Figure 75. The crack depth with a cut perpendicular to the cylindrical axis in the middle section of sample B12 after fatigue precrack process: (a) skew cut; (b) skew cut mate.

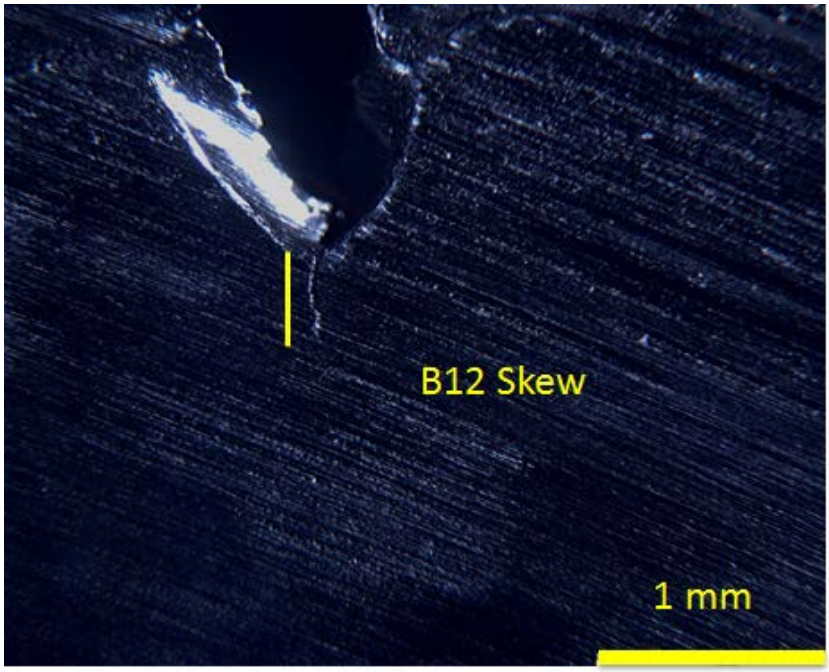

(a)

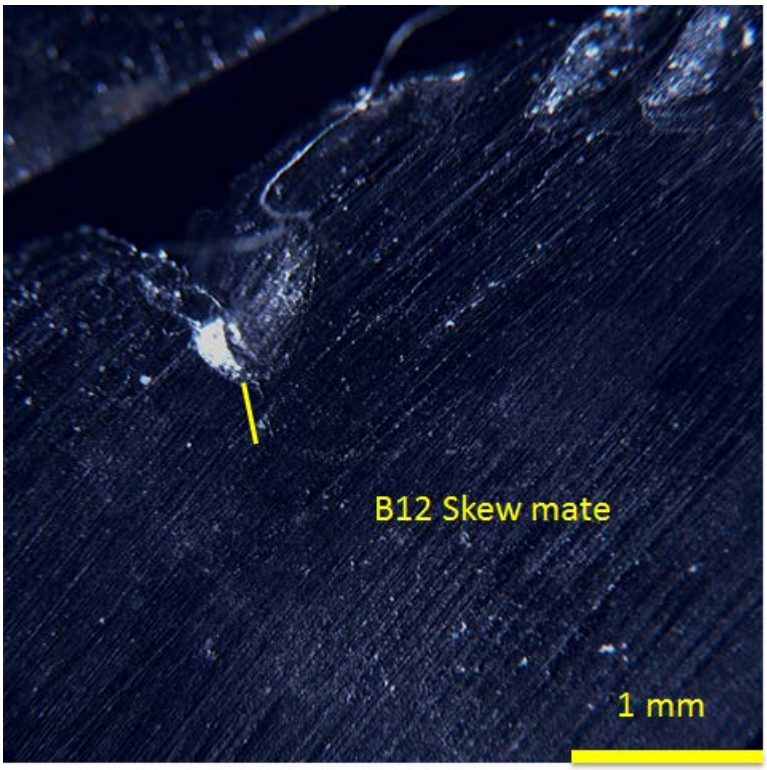

(b)

Figure 76. The crack depth with a skew-cut of sample B11 after fatigue precrack process: (a) skew cut; (b) skew cut mate.

4.4 In air SNTT testing of new batch X52 steel base materials

4.4.1 X52 SNTT sample design in the new batch

Most of the designs in Figure 35 remained the same except the diameter of the threads increased from ¼ in to 5/16 in. The new design is shown in Figure 77.

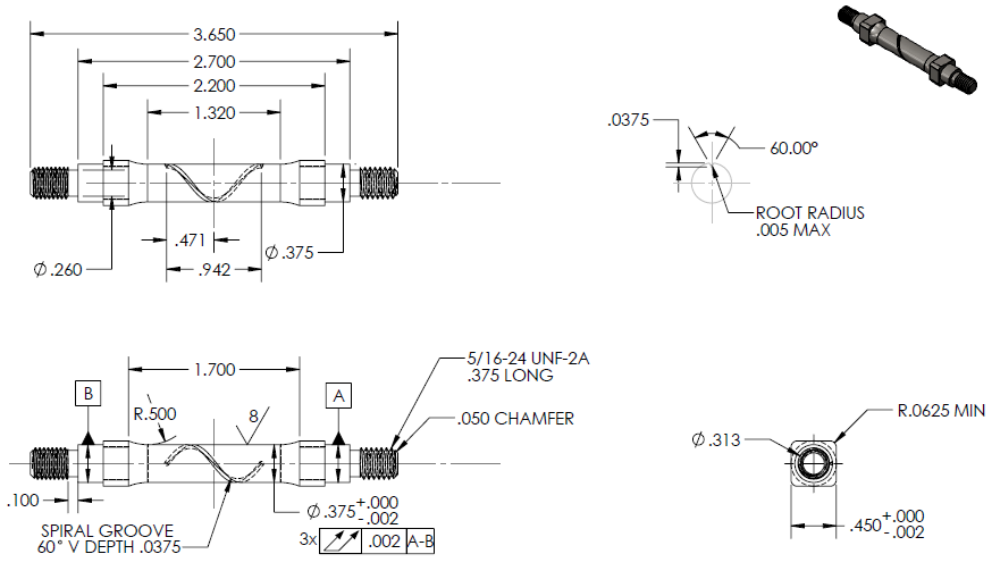

Figure 77. The new design of X52 steel SNTT specimen.

4.4.2 X52 base material sample NB01 in new batch

4.4.2.1 Cycle fatigue process

In the sample NB01, the same program was applied to drive the crack into SNTT samples with load control mode. The primary monitoring parameters were listed in Table 23.

Table 23. The monitoring process of NB01 sample through a controlled program

Date	Sample	Run	Frequency	Torque (lbf-in)		Cycle Interval
				Peak	Valley	
07/24/12	NB01	01	5	380	10	5000
07/25/12	NB01	02	5	300	10	5000

The gauge slope evolution process in sample NB01 was shown in Figure 78. It shows that the slope stayed almost in the same level before the count 11. Then the crack penetrated effectively between count 11 and 29. The program ended soon after this jump since the end rotation angle reached the critical angle limit. After count 29, the slope measurement stayed in the same level. Based on the data in Figure 32, the estimations of corresponding crack penetration ratios were also included, of which the final penetration in sample NB01 was ~0.40.

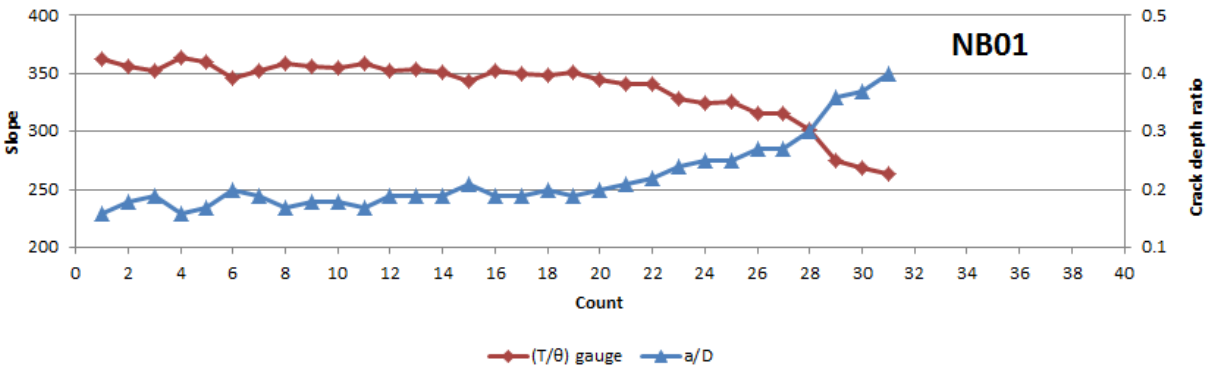

Figure 78. The monitoring curve of crack growth process in SNTT sample NB01.

4.4.2.2 Precracked sample characterization

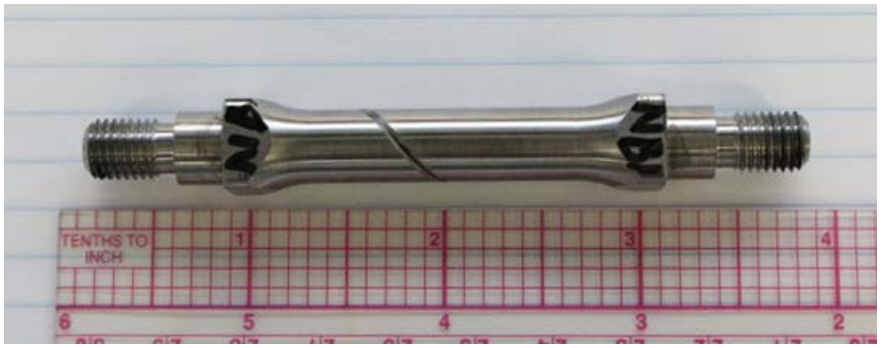

Figure 79. The precracked SNTT X52 steel sample NB01.

4.4.3 X52 base material sample NB02 in new batch

4.4.3.1 Cycle fatigue process

In the sample NB02, the same program was applied to drive the crack into SNTT samples with load control mode. The primary monitoring parameters were listed in Table 24.

Table 24. The monitoring process of NB02 sample through a controlled program

Date	Sample	Run	Frequency	Torque (lbf-in)		Cycle Interval
				Peak	Valley	
07/26/12	NB02	01	5	380	10	5000
07/27/12	NB02	02	5	300	10	5000

The gauge slope evolution process in sample NB02 was shown in Figure 80. It shows that the slope stayed almost in the same level before the count 6. Then the crack penetrated effectively between count 6 and 12. The program ended soon after this jump since the end rotation angle reached the critical angle limit. After count 12, the slope measurement stayed in the same level. Based on the data in Figure 32, the estimations of corresponding crack penetration ratios were also included, of which the final penetration in sample NB02 was ~0.45.

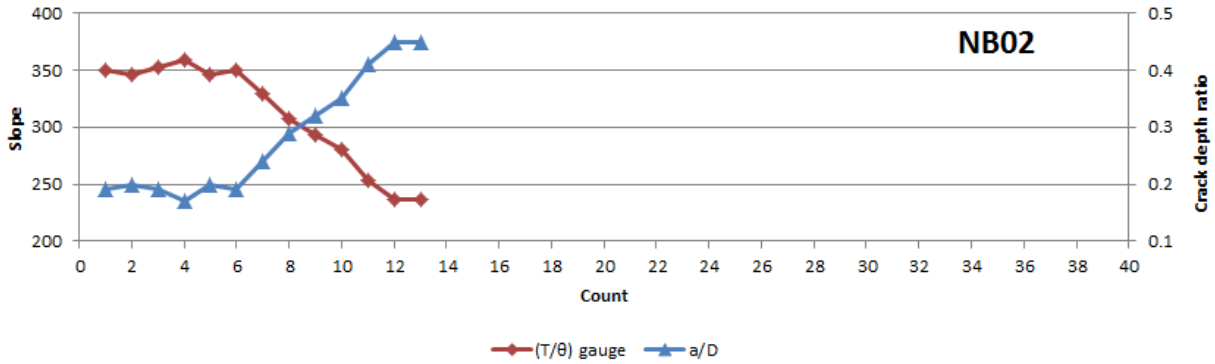

Figure 80. The monitoring curve of crack growth process in SNTT sample NB02.

4.4.3.2 Precracked sample characterization

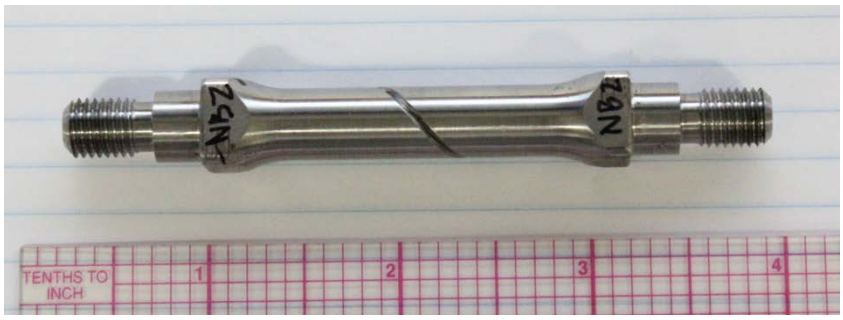

Figure 81. The precracked SNTT X52 steel sample NB02.

4.4.4 X52 base material sample NB03 in new batch

4.4.4.1 Cycle fatigue process

In the sample NB03, the same program was applied to drive the crack into SNTT samples with load control mode. The primary monitoring parameters were listed in Table 25.

Table 25. The monitoring process of NB03 sample through a controlled program

Date	Sample	Run	Frequency	Torque (lbf-in)		Cycle Interval
				Peak	Valley	

07/27/12	NB03	01	5	380	10	5000
07/27/12	NB03	02	5	300	10	5000

The gauge slope evolution process in sample NB03 was shown in Figure 80. It shows that the slope decrease gradually until the count 6. Then the crack penetrated effectively between count 6 and 14. Based on the data in Figure 32, the estimations of corresponding crack penetration ratios were also included, of which the final penetration in sample NB03 was ~0.44.

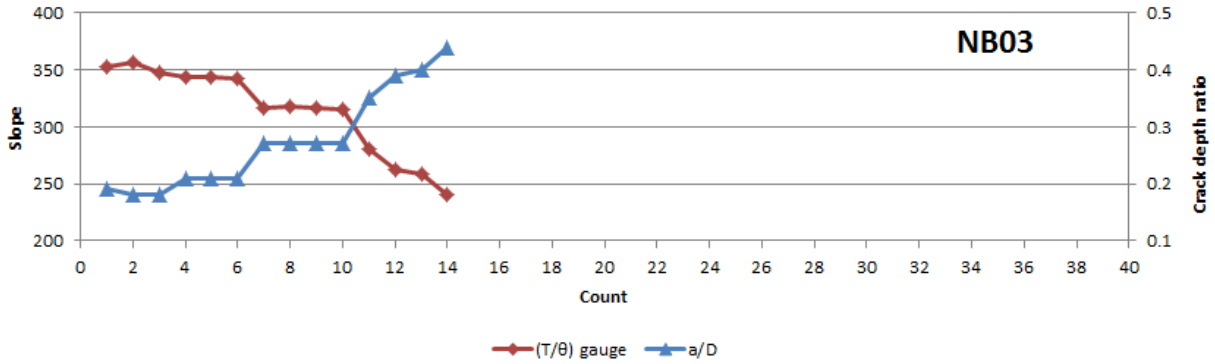

Figure 82. The monitoring curve of crack growth process in SNTT sample NB03.

4.4.4.2 Precracked sample characterization

The thread was torn apart when the displacement mode was switched to force mode suddenly during the test.

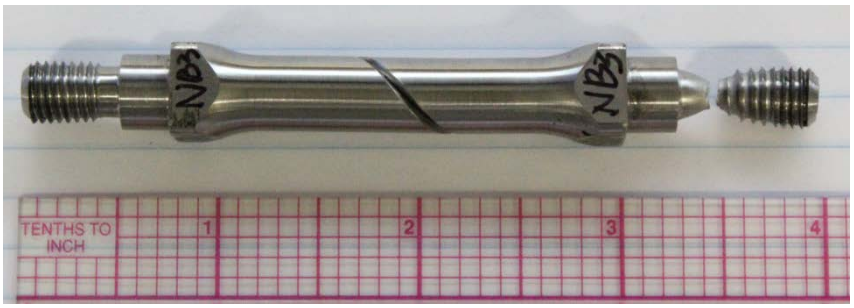

Figure 83. The precracked SNTT X52 steel sample NB03.

4.4.5 X52 base material sample NB04 in new batch

4.4.5.1 Cycle fatigue process

In the sample NB04, the same program was applied to drive the crack into SNTT samples with load control mode. The primary monitoring parameters were listed in Table 26.

Table 26. The monitoring process of NB04 sample through a controlled program

Date	Sample	Run	Frequency	Torque (lbf-in)		Cycle Interval
				Peak	Valley	
07/27/12	NB04	01	5	380	10	5000
07/28/12	NB04	02	5	300	10	5000

The gauge slope evolution process in sample NB04 was shown in Figure 84. It shows that the slope stayed in the same level until the count 6. Then the crack penetrated effectively between count 6 and 20. Based on the data in Figure 32, the estimations of corresponding crack penetration ratios were also included, of which the final penetration in sample NB04 was ~0.40.

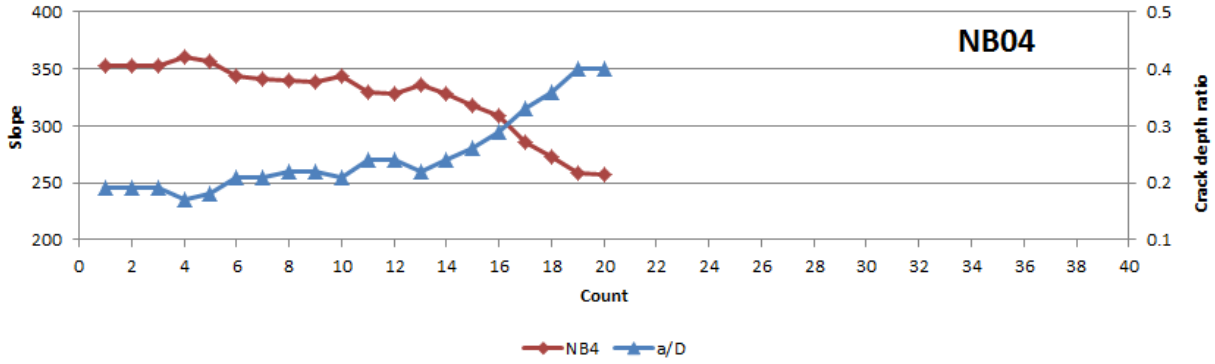

Figure 84.The monitoring curve of crack growth process in SNTT sample NB04.

4.4.5.2 Precracked sample characterization

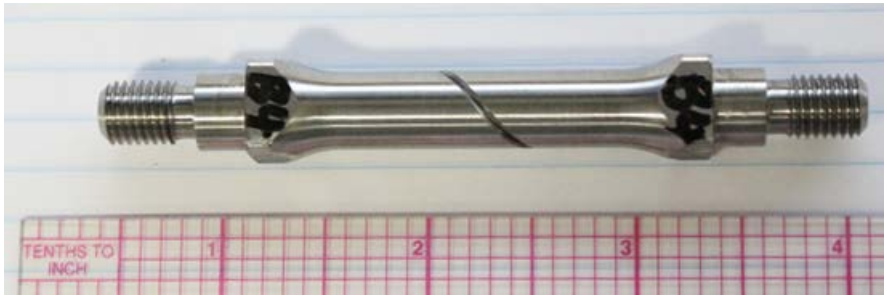

Figure 85. The precracked SNTT X52 steel sample NB04.

4.4.6 X52 base material sample NB05 in new batch

4.4.6.1 Cycle fatigue process

In the sample NB05, the same program was applied to drive the crack into SNTT samples with load control mode. The primary monitoring parameters were listed in Table 27.

Table 27. The monitoring process of NB05 sample through a controlled program

Date	Sample	Run	Frequency	Torque (lbf-in)		Cycle Interval
				Peak	Valley	
07/29/12	NB05	01	5	380	10	5000
07/30/12	NB05	02	5	300	10	5000

The gauge slope evolution process in sample NB05 was shown in Figure 86. It shows that the slope stayed in the same level until the count 7. Then the crack penetrated gradually between count 6 and 14. Based on the data in Figure 32, the estimations of corresponding crack penetration ratios were also included, of which the final penetration in sample NB05 was ~0.44.

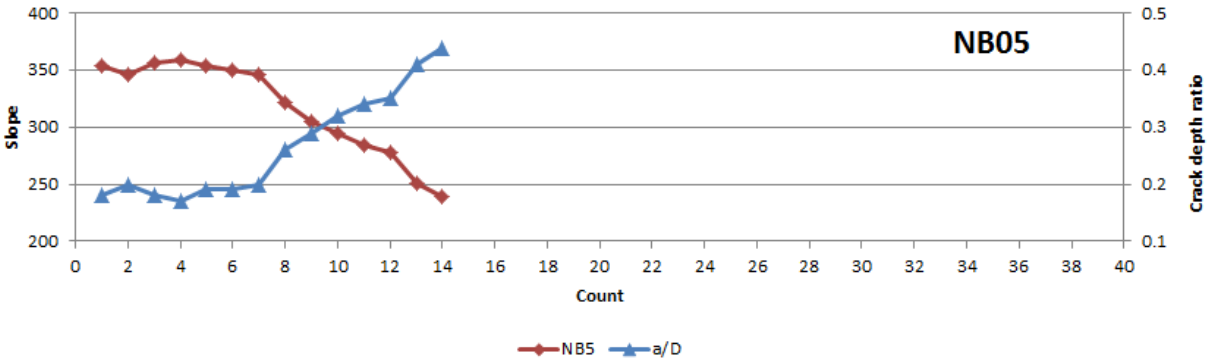

Figure 86.The monitoring curve of crack growth process in SNTT sample NB05.

4.4.6.2 Precracked sample characterization

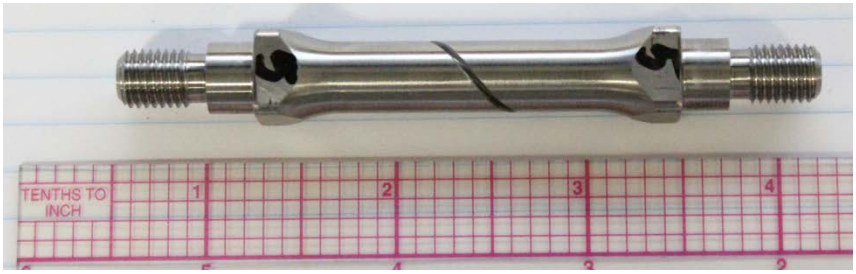

Figure 87. The precracked SNTT X52 steel sample NB05.

4.4.7 X52 base material sample NB06 in new batch

4.4.7.1 Cycle fatigue process

In the sample NB06, the same program was applied to drive the crack into SNTT samples with load control mode. The primary monitoring parameters were listed in Table 28.

Table 28. The monitoring process of NB06 sample through a controlled program

Date	Sample	Run	Frequency	Torque (lbf-in)		Cycle Interval
				Peak	Valley	
07/30/12	NB06	01	5	380	10	5000
08/01/12	NB06	02	5	300	10	5000

The gauge slope evolution process in sample NB06 was shown in Figure 88. It shows that the slope penetrated gradually since count 2. Based on the data in Figure 32, the estimations of corresponding crack penetration ratios were also included, of which the final penetration in sample NB06 was ~0.45.

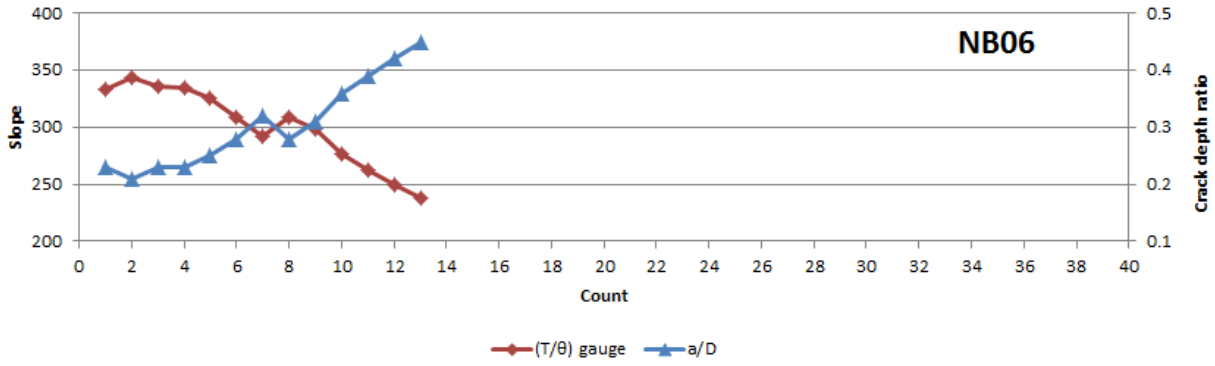

Figure 88.The monitoring curve of crack growth process in SNTT sample NB06.

4.4.7.2 Precracked sample characterization

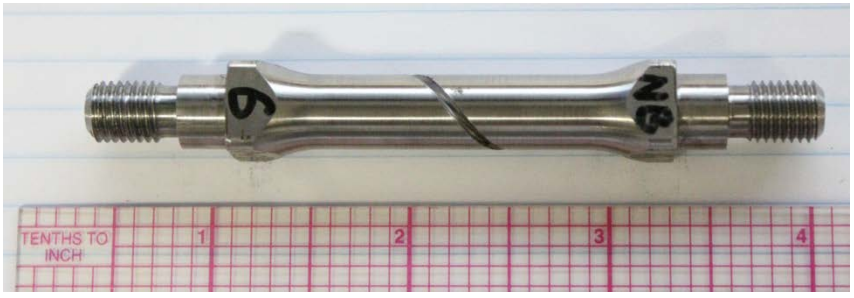

Figure 89. The precracked SNTT X52 steel sample NB06.

4.4.8 X52 base material sample NB07 in new batch

4.4.8.1 Cycle fatigue process

In the sample NB07, the same program was applied to drive the crack into SNTT samples with load control mode. The primary monitoring parameters were listed in Table 29.

Table 29. The monitoring process of NB07 sample through a controlled program

Date	Sample	Run	Frequency	Torque (lbf-in)		Cycle Interval
				Peak	Valley	
07/30/12	NB07	01	5	380	10	5000
08/01/12	NB07	02	5	300	10	5000

The gauge slope evolution process in sample NB06 was shown in Figure 88. It shows that the slope penetrated gradually since count 3. Based on the data in Figure 32, the estimations of corresponding crack penetration ratios were also included, of which the final penetration in sample NB07 was ~0.41.

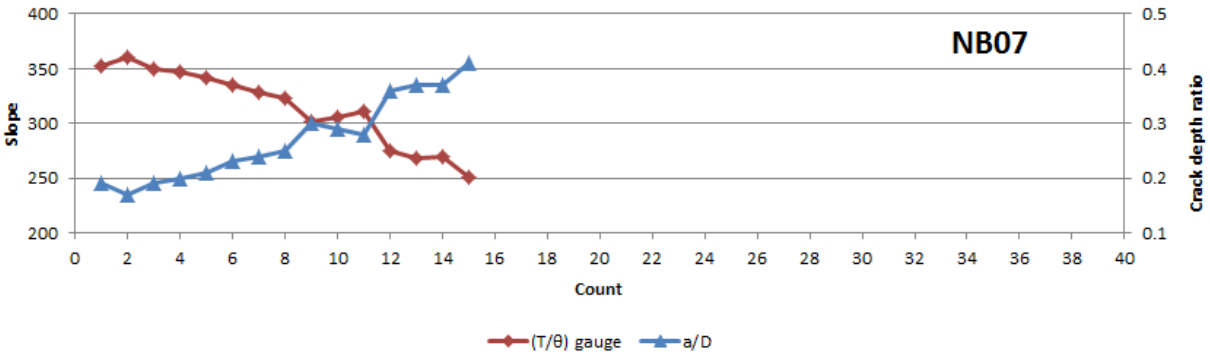

Figure 90.The monitoring curve of crack growth process in SNTT sample NB07.

4.4.8.2 Precracked sample characterization

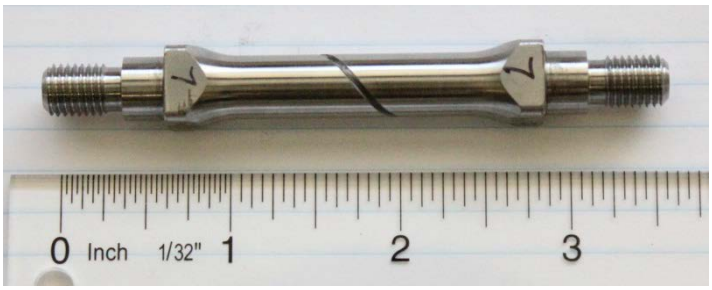

Figure 91. The precracked SNTT X52 steel sample NB07.

4.4.9 X52 base material sample NB08 in new batch

4.4.9.1 Cycle fatigue process

In the sample NB08, the same program was applied to drive the crack into SNTT samples with load control mode. The primary monitoring parameters were listed in Table 30.

Table 30. The monitoring process of NB08 sample through a controlled program

Date	Sample	Run	Frequency	Torque (lbf-in)		Cycle Interval
				Peak	Valley	
08/02/12	NB08	01	5	380	10	5000
08/03/12	NB08	02	5	300	10	5000

The gauge slope evolution process in sample NB06 was shown in Figure 92. It shows that the slope penetrated gradually since count 3. Based on the data in Figure 32, the estimations of corresponding crack penetration ratios were also included, of which the final penetration in sample NB08 was ~0.42.

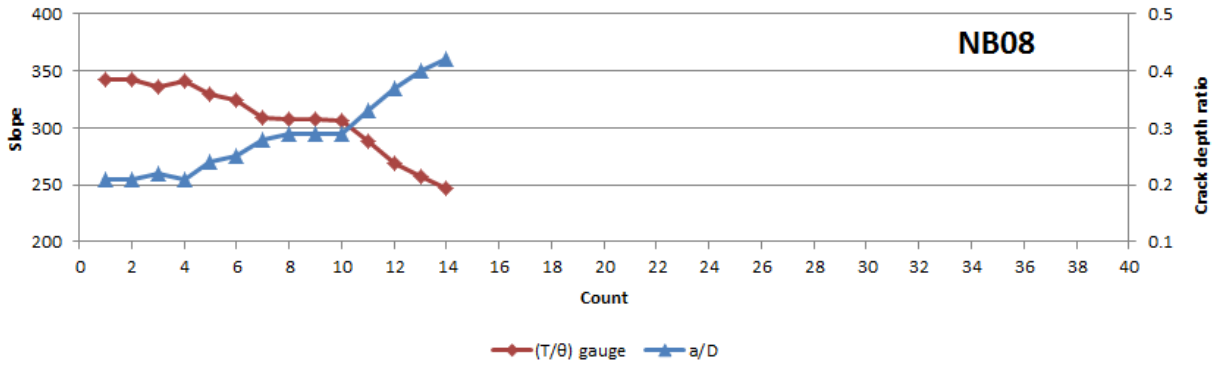

Figure 92.The monitoring curve of crack growth process in SNTT sample NB08.

4.4.9.2 Precracked sample characterization

Figure 93. The precracked SNTT X52 steel sample NB08.

4.4.10 X52 base material sample NB09 in new batch

4.4.10.1 Cycle fatigue process

In the sample NB09, the same program was applied to drive the crack into SNTT samples with load control mode. The primary monitoring parameters were listed in Table 31.

Table 31. The monitoring process of NB09 sample through a controlled program

Date	Sample	Run	Frequency	Torque (lbf-in)		Cycle Interval
				Peak	Valley	
08/03/12	NB09	01	5	380	10	5000
08/04/12	NB09	02	5	300	10	5000

The gauge slope evolution process in sample NB09 was shown in Figure 94. It shows that the slope penetrated gradually since count 3. Based on the data in Figure 32, the estimations of corresponding crack penetration ratios were also included, of which the final penetration in sample NB09 was ~0.43.

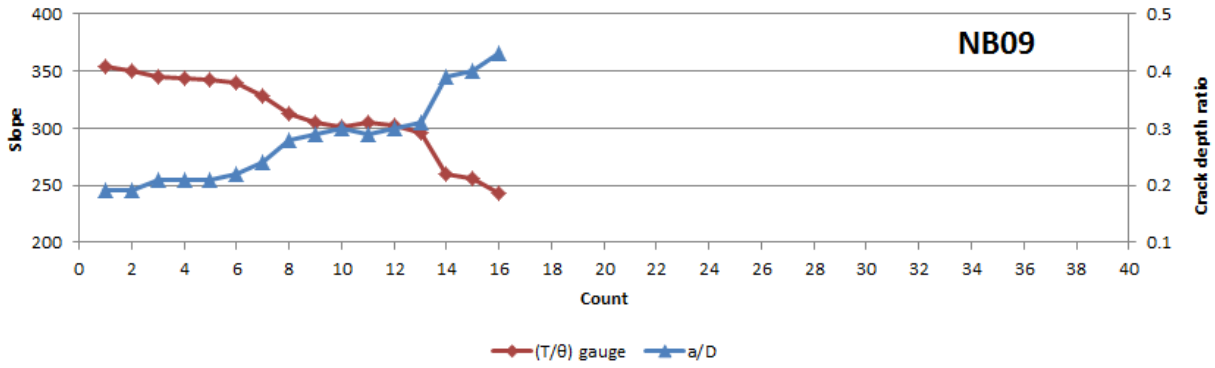

Figure 94.The monitoring curve of crack growth process in SNTT sample NB09.

4.4.10.2 Precracked sample characterization

Figure 95. The precracked SNTT X52 steel sample NB09.

4.4.11 X52 base material sample NB10 in new batch

4.4.11.1 Cycle fatigue process

In the sample NB10, the same program was applied to drive the crack into SNTT samples with load control mode. The primary monitoring parameters were listed in Table 32.

Table 32. The monitoring process of NB10 sample through a controlled program

Date	Sample	Run	Frequency	Torque (lbf-in)		Cycle Interval
				Peak	Valley	
08/03/12	NB10	01	5	380	10	5000
08/04/12	NB10	02	5	300	10	5000

The gauge slope evolution process in sample NB10 was shown in Figure 94. It shows that the slope penetrated gradually since count 3. Based on the data in Figure 32, the estimations of corresponding crack penetration ratios were also included, of which the final penetration in sample NB10 was ~0.44.

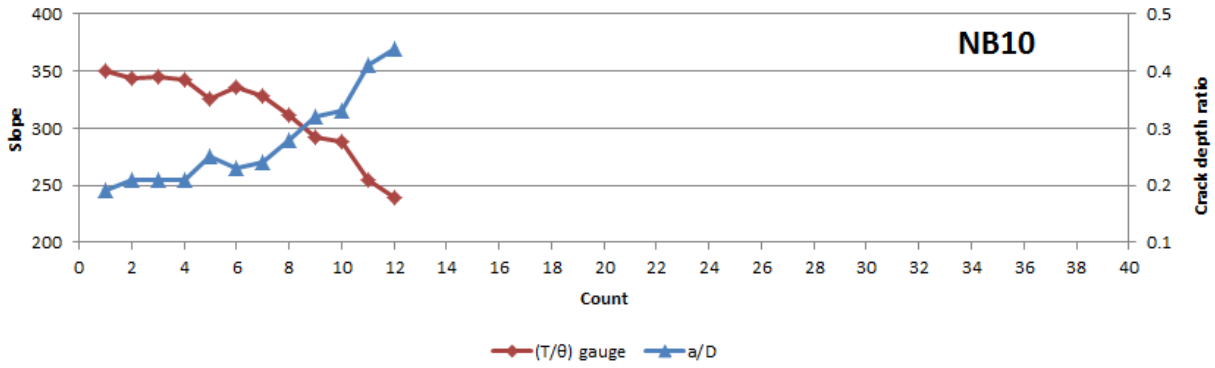

Figure 96.The monitoring curve of crack growth process in SNTT sample NB10.

Precracked sample characterization

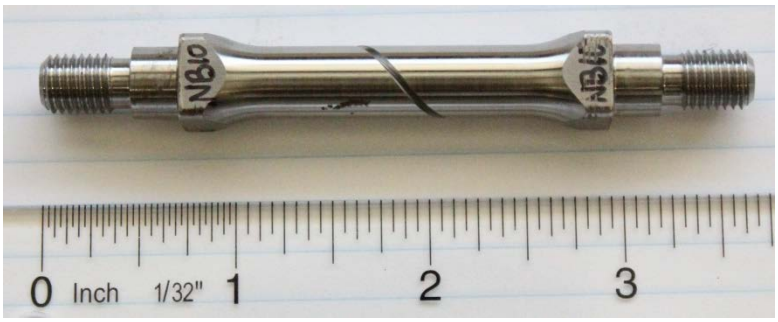

Figure 97. The precracked SNTT X52 steel sample NB10.

4.4.12 X52 base material sample NB11 in new batch

4.4.12.1 Cycle fatigue process

In the sample NB11, the same program was applied to drive the crack into SNTT samples with load control mode. The primary monitoring parameters were listed in Table 33.

Table 33.The monitoring process of NB10 sample through a controlled program

Date	Sample	Run	Frequency	Torque (lbf-in)		Cycle Interval
				Peak	Valley	
08/04/12	NB11	01	5	380	10	5000
08/05/12	NB11	02	5	300	10	5000

The gauge slope evolution process in sample NB11 was shown in Figure 94. It shows that the slope penetrated gradually since count 3. Based on the data in Figure 32, the estimations of corresponding crack penetration ratios were also included, of which the final penetration in sample NB11 was ~0.43.

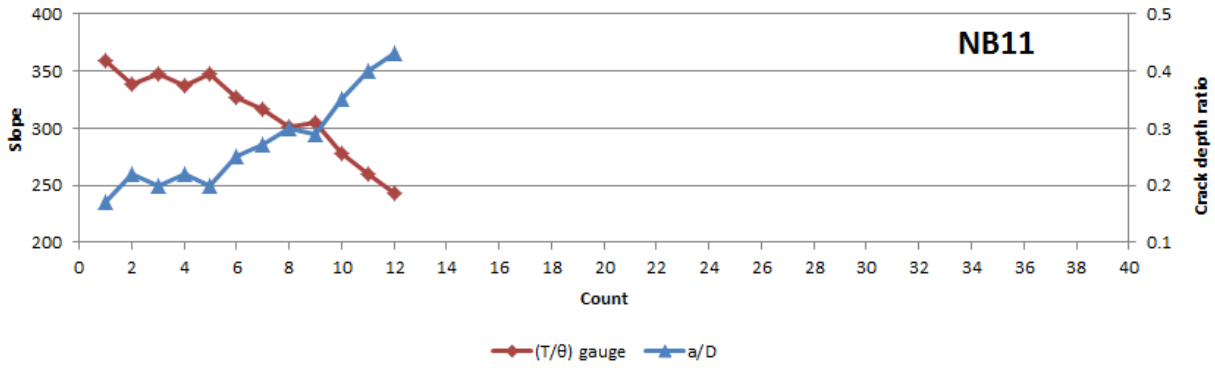

Figure 98. The monitoring curve of crack growth process in SNTT sample NB11.

4.4.12.2 Precracked sample characterization

Figure 99. The precracked SNTT X52 steel sample NB11.

4.5 In air SNTT testing of X52 steel welded materials

4.5.1 X52 welded material sample W1

4.5.1.1 Cycle fatigue process

In the sample W1, the same program was applied to drive the crack into SNTT samples with load control mode. The primary monitoring parameters were listed in Table 34.

Table 34. The monitoring process of W1 sample through a controlled program

Date	Sample	Run	Frequency	Torque (lbf-in)		Cycle Interval
				Peak	Valley	
04/30/12	W1	01	2	380	10	5000
04/30/12	W1	02	2	380	10	5000

The gauge slope evolution process in sample W1 was shown in Figure 100. It shows that the slope stayed almost in the same level before the count 14. Then the crack penetrated quickly between count 14 and 20. The program ended soon after this jump since the end rotation angle reached the critical angle limit. After count 20, the slope measurement stayed in the same level.

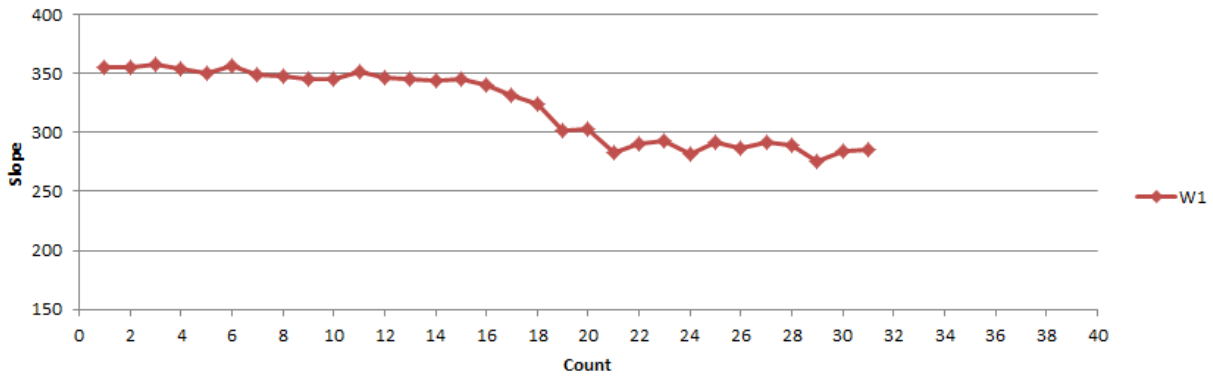

Figure 100. The monitoring curve of crack growth process in SNTT sample B12.

4.5.1.2 Failed sample characterization

When the program ended, the sample was cut into parts using a diamond saw Labcut 1010 (Extec, Enfield, CT) to check the actual crack depth. A cut was performed perpendicular to the cylindrical axis in middle section (Figure 101). In the cross section the measured ratios of crack depth to diameter were 0.29 and 0.28 on both sides (Figure 102.

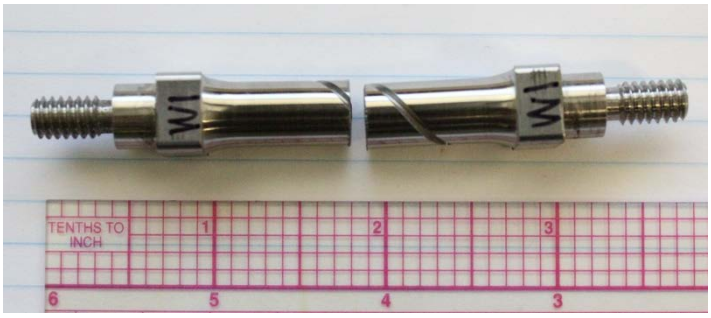

Figure 101. The failed W1 specimen in X52 welded steel series.

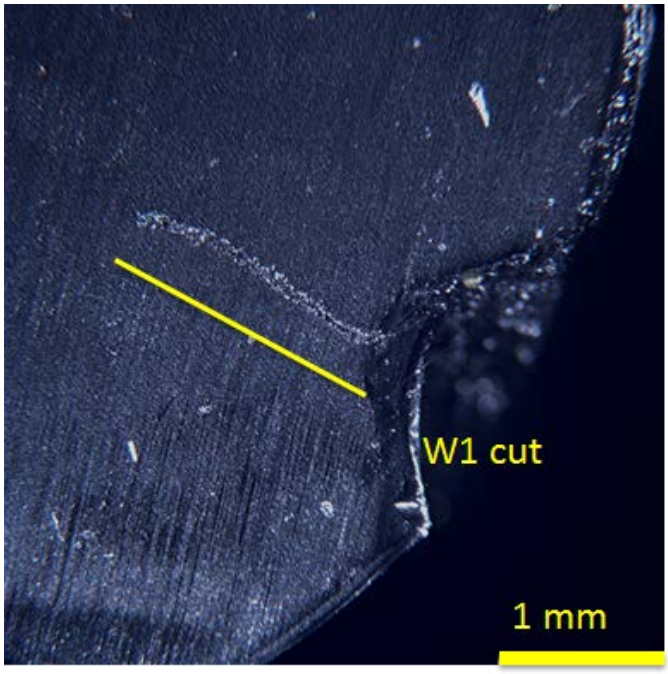

(a)

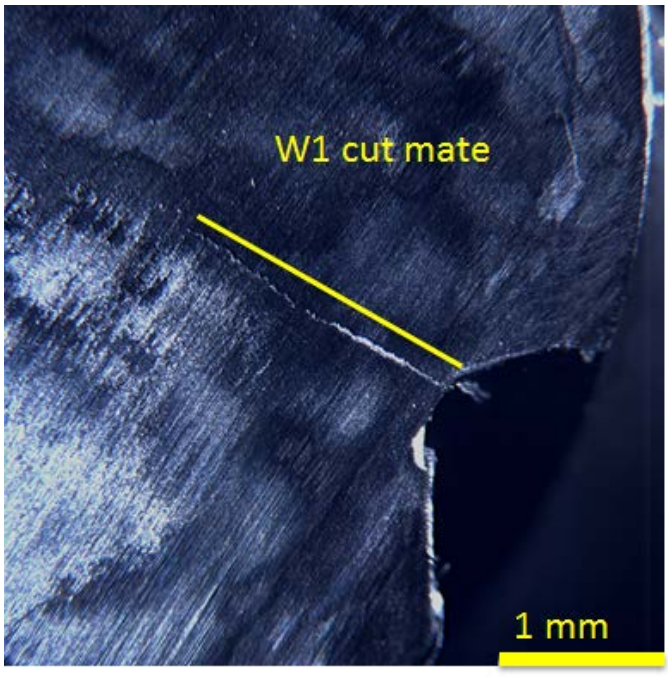

(b)

Figure 102. The crack depth with a cut in the middle section of sample W1 after fatigue precrack process: (a) cut; (b) cut mate.

4.5.2 X52 welded material sample W2

4.5.2.1 Cycle fatigue process

In the sample W2, the same program was applied to drive the crack into SNTT samples with load control mode. The primary monitoring parameters were listed in Table 35.

Table 35. The monitoring process of W2 sample through a controlled program

Date	Sample	Run	Frequency	Torque (lbf-in)		Cycle Interval
				Peak	Valley	
04/30/12	W2	01	2	380	10	5000
04/30/12	W2	02	2	380	10	5000

The gauge slope evolution process in sample W2 was shown in Figure 103. It shows that the slope stayed almost in the same level before the count 18. Then the crack penetrated quickly between count 18 and 26. The program ended soon after this jump since the end rotation angle reached the critical angle limit. After count 26, the slope measurement stayed in the same level.

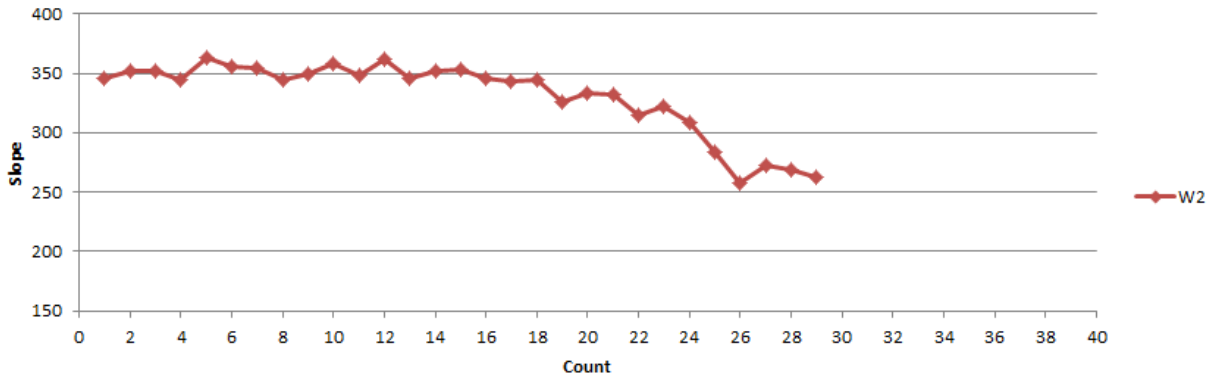

Figure 103. The monitoring curve of crack growth process in SNTT sample W2.

4.5.2.2 Failed sample characterization

When the program ended, the sample was cut into parts using a diamond saw Labcut 1010 (Extec, Enfield, CT) to check the actual crack depth. A cut was performed perpendicular to the cylindrical axis in middle section (Figure 104). In the cross section the measured ratios of crack depth to diameter were 0.40 and 0.41 on both sides (Figure 105). The other part of the W2 sample is with staff at Ohio State University for material characterization.

Figure 104. The failed W2 specimen in X52 welded steel series.

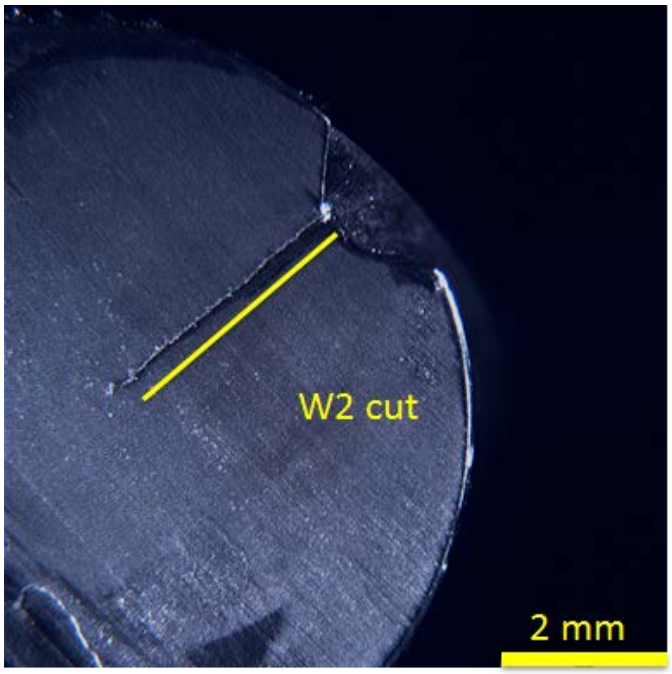

(a)

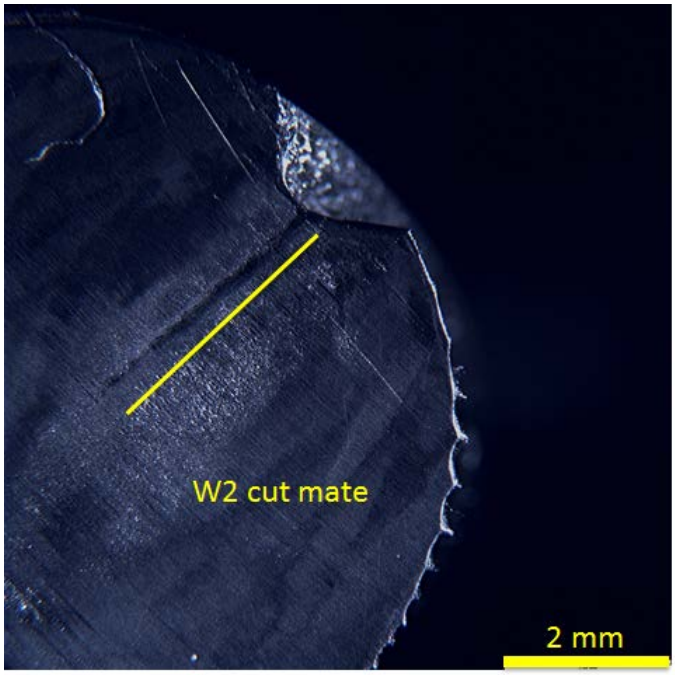

(b)

Figure 105. The crack depth with a cut in the middle section of sample W2 after fatigue precrack process: (a) cut; (b) cut mate.

4.5.3 X52 welded material sample W3

4.5.3.1 Cycle fatigue process

In the sample W3, the same program was applied to drive the crack into SNTT samples with load control mode. The primary monitoring parameters were listed in Table 36 . The gauge slope evolution process in sample W3 was shown in Figure 103. It shows that the slope decreased gradually from the beginning of the experiment.

Table 36. The monitoring process of W3 sample through a controlled program

Date	Sample	Run	Frequency	Torque (lbf-in)		Cycle Interval
				Peak	Valley	
05/03/12	W3	01	2	380	10	5000
05/04/12	W3	02	5	200	10	5000
05/04/12	W3	03	5	100	10	5000
05/04/12	W3	04	5	150	10	5000
05/04/12	W3	05	5	150	10	5000

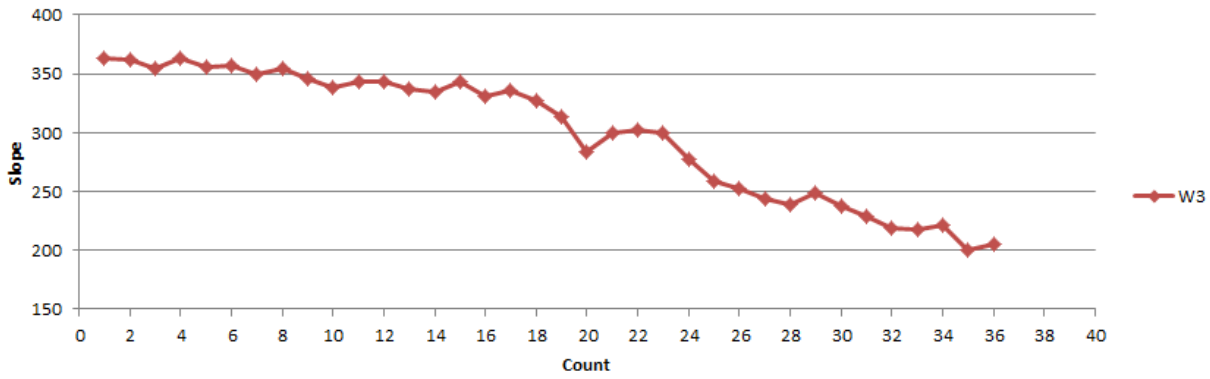

Figure 106. The monitoring curve of crack growth process in SNTT sample W3.

4.5.3.2 Failed sample characterization

When the program ended, the sample was cut into parts using a diamond saw Labcut 1010 (Extec, Enfield, CT) to check the actual crack depth. A cut was performed perpendicular to the cylindrical axis in middle section (Figure 107); the other parallel cut was performed in a location away from the previous cut. In the middle section, the cracks deviated from the circle center as the penetration depth increased (Figure 108), which were shown on both sides of the cut sample. One reason for this deviation may be due to the inhomogeneity of the welded materials, which led the cracks to the weakest tour during the cycle fatigue process. Further effort is needed to characterize the effect of material inhomogeneity on the crack penetration path of SNTT method.

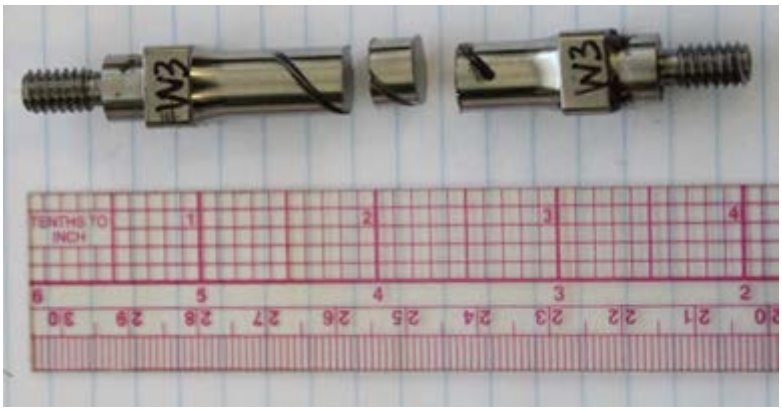

Figure 107. The failed W3 specimen in X52 welded steel series.

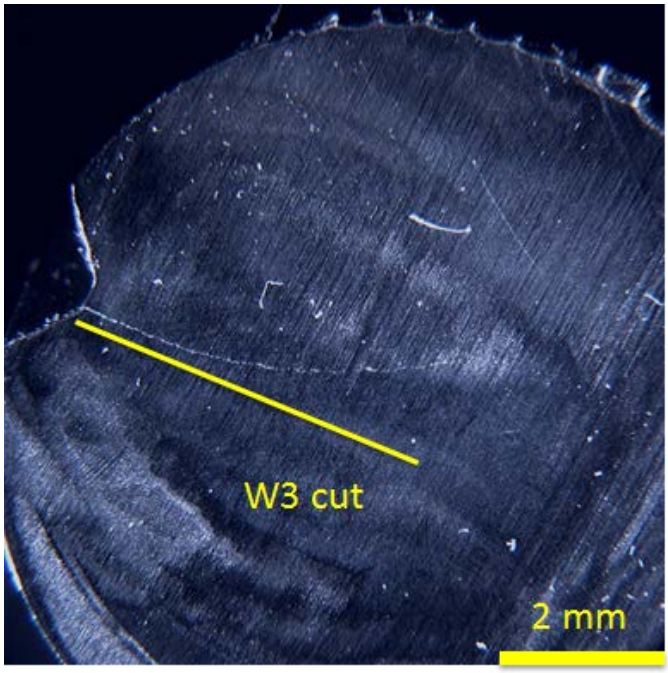

(a)

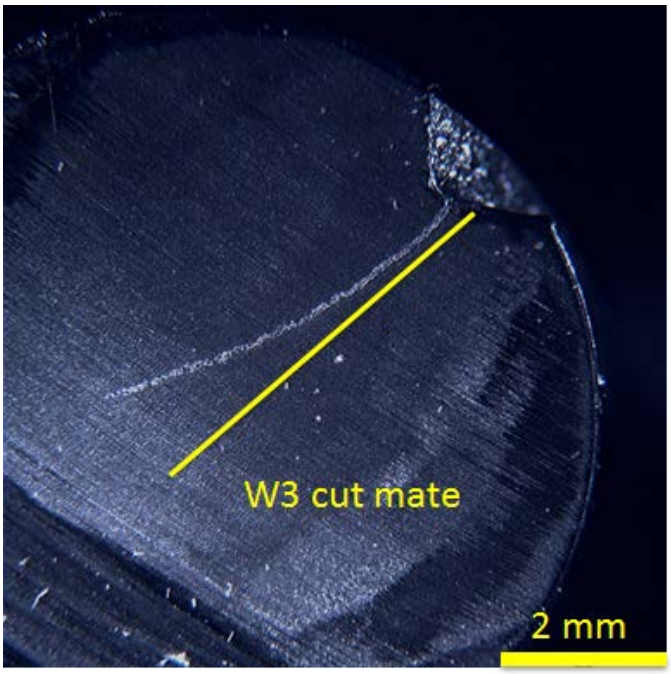

(b)

Figure 108. The crack depth with a cut in the middle section of sample W2 after fatigue precrack process: (a) cut; (b) cut mate.

4.5.4 X52 welded material sample W4

4.5.4.1 Cycle fatigue process

In the sample W4, the same program was applied to drive the crack into SNTT samples with load control mode. The primary monitoring parameters were listed in Table 37. The gauge slope evolution process in sample W4 was shown in Table 37. It shows that the slope stayed almost in the same level before the count 22. Then the crack penetrated quickly between count 22 and 34. The program ended soon after this jump since the end rotation angle reached the critical angle limit. After count 34, the slope measurement stayed in the same level.

Table 37. The monitoring process of W4 sample through a controlled program

Date	Sample	Run	Frequency	Torque (lbf-in)		Cycle Interval
				Peak	Valley	
05/03/12	W4	01	1	380	10	5000
05/04/12	W4	02	5	300	10	5000

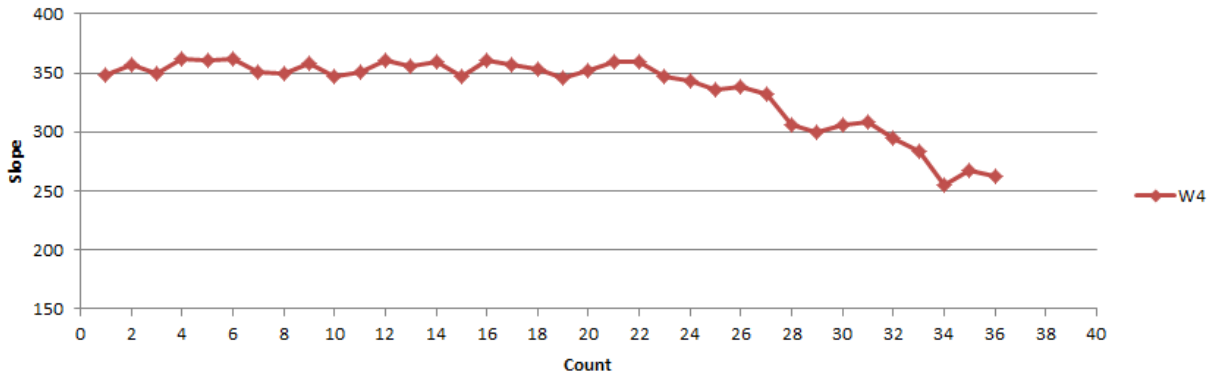

Figure 109. The monitoring curve of crack growth process in SNTT sample W4.

4.5.4.2 Precracked W4 sample

Cracks have been introduced to the SNTT W4 sample during the cycle fatigue process. It is ready for fracture toughness measurement by coupling acoustic emission or biaxial extensometer techniques (Figure 110).

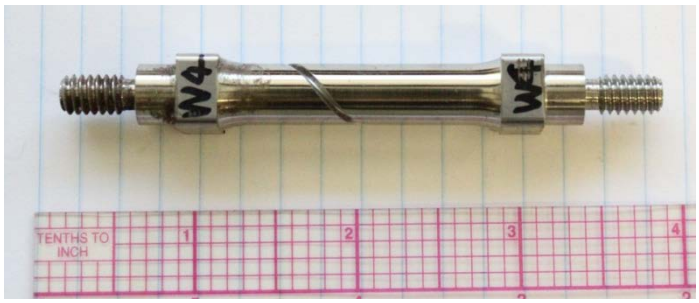

Figure 110. The fatigue precracked SNTT welded material sample W4.

4.5.5 X52 welded material sample W5

4.5.5.1 Cycle fatigue process

In the sample W5, the same program was applied to drive the crack into SNTT samples with load control mode. The primary monitoring parameters were listed in Table 38. The gauge slope evolution process in sample W5 was shown in Figure 111. It shows that the slope stayed almost in the same level before the count 18. Then the crack penetrated quickly between count 18 and 35. The program ended soon after this jump since the end rotation angle reached the critical angle limit. After count 35, the slope measurement stayed in the same level.

Table 38. The monitoring process of W5 sample through a controlled program

Date	Sample	Run	Frequency	Torque (lbf-in)		Cycle Interval
				Peak	Valley	
05/11/12	W5	01	2	380	10	5000
05/12/12	W5	02	5	300	10	5000
05/13/12	W5	03	5	300	10	5000
05/14/12	W5	04	5	250	10	5000

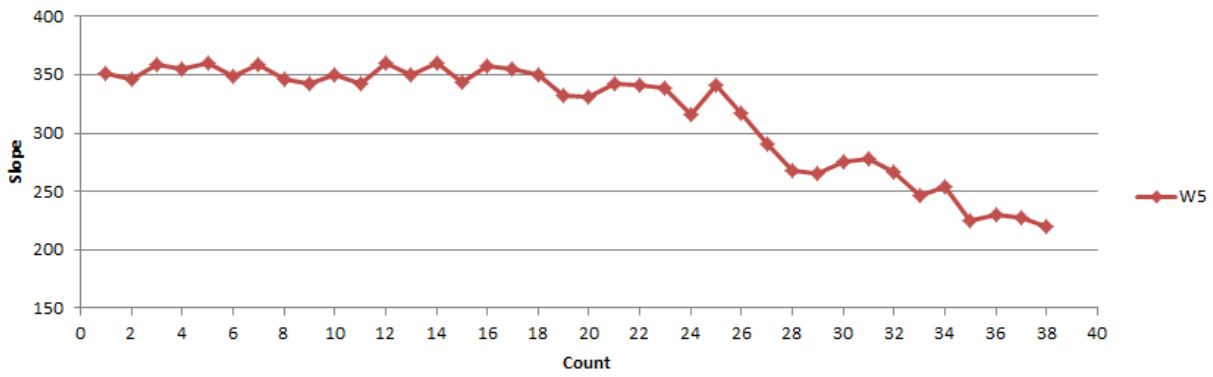

Figure 111. The monitoring curve of crack growth process in SNTT sample W5.

4.5.5.2 Precracked W5 sample

Cracks have been introduced to the SNTT W5 sample during the cycle fatigue process. It is ready for fracture toughness measurement by coupling acoustic emission or biaxial extensometer techniques (Figure 112).

Figure 112. The fatigue precracked SNTT welded material sample W5.

4.5.6 X52 welded material sample W6

4.5.6.1 Cycle fatigue process

In the sample W5, the same program was applied to drive the crack into SNTT samples with load control mode. The primary monitoring parameters were listed in Table 39. The gauge slope

evolution process in sample W6 was shown in Figure 113. It shows that the slope stayed almost in the same level before the count 22. Then the crack penetrated quickly between count 22 and 33. The program ended soon after this jump since the end rotation angle reached the critical angle limit. After the count 33, the slope measurement stayed in the same level.

Table 39. The monitoring process of W6 sample through a controlled program

Date	Sample	Run	Frequency	Torque (lbf-in)		Cycle Interval
				Peak	Valley	
05/15/12	W6	01	5	380	10	5000
05/16/12	W6	02	5	300	10	5000
05/16/12	W6	03	5	300	10	5000

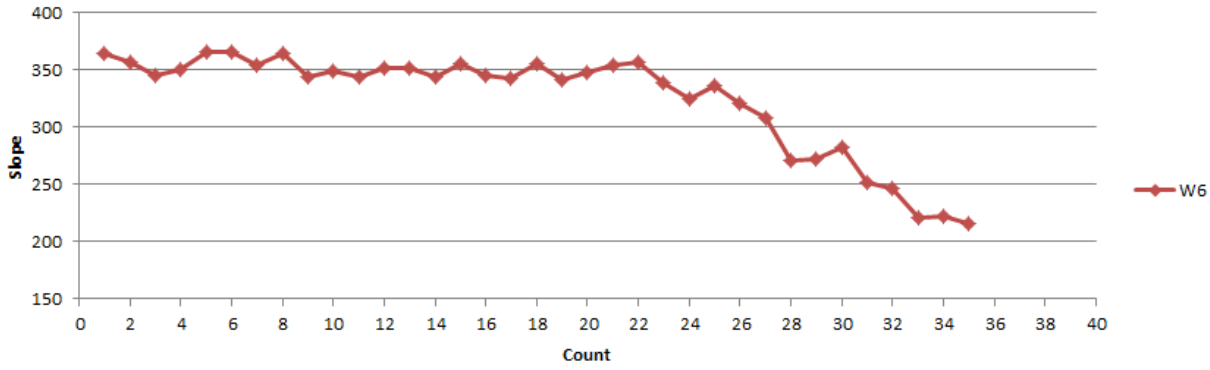

Figure 113. The monitoring curve of crack growth process in SNTT sample W6.

4.5.6.2 Failed W6 sample

Cracks have been introduced to the SNTT W6 sample during the cycle fatigue process. The W6 sample was used to test the acoustic emission machine for a loading-unloading test (Figure 114), which was not successful for this trial. In the meantime, W6 sample yielded during the testing process.

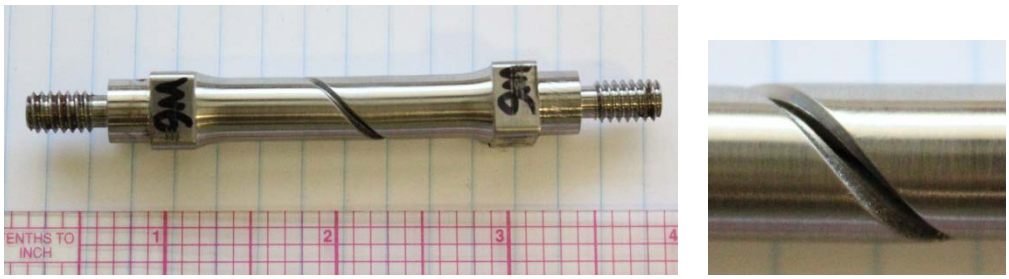

(a) (b)

Figure 114. The failed SNTT welded material sample W6: (a) the entire view; (b) the local view of the failed sample.

4.5.7 X52 welded material sample W7

4.5.7.1 Cycle fatigue process

In the sample W7, the same program was applied to drive the crack into SNTT samples with load control mode. The primary monitoring parameters were listed in Table 40. The gauge slope evolution process in sample W7 was shown in Figure 115. It shows that the slope stayed almost in the same level before the count 18. Then the crack penetrated quickly between count 18 and 46. The program ended soon after this jump since the end rotation angle reached the critical angle limit. After count 46, the slope measurement stayed in the same level.

Table 40. The monitoring process of W7 sample through a controlled program

Date	Sample	Run	Frequency	Torque (lbf-in)		Cycle Interval
				Peak	Valley	
05/16/12	W7	01	5	380	10	5000
05/17/12	W7	02	5	380	10	5000
05/17/12	W7	03	5	200	10	5000

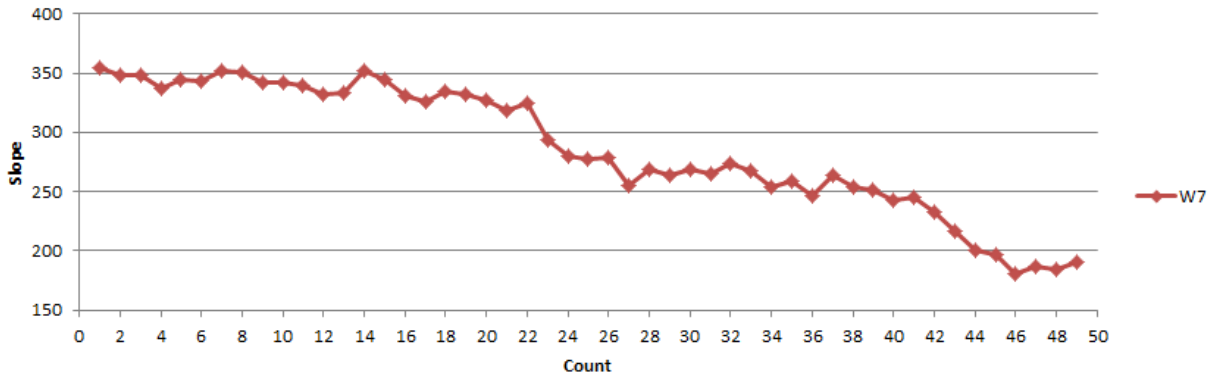

Figure 115. The monitoring curve of crack growth process in SNTT sample W7.

4.5.7.2 Failed W7 sample

Cracks have been introduced to the SNTT W7 sample during the cycle fatigue process. The W7 sample was used to test the acoustic emission machine for a loading-unloading test (Figure 116), which was not successful for this trial. In the meantime, W7 sample yielded during the testing process.

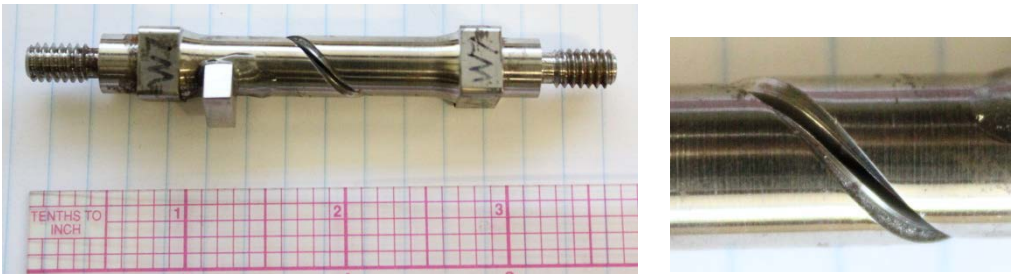

(a) (b)

Figure 116. The failed SNTT welded material sample W7: (a) the entire view; (b) the local view of the failed sample.

4.5.8 X52 welded material sample W8

4.5.8.1 Cycle fatigue process

In the sample W8, the same program was applied to drive the crack into SNTT samples with load control mode. The primary monitoring parameters were listed in Table 41. The gauge slope evolution process in sample W8 was shown in Figure 117. In the figure, the slope decreased gradually from the beginning of the experiment.

Table 41. The monitoring process of W8 sample through a controlled program

Date	Sample	Run	Frequency	Torque (lbf-in)		Cycle Interval
				Peak	Valley	
05/21/12	W8	01	5	420	10	5000
05/22/12	W8	02	5	250	10	5000
05/23/12	W8	03	5	200	10	5000
05/23/12	W8	04	2	200	10	5000

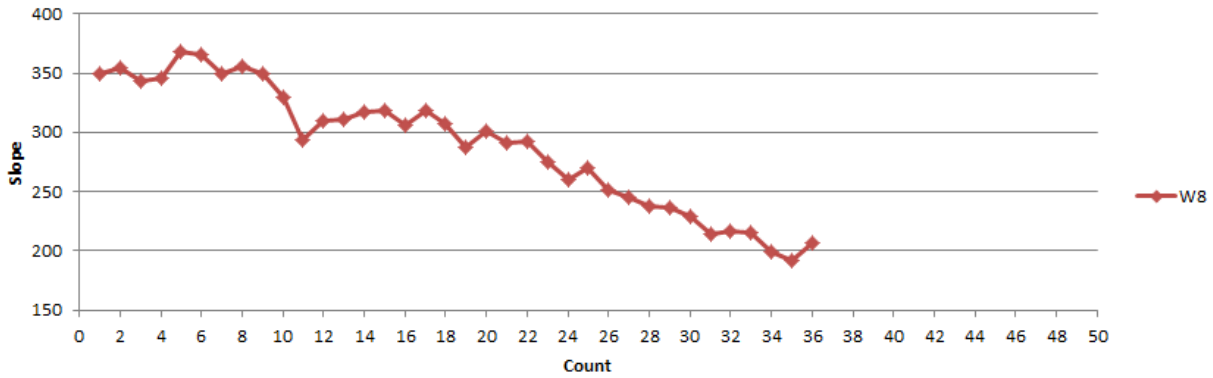

Figure 117. The monitoring curve of crack growth process in SNTT sample W8.

4.5.8.2 Failed W8 sample

Cracks have been introduced to the SNTT W5 sample during the cycle fatigue process. It is ready for fracture toughness measurement by coupling acoustic emission or biaxial extensometer techniques (Figure 118).

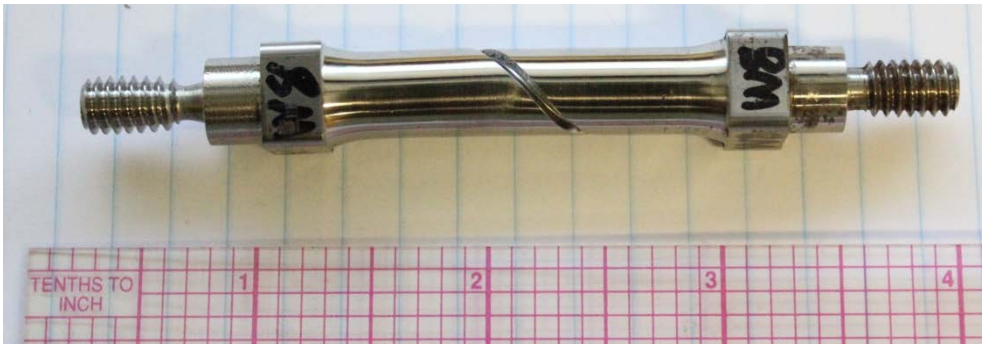

Figure 118. The fatigue precracked SNTT welded material sample W8.

4.6 In air SNTT testing of X80 steel welded materials

4.6.1 X80 sample design

In this approach, X80 SNTT samples were fabricated from a segment of the friction stir welded X80 steel pipe. Since the thickness of the pipe is 0.5 inch, the diameter of the SNTT cylinder was designed to be 0.375 inch (Figure 34. Actual dimension of Friction Stir Welded X52 steel pipe. The SNTT specimen axis was parallel to the pipe cylinder axis. Two entire loops were machined in the X80 SNTT sample.

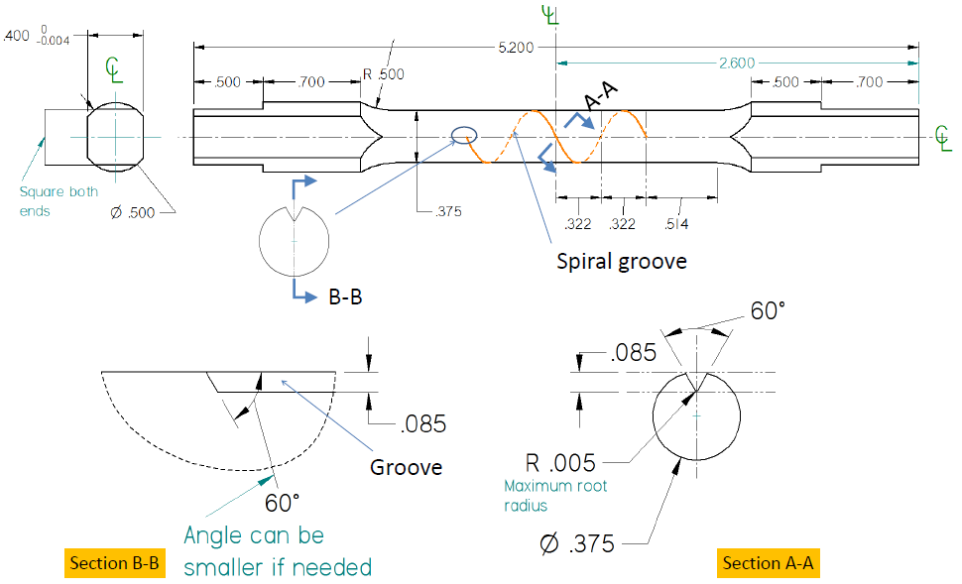

Figure 119. Sketch of X80 SNTT sample

4.6.2 X80 welded material sample X80B3

4.6.2.1 Cycle fatigue process

In the sample X80B03, the same program was applied to drive the crack into SNTT samples with load control mode. The primary monitoring parameters were listed in Table 42.

Table 42. The monitoring process of X80B3 sample through a controlled program

Date	Sample	Run	Frequency	Torque (lbf-in)		Cycle Interval
				Peak	Valley	
07/12/12	X80B03	01	5	150	10	5000

4.6.2.2 Failed X80B3 sample

Cracks have been introduced to the SNTT X80B03 sample during the cycle fatigue process. The precracked sample was cut in cross sections (Figure 120). By using dye penetrant (Magnaflux, Glenview, IL), cracks were detected in the middle section as shown in Figure 121. By measuring the area covered with dye penetrant, the notch-over-diameter ratio was ~ 0.39.

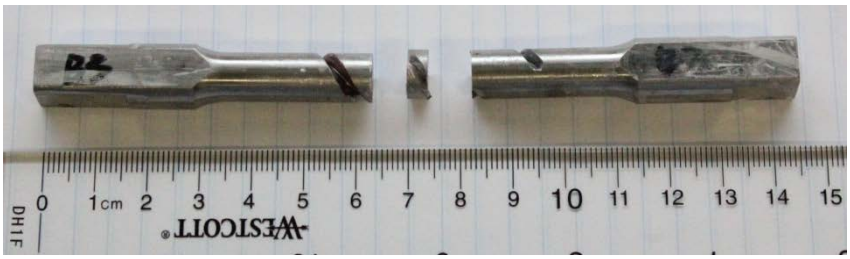

Figure 120. Section-Cut SNTT specimen X80B3.

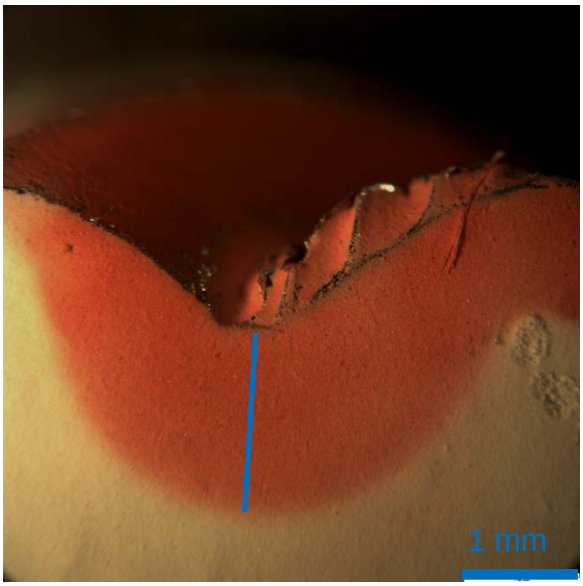

Figure 121. Middle sections with dye penetrant of SNTT specimen X80B3.

4.6.2.3 Acoustic emission test

Acoustic emission machine (Physical Acoustic Inc., Princeton Junction, NJ) was used to detect the initial pop-in moment during the loading-unloading test of SNTT samples. The experimental data and was shown in Figure 122. When the first pop-in appeared, the applied torque was ~91.7 lbf-in. By using Figure 32and Figure 33, the energy release rate upon the first pop-in moment was 1.35 lbf/in.

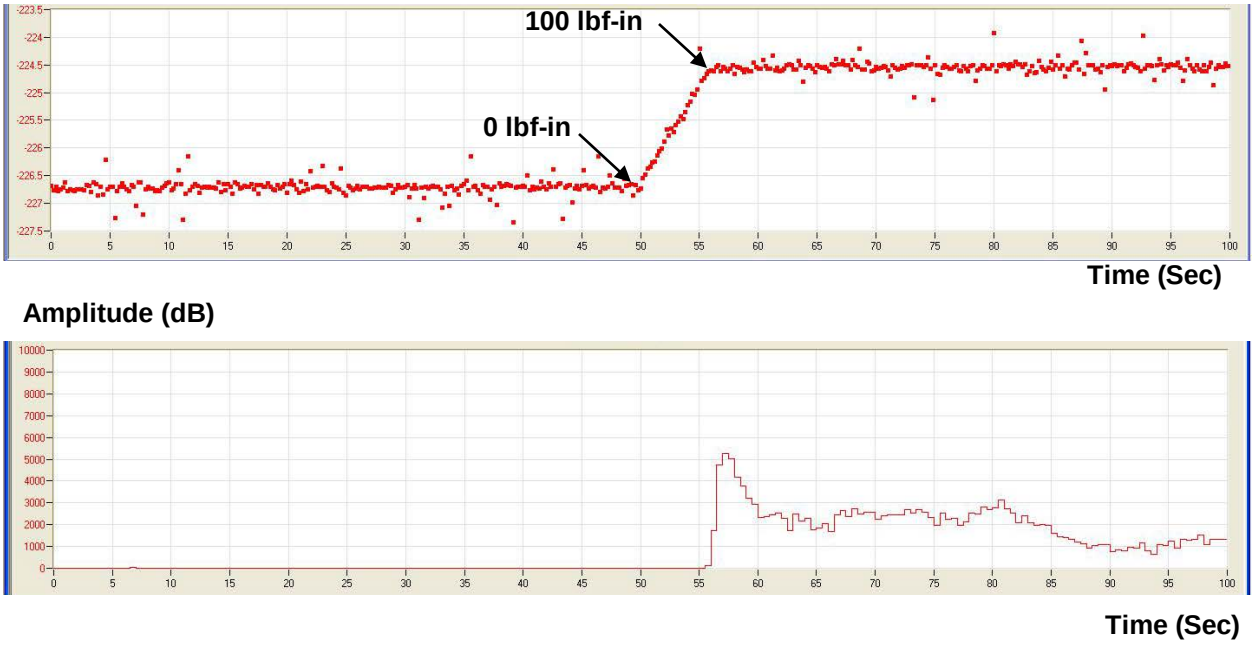

Figure 122. Acoustic emission data of loading-unloading test of specimen X80B3

4.6.3 X80 welded material sample X80B4

4.6.3.1 Cycle fatigue process

In the sample X80B04, the same program was applied to drive the crack into SNTT samples with load control mode. The primary monitoring parameters were listed in Table 43.

Table 43. The monitoring process of X80B4 sample through a controlled program

Date	Sample	Run	Frequency	Torque (lbf-in)		Cycle Interval
				Peak	Valley	
07/16/12	X80B05	01	5	150	10	5000

4.6.3.2 Failed X80B4 sample

Cracks have been introduced to the SNTT X80B04 sample during the cycle fatigue process. The precracked sample was cut in cross sections (Figure 123). By using dye penetrant (Magnaflux, Glenview, IL), cracks were detected in the middle section as shown in Figure 124. By measuring the area covered with dye penetrant, the notch-over-diameter ratio was ~ 0.33.

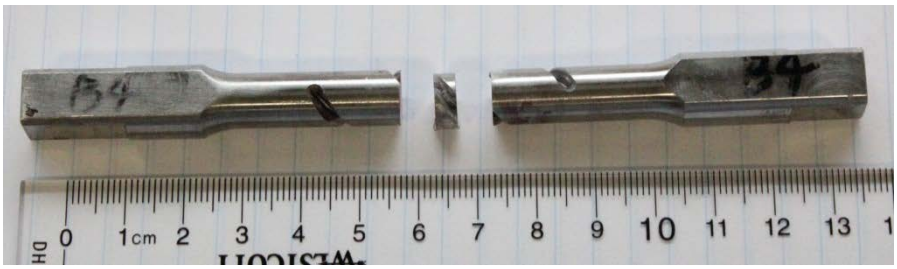

Figure 123. Section-Cut SNTT specimen X80B4.

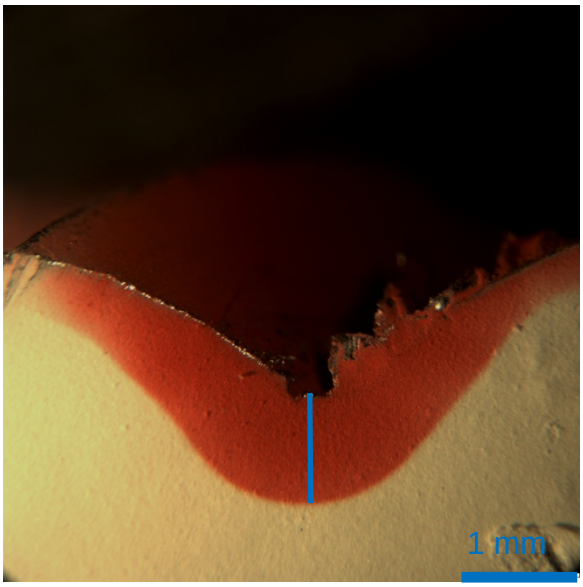

Figure 124. Middle sections with dye penetrant of SNTT specimen X80B4.

4.6.3.3 Acoustic emission test

The acoustic emission and the loading-unloading data were shown in Figure 125. When the first pop-in appeared, the applied torque was ~49.0 lbf-in. By using Figure 32and Figure 33, the energy release rate upon the first pop-in moment was 0.33 lbf/in.

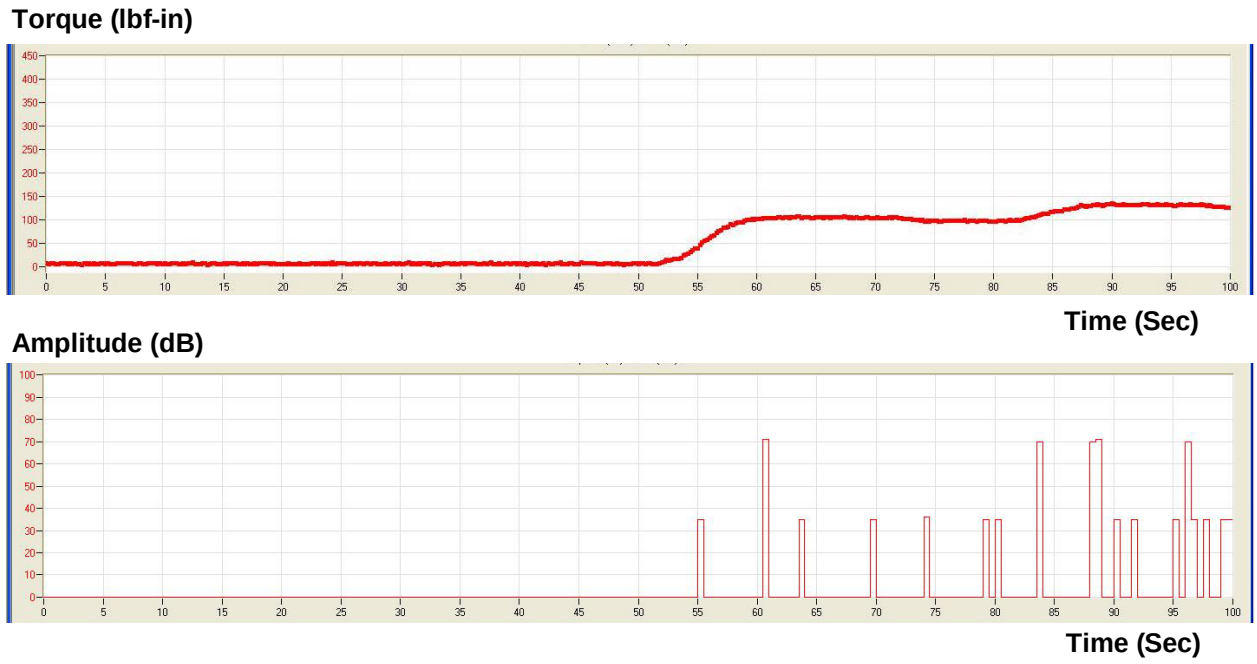

Figure 126. Acoustic emission data of loading-unloading test of specimen X80B4

4.6.4 X80 welded material sample X80B5

4.6.4.1 Cycle fatigue process

The cycle fatigue process (Table 44) of sample X80B5 was also performed through the angle control mode by the same function generator built in the MTS system. In order to find the fatigue threshold of the X80 SNTT samples, the initial maximum torque was adjusted to around 150 lbf-in 5 HZ cyclic fatigue process. This cyclic load was increased to 200 lbf-in after 1.2 million cycles, the dynamic torque decreased quickly to 150 lbf-in with a fast crack penetration.

Table 44. The monitoring process of X80B5 sample through a function generator

Date	Time (EST)	Mean (degree)	Amplitude (degree)	Freq	Torque (lbf-in)		Theta (degree)		Count
					Peak	Valley	Peak	Valley	
07/17/12	14:20	7.2	1.8	5	146.33	2.97	8.10	2.90	1,020
07/18/12	9:00	7.2	1.8	5	147.00	-0.08	8.10	6.29	
07/18/12	11:22	7.2	1.8	5	147.80	0.22	8.10	6.29	
07/18/12	15:24	7.2	1.8	5	146.60	1.75	8.10	6.29	451,860
07/18/12	17:56	7.2	1.8	5	147.86	-0.08	8.10	6.30	497,450
07/19/12	9:01	7.2	1.8	5	146.60	1.75	8.10	6.30	774,556
07/19/12	13:55	7.2	1.8	5	146.60	2.05	8.10	6.29	857,400
07/19/12	16:39	7.2	1.8	5	146.90	0.53	8.10	6.29	906,760

07/20/12	9:30	7.2	1.8	5	146.00	2.05	8.10	6.30	1,209,430
07/20/12	12:30	7.85	2.0	5	201.80	38.66	8.85	6.85	1,264,700
07/20/12	14:30	7.85	2.0	5	152.10	25.80	8.85	6.85	1,300,000

4.6.4.2 Failed X80B5 sample

X80B05 sample split into two halves at failure (Figure 127). By checking the local view of the fracture surface (Figure 128), distinctive areas could be found for fatigue or monotonic loading process, similar to the situation shown in X52 sample. Optical images of the fracture surfaces were shown in Figure 129, from which the notch-to-diameter ratio was ~0.66.

(a) (b)

Figure 127. Failed SNTT specimen X80B05: (a) one half; (b) the mating half.

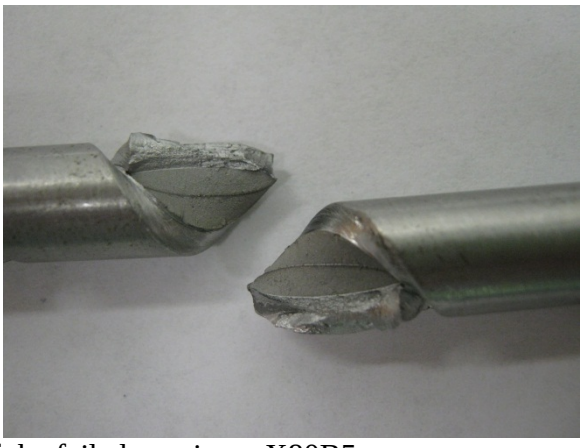

Figure 128. Local view of the failed specimen X80B5.

(a) (b)

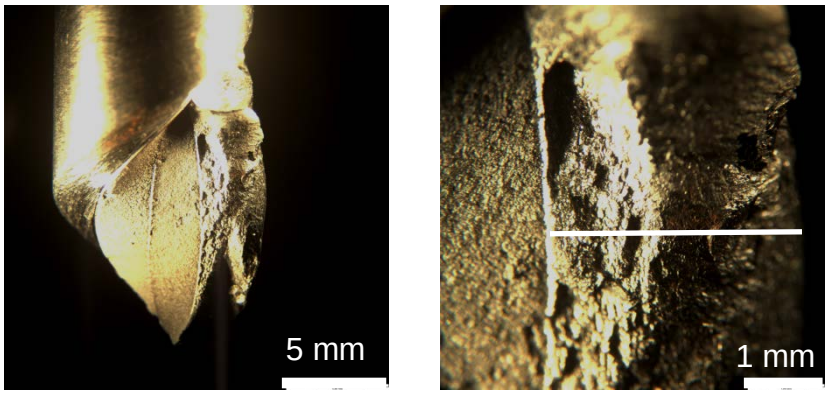

Figure 129. Optical images fracture surfaces of X80B5: (a) lower mag; (b) higher mag.

4.6.4.3 Acoustic emission test

The acoustic emission and the loading-unloading data were shown in Figure 130. When the first pop-in appeared, the applied torque was ~20.0 lbf-in. Further efforts in numerical modeling should be devoted to analyze the energy release rate at this scenario.

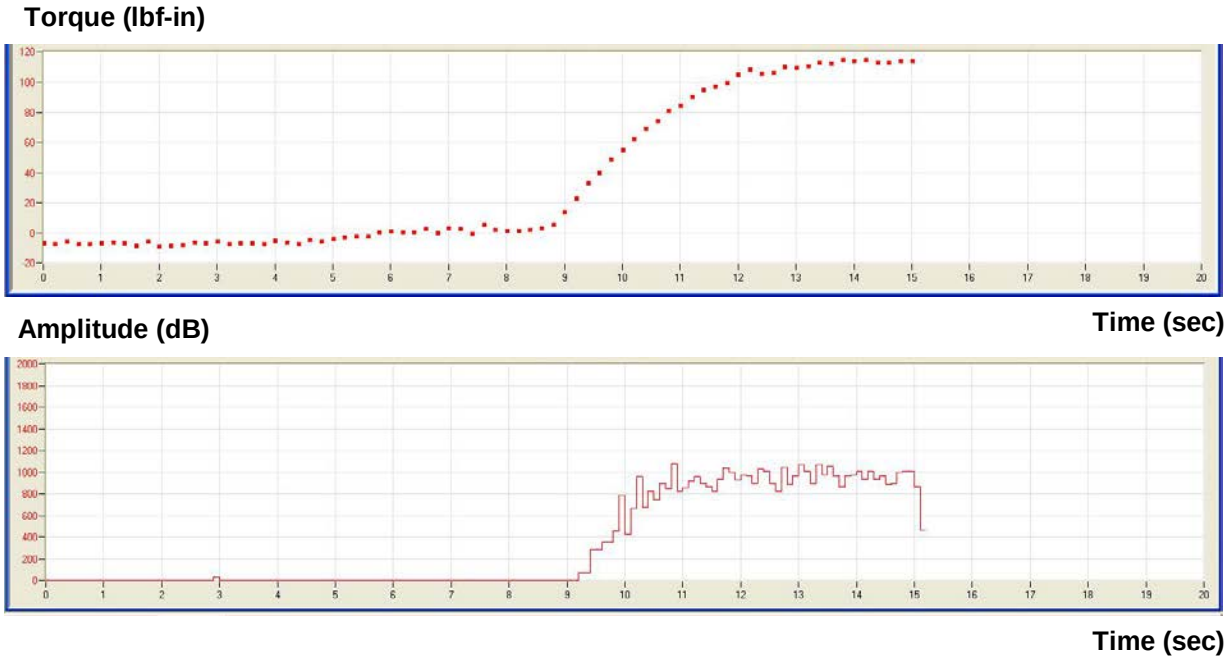

Figure 131. Acoustic emission data of loading-unloading test of specimen X80B5.

4.6.5 X80 welded material sample X80B6

4.6.5.1 Cycle fatigue process

In the sample X80B06, the same program was applied to drive the crack into SNTT samples with load control mode. The primary monitoring parameters were listed in Table 42.

Table 45. The monitoring process of X80B4 sample through a controlled program

Date	Sample	Run	Frequency	Torque (lbf-in)		Cycle Interval
				Peak	Valley	
07/22/12	X80B06	01	5	150	10	5000

4.6.5.2 Failed X80B6 sample

Cracks have been introduced to the SNTT X80B06 sample during the cycle fatigue process. The precracked sample was cut in cross sections (Figure 132). By using dye penetrant (Magnaflux, Glenview, IL), cracks were detected in the middle section as shown Figure 133. By measuring the area covered with dye penetrant, the notch-over-diameter ratio was ~ 0.30.

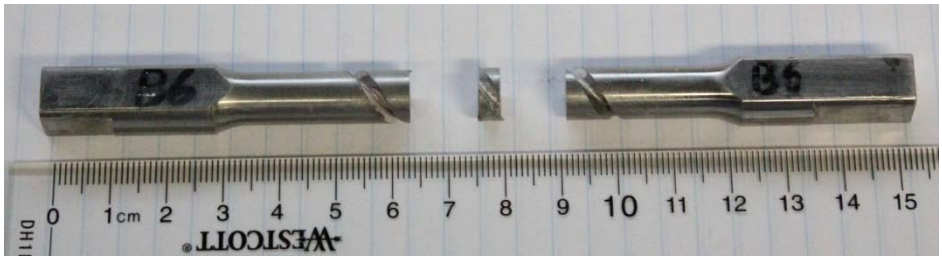

Figure 132. Section-Cut SNTT specimen X80B06.

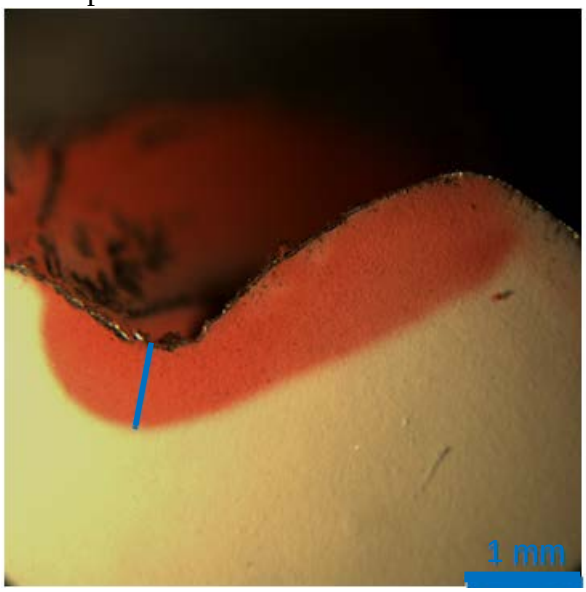

Figure 133. Middle sections with dye penetrant of SNTT specimen X80B6.

4.6.5.3 Acoustic emission test

The acoustic emission and the loading-unloading data were shown in . When the first pop-in appeared, the applied torque was ~115.0.0 lbf-in. By using Figure 32and Figure 33, the energy release rate upon the first pop-in moment was 1.67 lbf/in.

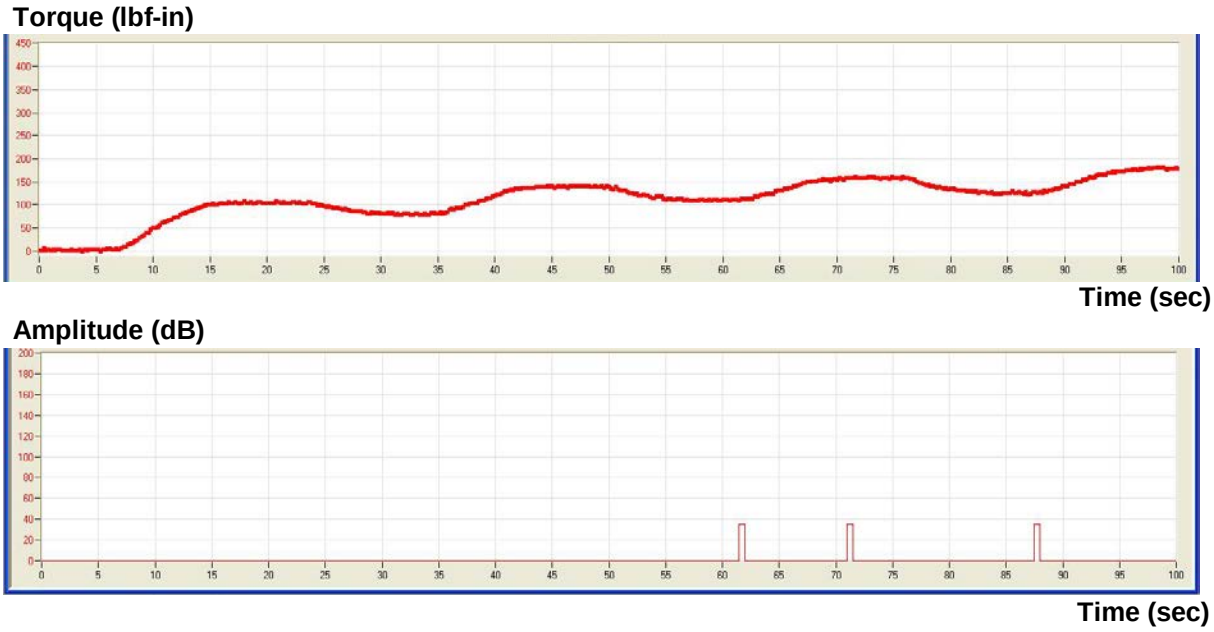

Figure 134. Acoustic emission data of loading-unloading test of specimen X80B6.

5. Future work

It has been demonstrated that the compliance study of SNTT method is successful in capturing the crack penetration during the cycle fatigue process. However, the current prediction only covers the ratio of crack depth to diameter from 0.10 to 0.45. Further work in both numerical modeling and experimental validation are needed to extend beyond this range. This will be helpful to fully understand and control the crack growth in SNTT method.

For the X52 steel base material, precracks were introduced to SNTT samples in the new batch systematically following the recently developed precrack protocol. With these pre-cracked SNTT samples, measurement of fracture toughness of these tough materials can then be performed in air, with auxiliary acoustic device to catch the crack initiation. The results will also be useful for future design and development of X52 steel.

On the other hand, the crack penetration pattern of X52 welded material will also be an interesting topic in the future. Based on current findings of the crack deviation in the welded material, the effect of material inhomogeneity on the crack penetration pattern under torsion cyclic loading conditions will be a new and exciting direction. The effort in both numerical modeling and experimental measurement can provide critical guidance in the failure prevention of friction stir welded structure.

In terms of hydrogen embrittlement, the next step will be to perform the in-situ SNTT test for both X52 base and welded material in the pressurized hydrogen environment. Further effort of developing the hydrogen loading frame that is suitable for the current X52 sample design is needed for the performing in-situ SNTT measurement in hydrogen environment. The SNTT samples can be precraced in the air, which will then be loaded into the hydrogen environment for in-situ testing. These results will be valuable for characterization of both X52 steel base and welded material under hydrogen environment.

6. Summary

The spiral notch torsion test (SNTT) has been utilized to investigate the crack growth behavior of X52 steel base and welded materials used for hydrogen infrastructures. The X52 steel materials are received from a welded pipe using friction stir welding techniques. The base materials are machined from the pipe section; while the welded materials are machined from the welded section.

Finite element models were established to study the crack growth behavior of steel SNTT steel samples, which were assumed to be isotropic material. A series SNTT models were set up to cover various crack penetration cases, of which the ratios between crack depth to diameter (a/D ratio) ranging from 0.10 to 0.45. The evolution of compliance and energy release rates in the SNTT method have been investigated with different cases, including different geometries and materials.

Indices of characteristic compliance and energy release rates have been proposed. Good agreement has been achieved between predictions from different cases in the same trend. These work shed lights on a successful protocol for SNTT application in wide ranges of structural materials. The further effort needed for compliance function development is to extend the current developed compliance function to the deep crack penetration arena, in the range of 0.55 to 0.85 to effectively determine fracture toughness for extremely tough materials.

All SNTT samples tested were machine with a 45^{o} pitch angel spiral groove to the cylinder axis. Two different methods were used during the cyclic fatigue loading process. One approach is the angle control method in a built in function generator. The development of torque and angle during the monitoring process is recorded accordingly. The other approach is torque control method with a built program in MTS system. The primary monitor parameters are also listed accordingly.

Detail experiment records have been established for the crack growth testing of both base and welded material using SNTT approach. In bases material, the crack depth measurement in the cutting cross sections was characterized using optical microscope. Good agreement has been achieved between predictions from the compliance study and the experimental data. Defects were found in some base materials, but not the others. In welded material, the crack penetrated towards the center for the samples under one targeted fatigue loading; while for weld sample under multiple loading cycles with the sequential reduction in load amplitudes the observed crack growth contour seems to deviate from the cylinder center.

Other potential areas to investigate in the future include fracture toughness testing of both base and welded materials for X52 steel. More effort in both numerical modeling and experimental measurement are needed to study the crack penetration pattern of welded material in SNTT cycle fatigue process. The next step plan will be to perform in-situ SNTT test for X52 materials in hydrogen environment to study the effects of hydrogen embrittlement on these pipeline materials.

The SNTT test of X80 provided some preliminary results for fracture toughness measurements. The acoustic method has been successfully implemented into SNTT testing protocol to capture the pop-in of steel in the fracture initiation stage to investigate the fracture behavior of the extreme high toughness materials.

References

[Abaqus 2010] Abaqus software manual (2010), Simulia, Dassault Systèmes.

[Abraham 1995] Abraham, D. P. and Altstetter, C. J. "Hydrogen-Enhanced Localization of Plasticity in an Austenitic Stainless Steel". *Metallurgical and Materials Transactions 26A*, 2859-2871.

[ASTM 2010] ASTM F519: Standard Test Method for Mechanical Hydrogen Embrittlement Evaluation of Plating/Coating Processes and Service Environments. West Conshohocken, PA.

[Baldwin 2009] Baldwin, D., Gardiner, M.R., and Bakke, P. Design and development of high pressure hydrogen storage tank for storage and gaseous truck delivery. FY2009 Annual Progress Report.

[Bromley 2008] Bromley, D.M. "Hydrogen Embrittlement testing of austenitic stainless steels sus 316 and 316L", master thesis, the University of British Columbia, Canada.

[Carlisle 1959] Carlisle, M.E. and Jackman, R.B. Method of Testing for Hydrogen Embrittlement. Northrop Aircraft, Inc, Hawthorne, California.

[Caskey 1983] Caskey, G.R. Hydrogen Compatibility Handbook for Stainless Steels (DP-1643). EI du Pont Nemours, Savannah River Laboratory, Aiken SC.

[Fidelle 1974] Fidelle, J.P., Bernardi, R., Broudeur, R., Roux, C. and Rapin, M. Disk Pressure Testing of Hydrogen Environment Embrittlement. in: Hydrogen Embrittlement Testing, ASTM STP 543, American Society for Testing and Materials, 221-253.

[Gavriljuk 2003] Gavriljuk, V.G., Shivanyuk, V.N. and Foct. J. "Diagnostic Experimental Results on the Hydrogen Embrittlement of Austenitic Steels", Acta Materialia 51:1293-1305.

[Gaydos 2007] Gaydos, S. "SERDP Hydrogen Re-Embrittlement DOE Test Plan Status", DoD Metal Finishing Workshop – Chromate Alternatives for Metal Treatment and Sealing, Layton, UT.

[Han 1998] Han, G., He, J., Fukuyama, S. and Yokogawa, K. "Effect of Strain-Induced Martensite on Hydrogen Environment Embrittlement of Sensitized Austenitic Stainless Steels at Low Temperatures". Acta Materialia 46(13): 4559-4570.

[Hayden 2007] Hayden, L.E., Material Testing Priorities for H2 Infrastructure. ASME/SRNL Materials and Components for Hydrogen Infrastructure Codes and Standards Workshop, Aiken, SC.

[Herm 1999] Herms E., Olive J.M., and Puiggali, M. "Hydrogen Embrittlement of 316L Type

Stainless Steel". *Materials Science and Engineering A* 272: 279-283.

[Hua 2010] Hua, T., Ahluwalia, R., Peng, J.K., Kromer, M., Lasher, S., McKenney, K., Law, K., and Sinha, J. Technical Assessment of Compressed Hydrogen Storage Tank Systems for Automotive Applications.

[Liang 2008] Liang, Y., Ahn, D.C., Sofronis, P., Dodds Jr., R.H. and Bammann. D. "Effect of Hydrogen Trapping on Void Growth and Coalescence in Metals and Alloys". Mechanics of Materials 40:115-132.

[Losch 1979] Losch, W. "Hydrogen Embrittlement: A New Model for the Mechanism of Reduction of Metallic Cohesion". Scripta Metallurgica 13, 661-664.

[Raymond 1972] Raymond, L. Hydrogen Embrittlement Testing: A Symposium Presented at the Seventy-fifth Annual Meeting, American Society for Testing and Materials, Los Angeles, Calif., 543:25-30.

[Sanford 2003] Sanford, R.J., Principles of fracture mechanics, Pearson Education, Inc., Upper Saddle River, NJ, 2003.

[Shivanyuk 2001] Shivanyuk, V.N., Shanina, B.D., Tarasenko, A.V., Gavriljuk, V.G. and Foct. J. "Effect of Hydrogen on Atomic Bonds in Autenitic Stainless Steel". Scripta Materialia 44:2765-2773.

[Shivanyuk 2003] Shivanyuk, V.N., Foct, J., Gavriljuk. V.G. "On a Role of Hydrogen-Induced ε-Martensite in Embrittlement of Stable Austenitic Steel". Scripta Materialia 49:601-606.

[Somerday 2005] Somerday B.P. and Marchi C.S., Technical Reference on Hydrogen Compatibility of Materials. Austenitic Stainless Steels (code 2101). Sandia National Laboratories, Livermore CA.

[Somerday 2010] Somerday B.P. and Marchi C.S., Technical Reference on Hydrogen Compatibility of Materials. Plain carbon ferritic steels: C-Mn Alloys (code 1100). Sandia National Laboratories, Livermore CA.

[Varias 2002] Varias, A.G. and Massih, A.R.. "Hydride-Induced Embrittlement and Fracture in Metals – Effect of Stress and Temperature Distribution". Journal of the Mechanics and Physics of Solids 50:1469-1510.

[Walter 1969] Walter, R.J. and Chandler, W.T. Effects of High-Pressure Hydrogen on Metals at Ambient Temperature: Final Report. Rocketdyne, R-7780-1, the National Aeronauticsand Space Administration, Canoga Park CA.

[Wang 2000] Wang, J. A., K. C. Liu, D. E. McCabe and S. A. David (2000). "Using torsional bar testing to determine fracture toughness." *Fatigue & Fracture of Engineering Materials & Structures* 23(11): 917-927.

[Wang 2002a] Wang, J.-A. and K. C. Liu (2002). ORNL Spiral-Notch Torsion Test (SNTT) System. *2002 R&D 100 Award,* R&D Magazine.

[Wang 2002b] Wang, J. A., Liu, K. C. and McCabe, D. E. “An Innovative Technique for Measuring Fracture Toughness of Metallic and Ceramic Materials,” *Fatigue and Fracture Mechanics: 33rd Volume*, ASTM STP 1417, W. G. Reuter and R. S. Piascik, Eds., pp. 757-770.

[Wang 2011] Wang, J. A., Ren, F., Zhang, W. and Feng, Z.L. (2011). "Development of In Situ Techniques for Torsion and Tension Testing in Hydrogen Environment." ASME 2011 Pressure Vessels and Piping Conference (PVP2011) July 17–21, Baltimore, Maryland, USA.